Passive Mode-Locking and Millimeter-Wave Modulation of Quantum Well Lasers

Thesis by

Steven Sanders

In Partial Fulfillment of the Requirements

for the Degree of

Doctor of Philosophy

California Institute of Technology

Pasadena, California

1992

(Defended October 22, 1991)

To my parents

Acknowledgments

It is a great pleasure to acknowledge the support and encouragement of my advisor, Professor Amnon Yariv. He and his group provided the atmosphere and resources necessary for exciting research and for my growth as an independent scientist.

I would especially like to thank Dr. Joel Paslaski for introducing me to the field of high speed optics and for the many hours he spent teaching me experimental procedures and laser theory.

I have very much enjoyed working with Lars Eng, whose commitment to growing good laser materials in the face of numerous obstacles was essential to the success of our work. Thomas Schrans has greatly contributed to the mode-locking work during the past year and I have benefited from our many discussions on this subject. His critical reading of this thesis is especially appreciated. I would also like to thank Gert Cauwenberghs and Randal Salvatore for their assistance.

Much of the experimental work in this thesis would not have been possible without the technical assistance of Desmond Armstrong, Ali Ghaffari, Larry Begay, and Kevin Cooper. The help of Jana Mercado is truly appreciated.

I am very greatful to the National Science Foundation for providing financial support for my education and research.

The encouragement of my parents, brothers, and Ian Arvin during the many years of my education will always be appreciated.

I would especially like to thank Leslie Holsinger for her love and support throughout my years at Caltech.

Abstract

Quantum well lasers with their optical cavities electrically divided into regions of saturable absorption and gain are passively mode-locked to generate picosecond pulse trains. Current is injected into the gain region, and the absorber is biased below the p-n junction turn-on voltage to control the absorption level and the rate of extraction of photogenerated carriers. Using only DC or low frequency electrical bias on monolithic devices, pulse trains at repetition rates above 100 GHz are generated for the first time.

Theoretical considerations show that quantum well laser properties including the reduction of differential gain with increasing carrier density and the fast recovery time of the absorber allow passive mode-locking to occur at repetition rates far beyond the direct modulation bandwidth of a semiconductor laser, at frequencies above 100 GHz. The saturable absorption in the cavity, however, also induces self-sustained pulsations at a few gigahertz that can interfere with the higher frequency mode-locking process. However, it is shown that increasing the photon lifetime in the cavity can inhibit self-sustained pulsations while extending the range of conditions for high-frequency passive mode-locking.

Multisection stripe lasers are fabricated from quantum well materials by etching through the highly conductive cap layer to electrically isolate regions along the stripes. A two-section monolithic triple quantum well GaAs/AlGaAs stripe laser is passively mode-locked at a 108 GHz repetition rate, with pulsewidths averaging 2.4 ps. More stable mode-locking is observed in a three-section passively mode-locked

InGaAs/AlGaAs double quantum well laser emitting 5.9 ps pulses at a 42 GHz repetition rate.

By coupling a two-section quantum well buried heterostructure laser to an external cavity, the pulse train period becomes comparable to the gain and absorber recovery times and compatible with conventional optical detectors and electronics. It is shown that the laser can operate at six different harmonics of the 1.17 GHz repetition rate, by adjustment of the gain section current only. Both small and large-signal saturation models for passive mode-locking are described and applied to determine the conditions where the laser should operate at the different harmonics and are in reasonable agreement with the experimental results. From power spectrum measurements of a laser mode-locked at 546 MHz, the timing jitter is determined to be 5.5 ps above 50 Hz, and the pulse energy fluctuations less than 0.52 % above 200 Hz. While it is expected that stable pulse trains can be generated at these lower repetition rates, as is demonstrated, the stability of the millimeter-wave mode-locked lasers remains a critical problem for future research.

Contents

List of Figures

List of Tables

Chapter 1

Introduction

1.1 High-speed mode-locked lasers

Laser mode-locking was first demonstrated using a He-Ne laser in 1964 [1] and has emerged as one of the most active areas of laser research and applications. Mode-locked lasers generate trains of ultrashort optical pulses that have given researchers access to the temporal evolution of systems on femtosecond time scales, greatly impacting diverse areas of science, including solid-state physics, biochemical kinetics, high-speed electronics, and molecular dynamics [2]. The basic laser mode-locking phenomenon was theoretically described by DiDomenico and Yariv [3,4], and further work explained and guided development of the many different mode-locked systems that emerged over the next decade [5]-[11]. Mode-locked dye lasers [12] quickly became the most important source of subpicosecond optical pulses and can presently emit pulses shorter than 30 femtoseconds, which have been compressed to six femtoseconds [13]. The time-bandwidth limitation for short pulse generation using visible radiation is on the order of a femtosecond, so further large reductions in pulsewidth will probably have to await progress on short wavelength and X-ray laser systems.

A laser is mode-locked by modulating the net gain or optical path length in the cavity at a rate equal to the frequency spacing of the longitudinal resonant modes. Energy is transferred from higher gain to lower gain modes, resulting in simultaneous, phase-locked multimode oscillation as shown in figure 1.1. The temporal coherence results in a train of short pulses with duration on the order of the reciprocal of the phase-locked lasing bandwidth, and in many cases hundreds or even thousands of modes may simultaneously oscillate in phase, demonstrating one of the greatest coherence phenomena in laser physics. One can also visualize mode-locking in the time domain by considering a circulating pulse that strikes one of the mirrors each time it makes a round-trip in the cavity, emitting a short pulse. Because the internal modulation in a mode-locked laser only needs to maintain the shape and power of the circulating pulse, rather than generate new independent pulses, mode-locking can be induced at repetition rates much higher than the direct modulation bandwidth of the laser.

The modulation required for mode-locking can be generated actively, by a time-varying injection current in the case of a semiconductor laser, or passively, by including saturable absorbers. The presence of appropriate saturable absorption causes a fluctuation at the round-trip frequency of the laser to grow into a pulse train, since the absorber responds to an increase in optical intensity by reducing its absorption level,

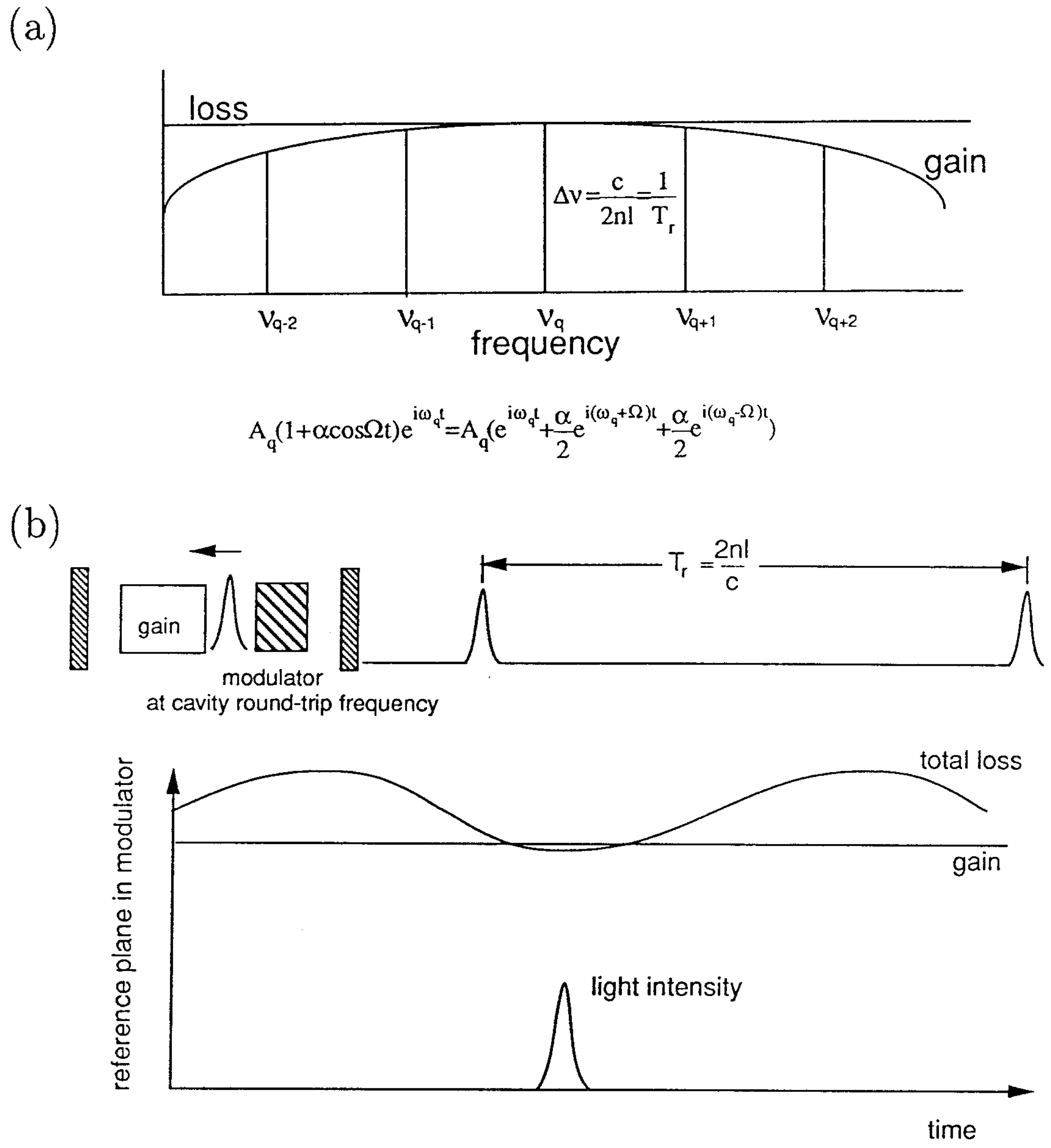

Figure 1.1: Basic mode-locking principles. (a) Frequency domain: the modulation causes net transfer of energy from higher to lower gain modes and locks the modes in phase. (b) Time domain: there is a small window in time where light passing through the modulator can see net gain in a round trip, resulting in the formation of a short pulse.

creating a *net* increase in the gain of the laser cavity. As shown in this thesis, quantum well materials are very well suited to form both regions of gain and appropriate saturable absorption for passive mode-locking in a single monolithic device.

While mode-locked dye lasers have brought us near the fundamental limit on pulsewidth, semiconductor lasers have several potential advantages. A comparison of some basic performance criteria for mode-locked dye lasers and mode-locked semiconductor lasers is shown in table 1.1. In addition to their small size, ease of operation, and very high efficiency, semiconductor lasers have the unique property of generating pulse trains at exteremely high repetition rates. The work in this thesis describes the first demonstration of mode-locked pulse trains at repetition rates above 100 GHz, using quantum well semiconductor lasers. It is, however, often preferable to work at lower repetition rates, and it is demonstrated in Chapter 4 that the same type of passively mode-locked laser that generates pulse trains above 100 GHz can be slowed down to operate below 1 GHz, by coupling the device to an external cavity. The pulse duration and power output from the dye laser are still superior to the best semiconductor lasers, although quantum well lasers have the necessary gain bandwidth to generate pulses on the order of 10 femtoseconds. The shortest pulses directly generated from any type of semiconductor laser, however, are longer that 0.5 picoseconds, most likely due to dispersion, and chirping from both the dependence of refractive index on carrier density and the dependence of the shape of the gain spectrum on carrier density, although no satisfactory quantitative explanation exists. Pulses as short as 0.27 ps have been generated from semiconductor lasers using external amplification and compression [14].

1.2 Mode-locked semiconductor lasers

The first actively mode-locked CW semiconductor laser was demonstrated by Ho et al. in 1978 [15], followed by the first passive device by Ippen et al. in 1980 [16]. The active laser generated 20 ps pulses at 3 GHz, while the passive device emitted 5 ps pulses at 850 MHz. These lasers were coupled to external cavities in order to reduce the repetition rates to be comparable to the carrier recovery times, and variations on these devices, including ion bombarded saturable absorber regions and ring lasers, were developed over the next few years [17]- [19]. There were some observations of subpicosecond pulses, but the outputs always consisted of bursts of multiple pulses, with these bursts typically lasting 20-40 ps.

In 1983, Harder et al. reported passive mode-locking of a two-section bulk GaAs laser with the absorber monolithically integrated with the gain region and having an electrical contact for external bias control [20]. The output pulses, however, were very broad and unstable, most likely due to the linearity of gain as a function of carrier density in bulk GaAs. Lau et al. used a long, degraded laser to passively generate a modulation at 17 GHz without an external cavity, but had no evidence of pulse generation [21]. By using an external multiple quantum well saturable absorber, proton bombarded to reduce the absorption recovery time, Smith et al. succeeded in passively mode-locking a bulk material laser at the quantum well excitonic reso-

Category	semiconductor laser	dye laser system
pump source	electrical	Ar^+ laser, Nd:YAG laser
size	<1 mm- 1 meter	> 1 meter
alignment	little or none	many adjustments
repetition rate	100's MHz - > 100 GHz	~ 100 MHz
efficiency	>20 %	<0.1%
avg. power	1-30 mW	>100 mW
pulsewidth	0.6 ps	<30 fs
compressed pulsewidth	0.27 ps	6 fs
wavelengths	>800 nm	490-880 nm

Table 1.1: Comparison of mode-locked dye laser and mode-locked semiconductor laser performance: semiconductor lasers are smaller, easier to operate, more efficient, and cover a broad range of repetition rates; dye lasers still outperform semiconductor lasers in power and pulse duration, and the two systems cover different spectral ranges (see text for references).

nance [22]. This was the first demonstration that quantum well materials can form a suitable saturable absorber for semiconductor laser passive mode-locking, and pulses with durations under 2 ps were generated. Additional external cavity experiments demonstrated active mode-locking at frequencies up to 20 GHz [23,24], and the first monolithic mode-locked semiconductor laser generated pulses at a 40 GHz repetition rate, even though the direct modulation bandwidth of the device was only about 2 GHz [25].

By this time, it had been recognized that one could generate mode-locked pulse trains at repetition rates far above the direct modulation bandwidth of a semiconductor laser, as had long been known in other laser systems, such as the Nd:YAG laser, which is a common laboratory instrument for generating 100 MHz pulse trains and has recently been mode-locked at 1 GHz [26]. Lau theoretically discussed the possibility of both active and passive mode-locking of semiconductor lasers at repetition rates above 100 GHz, and demonstrated a passively induced 10 % modulation at 67 GHz, again using bulk GaAs materials [27,28]. Presently, all of the reported mode-locking results at repetition rates above 40 GHz have been passive, since injection of the high frequency electrical signals required for active mode-locking is more difficult due to electrical parasitics. In 1989, Vasil'ev et al. demonstrated passive mode-locking at slightly less than 100 GHz to generate 2 ps pulses by pumping multisection bulk lasers with nanosecond electrical injection and very large absorber reverse bias [29].

The work in this thesis describes the first passively mode-locked quantum well semiconductor lasers [30]-[33]. The gain region and absorber are monolithically integrated into a single device, and by electrically isolating the laser into two regions, it can be mode-locked by adjustment of the current flowing into the gain region and voltage bias on the absorber region. Completely monolithic devices, which are fabricated without the need for any regrown regions, generate pulse trains at repetition rates exceeding 100 GHz, while two-section multiple quantum well lasers coupled to external cavities generate stable 5-8 ps pulses. In contrast to all of the bulk material monolithic passively mode-locked semiconductor lasers, which have been pumped with nanosecond electrical pulses, quantum well lasers have been mode-locked using DC injection currents. Since publication of our results concerning mode-locking at above 100 GHz, Chen, Wu, et al. have succeeded in fabricating a colliding-pulse mode-locked monolithic semiconductor laser that emits pulses at a 350 GHz repetition rate [34]. The issues of pulse train stability and a better understanding of the basic physical mechanisms limiting the performance of millimeter-wave mode-locked lasers are now essential to further progress in this field.

1.3 Outline of Thesis

The basic theory of high-repetition rate passive mode-locking is developed in Chapter 2 and applied to demonstrate that passive mode-locking can be induced in quantum well semiconductor lasers at millimeter-wave repetition rates. The important properties of quantum well materials, including reduction of differential gain at high carrier density and fast absorber recovery time under reverse bias are discussed, and geometries for two-section lasers are analyzed. Conditions for self-sustained pulsations, which often accompany and seriously degrade mode-locking performance, are determined, followed by a discussion of parameter ranges for passive mode-locking without simultaneous self-sustained pulsation.

The basic techniques for fabrication and measurement of millimeter-wave mode-locked semiconductor lasers are described in Chapter 3 and Appendix A. Mode-locking is demonstrated at 108 GHz in a triple quantum well two-section monolithic GaAs/AlGaAs laser, where self-sustained pulsation also occurs over a large range of bias conditions. More stable mode-locking is demonstrated in a longer 42 GHz InGaAs/AlGaAs double quantum well laser.

Both experimental demonstrations and related theoretical discussions of external cavity passive mode-locking are presented in Chapter 4. The repetition rates of the pulse trains are reduced to 500 MHz-7 GHz, so that stronger passive mode-locking can be induced, since much larger changes in the gain and absorption can occur between pulses than in the millimeter-wave devices. It is demonstrated that these lasers can operate at at least six different harmonics of the cavity round-trip frequency by adjustment of only the gain current. The conditions for the different harmonics and the expected pulse energies are analyzed theoretically using a large signal time-domain model for the pulse propagation through the gain and absorber media. Chapter 4 concludes with the first quantitative measurements of stability of any passively mode-locked semiconductor laser, demonstrating by power spectral analysis that pulse trains with low timing jitter and small energy fluctuations are generated by a two-section quantum well laser.

References

[1] L.E. Hargrove, R.L. Fork and M.A. Pollack, *Appl. Phys. Lett.*, **5**, 4 (1964).

[2] W. Kaiser (ed.), **Ultrashort Laser Pulses and Applications**, Springer-Verlag (1988).

[3] M. DiDomenico, Jr., *J. Appl. Phys.*, **35**, 2870 (1964).

[4] A. Yariv, *J. Appl. Phys.*, **38**, 388 (1965).

[5] O.P. McDuff and S.E. Harris, *IEEE J. Quantum Electron.*, **QE-3**, 101 (1967).

[6] H. Haken and M. Pauthier, *IEEE J. Quantum Electron.*, **QE-4**, 454 (1968).

[7] D.J. Kuzienga and A.E. Siegman, *IEEE J. Quantum Electron.*, **QE-6**, 694 (1970).

[8] G.H.C. New, *Optics Communications*, **6**, 188 (1972).

[9] G.H.C. New, *IEEE J. Quantum Electron.*, **QE-10**, 115 (1974).

[10] H.A. Haus, *IEEE J. Quantum Electron.*, **QE-11**, 736 (1975).

[11] H.A. Haus, *IEEE J. Quantum Electron.*, **QE-12**, 169 (1976).

[12] E.P. Ippen, C.V. Shank and A. Dienes, *Appl. Phys. Lett.*, **21**, 348 (1972).

[13] R.L. Fork, C.H. Brito Cruz, P.C. Becker and C.V. Shank, *Optics Letters*, **12**, 483 (1987).

[14] P.J. Delfyett, L. Florez, N. Stoffel, T. Gmitter, N. Andreadakis, G. Alphonse and J. Connolly, paper ThB3-1 in *Picosecond Electronics and Optoelectronics, 1991, Technical Digest Series*, (Optical Society of America), 129 (1991).

[15] P.-T. Ho, L.A. Glasser, E.P. Ippen and H.A. Haus, *Appl. Phys. Lett.*, **33**, 241 (1978).

[16] E.P. Ippen, D.J. Eilenberger and R.W. Dixon, *Appl. Phys. Lett.*, **37**, 267 (1980).

[17] J.P. van der Ziel, W.T. Tsang, R.A. Logan, R.M. Mikulyak and W.M. Augustyniak, *Appl. Phys. Lett*, **39**, 525 (1981).

[18] J.P. van der Ziel, R.A. Logan and R.M. Mikulyak, *Appl. Phys. Lett.*, **39**, 867 (1981).

[19] H. Yokoyama, H. Ito and H. Inaba, *Appl. Phys. Lett.*, **40**, 105 (1982).

[20] C. Harder, J.S. Smith, K.Y. Lau and A. Yariv, *Appl. Phys. Lett.*, **42**, 772 (1983).

[21] K.Y. Lau, I. Ury and A. Yariv, *Appl. Phys. Lett.*, **46**, 1117 (1985).

[22] P.W. Smith, Y. Silberberg and D.A.B. Miller, *J. Opt. Soc. Am. B*, **7**, 1228 (1985).

[23] G. Eisenstein, R.S. Tucker, U. Koren and S.K. Korotky, *IEEE J. Quantum Electron.*, **QE-22**, 142 (1986).

[24] J.E. Bowers, P.A. Morton, A.Mar and S.W. Corzine, *IEEE J. Quantum Electron.*, **QE-25**, 1426 (1989).

[25] R.S. Tucker, U. Koren, G. Raybon, C.A. Burrus, B.I. Miller, T.L. Koch and G. Eisenstein, *Electron. Lett.*, **25**, 621 (1989).

[26] T. Sizer, II, *Appl. Phys. Lett.*, **55**, 2694 (1989).

[27] K.Y. Lau, *Appl. Phys. Lett.*, **52**, 2214 (1988).

[28] K.Y. Lau, *IEEE J. Quantum Electron.*, **26**, 250 (1990).

[29] P.P. Vasil'ev and A.B. Sergeev, *Electron. Lett.*, **25**, 1049 (1989).

[30] S. Sanders, L.E. Eng, J. Paslaski and A. Yariv, *Appl. Phys. Lett.*, **56**, 310 (1990).

[31] S. Sanders, L.E. Eng and A. Yariv, *Electron. Lett.*, **26**, 1087 (1990).

[32] S. Sanders, A. Yariv, J. Paslaski, J.E. Ungar and H.A. Zarem, *Appl. Phys. Lett.*, **58**, 681 (1991).

[33] S. Sanders, T. Schrans, A. Yariv, J. Paslaski, J.E.Ungar and H.A. Zarem, *Appl. Phys. Lett.*, **59**, 1275 (1991).

[34] Y.K. Chen, M.C. Wu, T. Tanbun-Ek, R.A. Logan and M.A. Chin, *Appl. Phys. Lett.*, **58**, 1253 (1991).

Chapter 2

High repetition-rate passive mode-locking theory

2.1 Introduction

The basic theory of passive mode-locking in two-section quantum well lasers is developed in this chapter. The two main issues addressed are the conditions under which strong modulation at the laser cavity-mode spacing is passively induced, and the stability of the laser against lower frequency self-sustained pulsations, which lead to unstable mode-locking or pulse trains with a large amplitude modulation envelope. A frequency domain treatment of mode-locking will be pursued, specialized to the case of small-saturation passive mode-locking, where the basic assumption is that the modulation of the gain and absorption due to the light pulses in the cavity can be approximated as sinusoidal. Such a theory will allow us to determine some of the effects of the cavity geometry, pumping conditions and material properties on passive mode-locking repetition rate limitations. Stability of the average energy in the laser cavity will be analyzed by a small-signal analysis of rate equations for a laser containing a region of saturable absorption, and used to show ways to reduce self-pulsation problems in the laser. These two models will then be combined to demonstrate that quantum well lasers can be mode-locked at millimeter-wave repetition rates, without lower frequency self-sustained modulation.

The basic model used to study the two-section quantum well laser is illustrated in figure 2.1. A single optical cavity is electrically divided into regions biased to provide gain and absorption. The gain region is described by a differential gain G, carrier lifetime τ_g, and saturated DC gain level g_0. Similarly, the absorber is described by a differential gain A, which will hereafter be referred to as the differential absorption, carrier lifetime τ_a, and saturated DC absorption level a_0, where a_0 is negative. The gain region has length l_g; the absorber has length l_a, and a uniform DC optical intensity s_0 is assumed. The relationship between the external bias conditions and the internal DC operating point can be established two different ways. The current flowing into the gain region determines the unsaturated gain level of the laser, while the bias on the absorber determines the rate of carrier extraction and, therefore, the effective absorber carrier lifetime, although there can be some spectral shifting due to the quantum confined Stark effect that will not be considered here [1]. By considering a given s_0 and unsaturated absorption, a_0', a saturated absorption level can be determined, and the DC saturated gain level is fixed by the threshold condition.

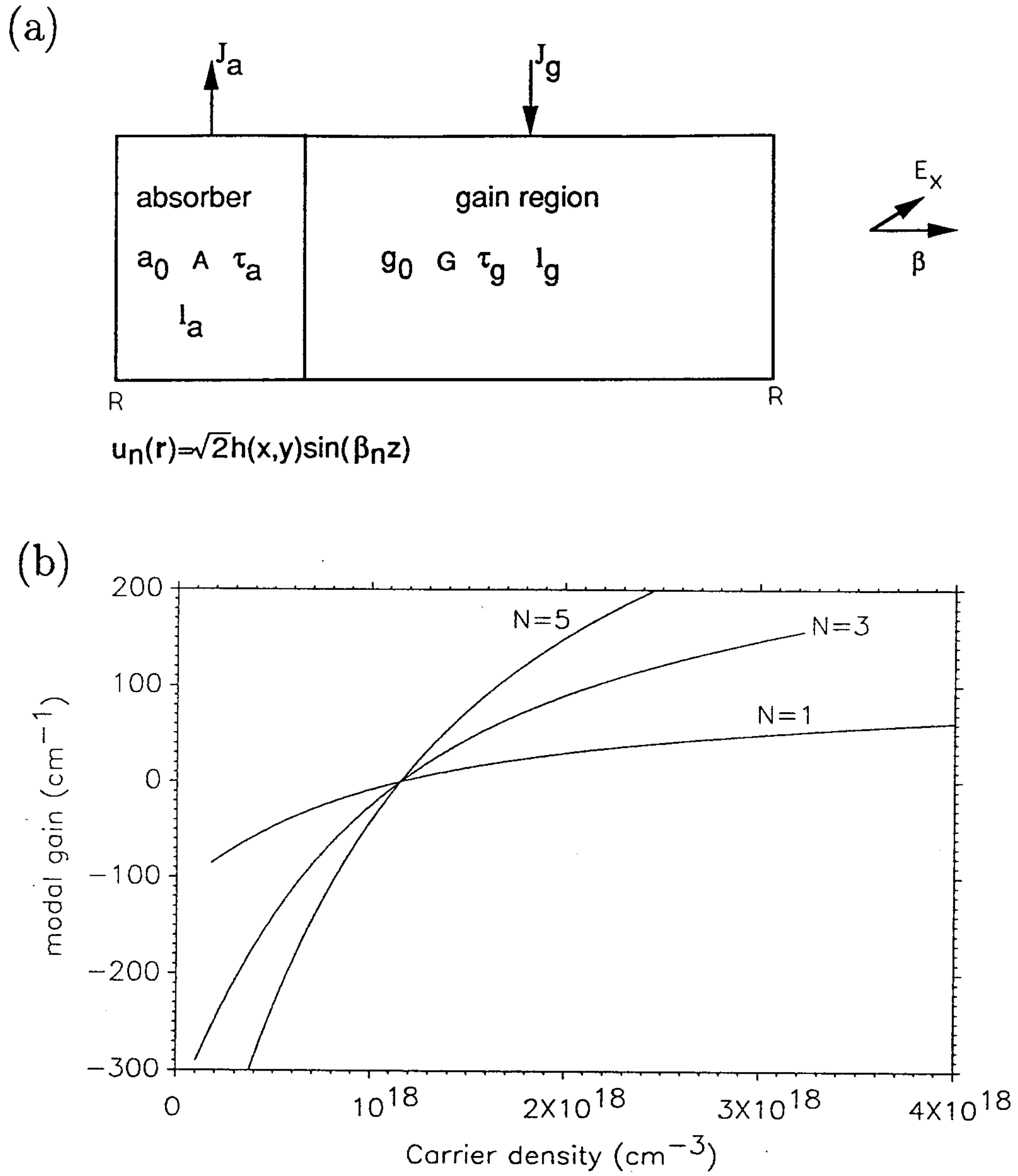

Figure 2.1: Model for the 2-section quantum well laser. (a) Cavity geometry and parameters describing operating conditions; a_0, A, τ_a, and l_a are the saturated absorption level, the differential absorption, the absorber recovery time, and the absorber length, respectively, with g_0, G, τ_g, and l_g corresponding to the same parameters in the gain region. (b) Qualitative calculation of gain for N quantum wells, showing decrease in differential gain at higher carrier densities.

This model requires assuming constant A and τ_a over a large range of carrier densities, but only a small signal expansion of the gain about its operating point. Alternatively, one may consider a given unsaturated gain level to determine s_0, but this requires the assumption of constant G and τ_g, in addition to the earilier assumptions about the absorption. For high repetition rate mode-locking and analysis of the laser stability, the former model will be used, since only small changes occur in the gain due to saturation by the time varying optical intensity. However, for the strong passive mode-locking to be considered in Chapter 4, large signal changes in gain and absorption occur, so the latter model will be used. An additional advantage of the second model is that it allows approximate relationships to be established between the gain current levels and passive mode-locking conditions.

Figure 2.1(b) shows a qualitative calculation of modal gain for one, three, and five quantum wells, using the model in reference [2]. As will be shown in the following section, an important feature of quantum well materials for passive mode-locking is the decrease in the differential gain with carrier density. The two section laser will operate with the gain region at a level around 50-100 cm^{-1}, while the absorber will have a negative gain value. In choosing a material for the mode-locked devices, one must consider having a large ratio of differential absorption to differential gain, yet have enough gain at modest injection currents for the device to operate. These requirements are both met by using multiple quantum well materials, and both double and triple quantum well lasers are used in the experiments described in Chapter 3. Approximate values for the ratio of differential absorption to differential gain are in the range of 1.5 to 3, based upon more accurate calculations and experimental measurements [3]-[5]. The value of the differential absorption is also very important in determining the high frequency mode-locking limitations, and recent measurements and calculations give values around $10^{-15}\mathrm{cm}^2$ [5].

2.2 Small-saturation passive mode-locking

A self-consistent solution for passive mode-locking of a two-section semiconductor laser will be developed, using a treatment similar to reference [6]. However, the present model considers the spatial distribution of the carrier density modulation, which has been shown to be important in the geometric design [7], and the absorber recovery time, which is critical in determining the saturated absorption level and the absorber modulation strength. Earlier models [8] have assumed that the stimulated lifetime in the absorber is much shorter than the recovery time, which is not necessarily true under strong reverse bias conditions, where recovery times are on the order of 100 psec or less [9,10]. A measurement of the recovery time of the absorber when grounded is shown near the end of Chapter 4, where the light pulse circulating in the mode-locked laser cavity is used to probe the laser dynamics by measuring the absorber voltage with a sampling oscilloscope synchronized to the pulse train. While the measurement is probably limited by electrical parasitics, it shows a <150 picosecond absorber recovery time.

2.2.1 Mode-Coupling Equations

Starting from Maxwell's equations and assuming a sinusoidal modulation of the carrier densities in the regions of gain and absorption, mode-coupling equations are derived. The amplitudes and phases of the gain and absorption modulations are assumed to be known from a self-consistency requirement to be invoked later. The basic strategy to find self-consistent passive mode-locking solutions is illustrated in figure 2.2(a). First the response of the multimode electric field to an electric susceptibility varying at the mode-spacing frequency is determined. The optical modulation of the multimode field is calculated in section 2.2.2 and used to determine the carrier density modulation, which determines the susceptibility. Finally, the steady-state solution for a three mode electric field is made self-consistent in section 2.2.3, giving the necessary conditions to achieve a strong modulation at the mode-spacing frequency. The first harmonic of the optical modulation and carrier density modulations along the length of the laser are shown in figures 2.2(b) and 2.2(c), where the additional arrows in figure 2.2(c) represent the gain modulation when the optical modulation is at its maximum. The absorber has a gain modulation component in phase with the optical modulation, while the gain region modulation has a component 180° out of phase and tends to suppress intensity fluctuations. As a minimum condition for passive mode-locking, the total in-phase gain modulation from the absorber must be larger than the total out-of-phase gain modulation from the gain region.

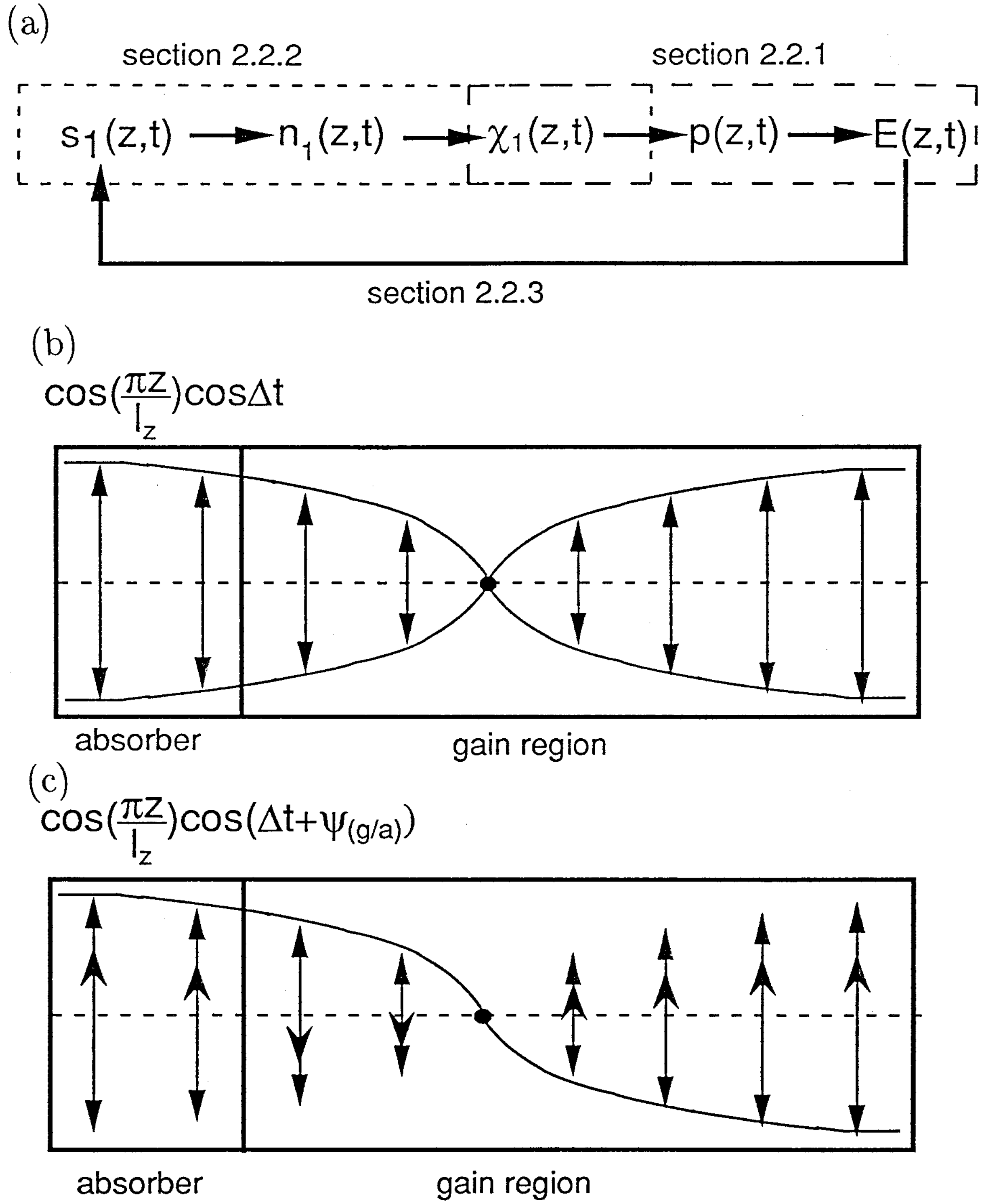

Figure 2.2: (a) Outline of self-consistent passive mode-locking calculation; (b) optical modulation at the first harmonic of the cavity due to beating of adjacent modes; (c) gain modulation in response to the optical modulation; the additional arrows in (c) represent the gain modulation when $\cos(\Delta t) = 1$.

Amplitude-Phase equations of motion (Lamb theory)

The electric and magnetic fields inside the semiconductor laser cavity satisfy Maxwell's equations and constitutive relations, where an effective conductivity accounts for linear cavity losses. The cavity is modeled as having perfect reflectors and a uniformly distributed loss, an approximation that remains valid as long as the intensity along the direction of propagation does not vary much, which requires small mirror losses and low internal losses, including the saturated absorption. Modifications to include real mirror losses and the exponential growth of the field in the cavity are discussed in reference [11]. The amplitude-field equations of motion are now derived as follows [12,13]:

$$\nabla \cdot \mathbf{D}(\mathbf{r},t) = 0 \tag{2.1}$$

$$\nabla \cdot \mathbf{B}(\mathbf{r},t) = 0 \tag{2.2}$$

$$\nabla \times \mathbf{E}(\mathbf{r},t) = -\frac{\partial \mathbf{B}(\mathbf{r},t)}{\partial t} \tag{2.3}$$

$$\nabla \times \mathbf{H}(\mathbf{r},t) = \mathbf{J}(\mathbf{r},t) + \frac{\partial \mathbf{D}(\mathbf{r},t)}{\partial t} \tag{2.4}$$

$$\mathbf{J}(\mathbf{r},t) = \sigma \mathbf{E}(\mathbf{r},t) \tag{2.5}$$

$$\mathbf{D}(\mathbf{r},t) = \epsilon_0 \mathbf{E}(\mathbf{r},t) + \mathbf{P}(\mathbf{r},t) \tag{2.6}$$

$$\mathbf{B}(\mathbf{r},t) = \mu_0 \mathbf{H}(\mathbf{r},t) \tag{2.7}$$

where the magnetic polarization has been neglected. From equations 2.3 and 2.4, the wave equation

$$\frac{\partial^2 \mathbf{E}(\mathbf{r},t)}{\partial t^2} + \frac{\sigma}{\epsilon}\frac{\partial \mathbf{E}(\mathbf{r},t)}{\partial t} - \frac{1}{\mu_0 \epsilon}\nabla^2 \mathbf{E}(\mathbf{r},t) = -\frac{1}{\epsilon}\frac{\partial^2 \mathbf{p}(\mathbf{r},t)}{\partial t^2} \tag{2.8}$$

is derived, where the non-resonant component of the electric susceptibility is included in ϵ, and $\mathbf{p}(\mathbf{r},t)$ is the resonant polarization.

The electric field is expanded as:

$$\mathbf{E}(\mathbf{r},t) = \sum_n \varepsilon_n(t)\mathbf{u}_n(\mathbf{r}) \tag{2.9}$$

where the $\mathbf{u}_n(\mathbf{r})$ are the cold cavity modes, satisfying Laplace's equation:

$$\frac{1}{\mu_0\epsilon}\nabla^2\mathbf{u}_n(\mathbf{r}) + \Omega_n^2\mathbf{u}_n(\mathbf{r}) = 0 \tag{2.10}$$

with solutions

$$\mathbf{u}_n(\mathbf{r}) = \mathbf{a}(\mathbf{x},\mathbf{y})e^{\pm i\beta_n z} \tag{2.11}$$

having

$$\beta_{n+1} - \beta_n = \frac{\mu_g}{c}(\Omega_{n+1} - \Omega_n) \tag{2.12}$$

and normalized by

$$\int \mathbf{u}_n(\mathbf{r}) \cdot \mathbf{u}_m(\mathbf{r})d^3\mathbf{r} = V_c\delta_{nm} \tag{2.13}$$

where V_c is the volume occupied by the mode; μ_g is the group velocity index. The polarization is similarly expanded as:

$$\mathbf{p}(\mathbf{r},t) = \sum_n \wp_n(t)\mathbf{u}_n(\mathbf{r}) \tag{2.14}$$

giving the ordinary differential equation for the time variation of the electric fields:

$$\frac{d^2\varepsilon_n(t)}{dt^2} + \frac{1}{\tau_p}\frac{d\varepsilon_n(t)}{dt} + \Omega_n^2\varepsilon_n(t) = -\frac{1}{\epsilon}\frac{d^2\wp_n(t)}{dt^2} \tag{2.15}$$

where

$$\wp_n(t) = \frac{1}{V_c}\int \mathbf{p}(\mathbf{r},t) \cdot \mathbf{u}_n(\mathbf{r})d^3\mathbf{r} \tag{2.16}$$

and τ_p is the photon lifetime.

Both the electric field and the polarization are expanded to perform a slowly varying envelope approximation, and only one electric field polarization is considered:

$$\varepsilon_n(t) = \frac{1}{2}[E_n(t)e^{i(\omega_n t+\phi_n)} + E_n(t)e^{-i(\omega_n t+\phi_n)}] \tag{2.17}$$

$$\wp_n(t) = \frac{1}{2}[P_n(t)e^{i(\omega_n t+\phi_n)} + P_n^*(t)e^{-i(\omega_n t+\phi_n)}] \tag{2.18}$$

where the E_n's are real and the P_n's are complex due to the phase shift between the polarization and the electric field. In the slowly varying envelope approximation, a first order equation for the electric field amplitude and phase is derived:

$$\dot{E}_n - i[(\Omega_n - \omega_n) - \dot{\phi}_n]E_n + \frac{1}{2\tau_p}E_n = -i\frac{\omega_n}{2\epsilon_n}P_n \tag{2.19}$$

where $\epsilon_n \equiv \epsilon(\omega_n)$.

Form of the polarization

The polarization is related to the electric field by:

$$p(\mathbf{r},t) = \epsilon_0\chi(\mathbf{r},t)E(\mathbf{r},t) \tag{2.20}$$

where $\chi(\mathbf{r},t)$ is modulated adiabatically, or

$$\frac{1}{|\chi(\mathbf{r},t)|}|\frac{d\chi(\mathbf{r},t)}{dt}| \ll \frac{\omega_n}{2\pi} \tag{2.21}$$

and we include only the resonant component of the susceptibility, since the non-resonant refractive index and the linear losses are contained in ϵ and τ_p. In addition, we consider the steady state frequency dependence of the susceptibility, since intraband relaxation times in the semiconductor laser are less than 100 femtoseconds [14]. There are four contributions to $\chi(\mathbf{r},t)$ that influence the mode-locking behavior:

$$\chi(\mathbf{r},t) = \chi_0(\mathbf{r}) + \chi_1(\mathbf{r},t) \tag{2.22}$$

where

$$\chi_0(\mathbf{r}) = \chi_0'(\mathbf{r}) + i\chi_0''(\mathbf{r}) \tag{2.23}$$

and

$$\chi_1(\mathbf{r},t) = \chi_1'(\mathbf{r},t) + i\chi_1''(\mathbf{r},t). \tag{2.24}$$

The real part of equation 2.23 will be considered to first order in the optical frequency and gives rise to a shift in the spacing of the lasing modes, described by modifying the group velocity index. The imaginary part of $\chi_0(\mathbf{r})$ contains the DC gain of the laser, and will be considered to second order in its spectral dependence. The coupling of modes is determined by the modulation of the susceptibility, contained in $\chi_1(\mathbf{r},t)$. The real part gives rise to FM coupling and is present in the semiconductor laser because of the correlation between the real and imaginary parts of the resonant susceptibility, as described by the parameter [15]:

$$\alpha = -\frac{\frac{d\chi'}{dn}}{\frac{d\chi''}{dn}} \tag{2.25}$$

where n is the carrier density. The imaginary part of $\chi_1(\mathbf{r},t)$ gives rise to AM mode coupling, from which the approximate conditions for high repetition rate passive mode-locking will be determined. The FM coupling acts in a manner similar to the AM coupling, but also leads to chirping of the pulses.

Considering only the first harmonic of the carrier density modulation, the susceptiblity has the dependence on the optical frequency, position, and mode spacing frequency Δ:

$$\chi_1(\mathbf{r},t) = \chi_1(\mathbf{r})\cos[\Delta t + \psi(\mathbf{r})]f(\omega) \tag{2.26}$$

where $\psi(\mathbf{r})$ is the phase relative to the phase of the optical modulation, which is chosen to be zero. The value of $\psi(\mathbf{r})$ in the gain region is ψ_g and is ψ_a in the absorber region. The factor $f(\omega)$ describes the dependence of the gain spectrum on the optical frequency. The polarization is:

$$\begin{aligned} p(\mathbf{r},t) &= \epsilon_0\{\chi_0'(\mathbf{r}) + i\chi_0''(\mathbf{r}) + \chi_1'(\mathbf{r})\cos[\Delta t + \psi(\mathbf{r})] + \\ &\quad i\chi_1''(\mathbf{r})\cos[\Delta t + \psi(\mathbf{r})]\}f(\omega)\frac{1}{2}[\sum_n E_n(t)e^{i(\omega_n t+\phi_n)}u_n(\mathbf{r}) + c.c.]. \end{aligned} \tag{2.27}$$

The slowly varying envelope of the polarization is then given by:

$$\begin{aligned} P_m(t) &= \{\frac{\epsilon_0}{V_c}E_m(t)\zeta_0 + \frac{\epsilon_0}{2V_c}E_{m-1}(t)[\zeta_{1g-}e^{i(\phi_{m-1}-\phi_m+\psi_g)} + \zeta_{1a-}e^{i(\phi_{m-1}-\phi_m+\psi_a)}] + \\ &\quad \frac{\epsilon_0}{2V_c}E_{m+1}(t)[\zeta_{1g+}e^{i(\phi_{m+1}-\phi_m-\psi_g)} + \zeta_{1a+}e^{i(\phi_{m+1}-\phi_m-\psi_a)}]\}f(\omega_m) \end{aligned} \tag{2.28}$$

where

$$\zeta_{1(g/a)(\mp)} = \int d^3\mathbf{r}\chi_{1(g/a)}(\mathbf{r})u_{m\mp1}(\mathbf{r})u_m(\mathbf{r}) \tag{2.29}$$

and

$$\zeta_0 = \int d^3\mathbf{r}\chi_0(\mathbf{r})u_m^2(\mathbf{r}). \tag{2.30}$$

(The notation (g/a) indicates quantities pertaining to the gain or absorber region, respectively.) Before proceeding to evaluate these quantities, it is convenient to relate the susceptibilities to the more familiar material gain and absorption properties of the semiconductor laser. The gain is related to the imaginary part of the susceptibility by [16]

$$\chi'' = \frac{\hat{g}\mu_r^2}{k} \tag{2.31}$$

where

$$k = \frac{\mu_r \Omega}{c} \tag{2.32}$$

and μ_r, the material refractive index, and k are determined from the non-resonant contribution to the susceptibility, which has been assumed to be much larger than the resonant contribution. The form of the spatial distribution is approximated by the cold cavity modes giving:

$$u_m(\mathbf{r}) = \sqrt{2}h(x,y)\sin(\beta_m z). \tag{2.33}$$

Evaluating the integral in equation 2.30 yields:

$$\frac{\zeta_0}{V_c} = \frac{\Gamma}{l_z}(\chi_{0g}l_g + \chi_{0a}l_a) \tag{2.34}$$

where Γ is the familiar optical confinement factor; l_g and l_a are the lengths of the gain and absorber regions respectively, and χ_{0g} and χ_{0a} are the DC resonant susceptibilities in the gain and absorber, respectively. The parameter l_z is the length of the laser, and we have used the fact that $m \gg 1$ in evaluating the integral. In terms of the saturated semiconductor material gain, $\hat{g}_0$, and absorption, $\hat{a}_0$,

$$\frac{\zeta_0''}{V_c} = \frac{\Gamma}{l_z}\frac{\mu_r c}{\omega_0}(\hat{g}_0 l_g + \hat{a}_0 l_a). \tag{2.35}$$

Having now derived the response of the electric field to a given polarization and the polarization in terms of the gain and absorption in the cavity, the dynamic response of the carrier density to the optical modulation in the cavity must now be determined so that self-consistent solutions can be found.

2.2.2 Gain and absorption dynamics

The carrier density modulations are determined from a small-signal analysis of the local rate equations, neglecting carrier diffusion, except to average over distances of an optical wavlength. From the electric fields to be determined self-consistently in section 2.2.3 from equation 2.19, the optical modulation is calculated and has the form:

$$s(z,t) = s_0(z) + [\sum_{n=1}^{\infty} \tilde{s}_n(z)e^{in\Delta t} + c.c.]. \tag{2.36}$$

In the steady-state mode-locked condition, the time derivatives of the E_n go to zero, so that

$$s(z,t) = \frac{\epsilon}{2\hbar\omega_0}\frac{c}{\mu_g}|\sum_{n=-q}^{q} E_n e^{i(\omega_n t+\phi_n)}u_n(z)|^2 \tag{2.37}$$

in units of photon intensity, where q is the number of modes excited. The DC optical intensity is then

$$s_0(z) = \frac{\epsilon c}{2\mu_g\hbar\omega_0}\sum_{n=-q}^{q} E_n^2[u_n(z)]^2 \tag{2.38}$$

and the first harmonic of the optical modulation is:

$$\tilde{s}_1(z)e^{i\Delta t} + c.c. \equiv s_1(z,t) = \frac{\epsilon c}{\mu_g\hbar\omega_0}\sum_{n=-q+1}^{q} E_n E_{n-1}\cos(\Delta t + \phi_n - \phi_{n-1})u_n(z)u_{n-1}(z) \tag{2.39}$$

from which the magnitude and phase of the first harmonic of the optical modulation are determined, with the form:

$$s_1(z,t) = s_1(z)\cos(\Delta t + \psi_s) \tag{2.40}$$

where

$$s_1(z) =< 2\sin(\beta_m z)\sin(\beta_{m-1} z) >_\lambda r(\phi_n) \sum_{n=-q+1}^{q} E_n E_{n-1} \tag{2.41}$$

and ψ_s is an arbitrary time reference chosen to be zero. The constant $r(\phi_n)$ is determined from the phases of the fields and is unity for Fourier-transform limited pulses.

In response to the optical modulation created by the beating of the lasing modes, the carrier density in the gain region responds according to the rate equation:

$$\frac{dn_g(z,t)}{dt} = \frac{J_g}{ed} - \hat{g}(z,t)s(z,t) - \frac{n_g(z,t)}{\tau_g} \tag{2.42}$$

where the variations in optical intensity over the lateral dimensions in the active region are neglected. The key approximation to this theory is that only the first harmonic of the carrier density modulation is considered. As the laser approaches the high frequency limit for mode-locking, this approximation improves, since the optical modulation approaches a sinusoidal output, and the higher harmonics of the carrier density modulation become smaller, since the laser operates at frequencies past the 3dB roll-off point. The carrier density is written as

$$\begin{aligned} n_g(z,t) &= n_{0g} + n_{1g}(z,t) \\ &= n_{0g} + n_{1g}(z)\cos(\Delta t + \psi_g) \end{aligned} \tag{2.43}$$

and the gain is expanded about its DC saturated value as

$$\hat{g}(z,t) = \hat{g}_0 + Gn_{1g}(z,t) \tag{2.44}$$

where

$$G = \frac{d\hat{g}}{dn}|_{\hat{g}_0} \tag{2.45}$$

the differential gain. From the small-signal analysis of equation 2.42,

$$g_1(z) = \Gamma G n_{1g}(z) e^{i\psi_g} = \frac{-Gg_0 s_1(z)}{i\Delta + Gs_0 + \frac{1}{\tau_g}} \tag{2.46}$$

where $g_0 = \Gamma\hat{g}_0$. The absorber has a similar low-pass filter response:

$$a_1(z) = \Gamma A n_{1a}(z) e^{i\psi_a} = \frac{-Aa_0 s_1(z)}{i\Delta + As_0 + \frac{1}{\tau_a}} \tag{2.47}$$

where A is the differential gain in the absorption region, and $a_0 = \Gamma\hat{a}_0$.

At this point, it is instructive to more carefully examine the gain and absorber dynamics, neglecting their spatial variation, to determine some of the limiting conditions on achieving a sustained modulation at the cavity resonance. The gain modulation is always more than 90 degrees out of phase with the optical modulation, while the modulation of the absorber gives a gain modulation component in phase with the optical modulation. A minimum condition to achieve passive mode-locking is that the sum of these two gain modulations has a component in phase with the optical modulation, which is Haus' condition for self-starting of passive mode-locking [17]. In addition, the net gain modulation must have a minimum magnitude to transfer enough energy from the center mode to the two nearest neighboring modes so that they will be able to lase. This requires a modulation depth on the order of the fractional difference in gain between these modes. A minimum requirement for passive mode-locking can be derived by expanding the gain and absorber modulation to second order in $\frac{1}{\Delta}$ in the limit of very high frequency. Defining:

$$\gamma_g \equiv Gs_0 + \frac{1}{\tau_g} \tag{2.48}$$

and

$$\gamma_a \equiv As_0 + \frac{1}{\tau_a} \tag{2.49}$$

the second order expansions give:

$$g_1 \rightarrow \frac{iGg_0s_1}{\Delta} - \frac{Gg_0s_1\gamma_g}{\Delta^2} \tag{2.50}$$

and

$$a_1 \rightarrow \frac{iAa_0s_1}{\Delta} - \frac{Aa_0s_1\gamma_a}{\Delta^2}. \tag{2.51}$$

The requirement that $Re(g_1l_g + a_1l_a)$ be greater than zero then becomes:

$$\frac{A}{G} > \frac{\gamma_g g_0 l_g}{\gamma_a |a_0| l_a}. \tag{2.52}$$

Furthermore, since $\frac{1}{\tau_g}$ is usually less than Gs_0, and if we neglect $\frac{1}{\tau_a}$ for the time being, the inequality

$$\frac{A}{G} > \frac{Gg_0l_g}{A|a_0|l_a} \tag{2.53}$$

must be satisfied and implies immediately that A has to be greater than G as a minimum condition for passive mode-locking, since g_0l_g is always greater than $|a_0|l_a$. Considering the absorber recovery time, which can be smaller than $\frac{1}{As_0}$ under appropriate absorber bias, there will be larger modulation of the net gain in phase with the optical modulation, which may permit mode-coupling at higher frequencies and, possibly, allow A to be less than G under some mode-coupling conditions. However, as the pulse becomes shorter and higher harmonics of the carrier modulation are considered, the recovery lifetime plays a smaller role in the saturation dynamics, and A must be greater than G for strong passive mode-locking, as will be shown in the time domain analysis of Chapter 4. The condition derived above is just a minimum condition for the optical modulation to be able to build up from a small fluctuation, and the strength and shape of the carrier density modulation determine how short an optical pulse is generated.

Returning to the problem of finding a self-consistent solution for small-saturation passive mode-locking, the carrier density modulations are used to determine the time-varying polarization that excites and couples modes in equation 2.19. Using equations 2.31 and 2.25:

$$\chi''_{1(g/a)}(z,t) = \frac{\mu_T c}{\omega_0}(\hat{g}/\hat{a})(z,t) \tag{2.54}$$

with the real part of the susceptibility modulation given by

$$\chi'_{1(g/a)}(z,t) = -\alpha \chi''_{1(g/a)}(z,t). \tag{2.55}$$

The spatial pattern of the optical intensity can be averaged over one wavelength to give:

$$< s_0(z) >_\lambda = \frac{\epsilon c}{2\mu_g \hbar \omega_0} \sum_{n=-q}^{q} E_n^2 \equiv s_0 \tag{2.56}$$

and

$$< s_1(z,t) >_\lambda \; = \; \frac{\epsilon c}{\mu_g \hbar \omega_0} \sum_{n=-q+1}^{q} E_n E_{n-1} \cos(\Delta t + \phi_n - \phi_{n-1}) \ast$$

$$\frac{1}{\lambda_m}\int_0^{\lambda_m} 2\sin(\beta_m z)\sin(\beta_{m-1}z)dz \tag{2.57}$$

giving

$$s_1(z,t) = s_1\cos(\Delta t)\cos(\frac{\pi z}{l}) \tag{2.58}$$

and

$$\chi''_{1g}(z,t) = \frac{\mu_r c}{\omega_0}\frac{G\hat{g}_0 s_1}{\sqrt{\Delta^2+\gamma_g^2}}\cos(\frac{\pi z}{l})\cos(\Delta t+\psi_g) \tag{2.59}$$

and

$$\chi''_{1a}(z,t) = \frac{\mu_r c}{\omega_0}\frac{A\hat{a}_0 s_1}{\sqrt{\Delta^2+\gamma_a^2}}\cos(\frac{\pi z}{l})\cos(\Delta t+\psi_a) \tag{2.60}$$

where

$$s_1 = \frac{\epsilon c}{\mu_g \hbar\omega_0} r(\phi_m)\sum_{n=-q+1}^{q} E_n E_{n-1}. \tag{2.61}$$

Finally, evaluating the integral in equation 2.29:

$$\frac{\zeta''_{1g-}}{V_c} = \frac{\zeta''_{1g+}}{V_c} = \frac{\Gamma\mu_r c}{l_z\omega_0}\frac{G\hat{g}_0 s_1}{\sqrt{\Delta^2+\gamma_g^2}}[\frac{l_g}{2}+\frac{l_z}{4\pi}\sin(\frac{2\pi l_g}{l_z})] \tag{2.62}$$

and

$$\frac{\zeta''_{1a-}}{V_c} = \frac{\zeta''_{1a+}}{V_c} = \frac{\Gamma\mu_r c}{l_z\omega_0}\frac{A\hat{a}_0 s_1}{\sqrt{\Delta^2+\gamma_a^2}}[\frac{l_z-l_g}{2}-\frac{l_z}{4\pi}\sin(\frac{2\pi l_g}{l_z})]. \tag{2.63}$$

The real parts of the ζ_1's are given by:

$$\zeta'_{1(a/g)} = -\alpha\zeta''_{1(a/g)}. \tag{2.64}$$

Defining:

$$\tilde{g}_0 = \Gamma\hat{g}_0 l_g\frac{\mu_g}{\mu_r}\frac{2\tau_p}{T_r} \tag{2.65}$$

and

$$\tilde{a}_0 = \Gamma\hat{a}_0 l_a\frac{\mu_g}{\mu_r}\frac{2\tau_p}{T_r} \tag{2.66}$$

as the single pass gain and absorption exponents, normalized to the linear single-pass cavity loss exponent, and defining

$$\kappa_g = \frac{G\tilde{g}_0}{\sqrt{\Delta^2 + \gamma_g^2}}[\frac{1}{2} + \frac{1}{4\pi h_g}\sin(2\pi h_g)] \tag{2.67}$$

and

$$\kappa_a = \frac{A\tilde{a}_0}{\sqrt{\Delta^2 + \gamma_a^2}}[\frac{1}{2} - \frac{1}{4\pi h_a}\sin(2\pi h_g)] \tag{2.68}$$

leads to the simpler expressions:

$$\frac{\zeta_{1g}}{V_c} = \frac{\mu_r^2}{\tau_p \omega_0}\kappa_g s_1(-\alpha + i) \tag{2.69}$$

$$\frac{\zeta_{1a}}{V_c} = \frac{\mu_r^2}{\tau_p \omega_0}\kappa_a s_1(-\alpha + i) \tag{2.70}$$

where

$$h_{(g/a)} = \frac{l_{(g/a)}}{l_z} \tag{2.71}$$

and the cavity round-trip time is given by

$$T_r = \frac{2\mu_g l_z}{c}. \tag{2.72}$$

Using the definitions above in equation 2.35 gives

$$\frac{\zeta_0''}{V_c} = \frac{\mu_r^2}{\tau_p \omega_0}(\tilde{g}_0 + \tilde{a}_0). \tag{2.73}$$

The modulation of the polarization is determined by the material parameters, laser geometry, DC pumping conditions and s_1, which will be determined self-consistently in the next section, under some simplifying approximations. The mode-locked solution is obtained by solving equation 2.19, using equations 2.69, 2.70 and 2.73 in equation 2.28, which gives:

$$2\tau_p \dot{E}_m - i2\tau_p[(\Omega_m - \omega_m) - \dot{\phi}_m]E_m =$$

$$(\tilde{g}_0 + \tilde{a}_0 - 1)E_m - i\tfrac{\omega_m}{2\mu_r^2}\beta_0'(\omega) + (1 + i\alpha)\{\tfrac{E_{m-1}}{2}[\kappa_g e^{i(\phi_{m-1}-\phi_m+\psi_g)} + \kappa_a e^{i(\phi_{m-1}-\phi_m+\psi_a)}] +$$

$$\tfrac{E_{m+1}}{2}[\kappa_g e^{i(\phi_{m+1}-\phi_m-\psi_g)} + \kappa_a e^{i(\phi_{m+1}-\phi_m-\psi_a)}]\}s_1. \qquad (2.74)$$

The geometric effects of the spatial distribution of the gain and absorption modulations modify equations 2.67 and 2.68 by effectively change the ratio A to G to

$$\frac{A}{G}\Big[\frac{\frac{1}{2} - \frac{1}{4\pi h_a}\sin(2\pi h_g)}{\frac{1}{2} + \frac{1}{4\pi h_g}\sin(2\pi h_g)}\Big] \equiv s(\frac{f_a}{f_g}) \qquad (2.75)$$

where f_a and f_g are the geometric factors in brackets in κ_a and κ_g, respectively, and $s = \frac{A}{G}$. This geometric effect is calculated in figure 2.3 and shows that a short absorber, near one-quarter of the cavity length, should be used to maximize the modulation of the absorption relative to the gain, which will increase the net gain modulation at high frequencies. In addition, a short absorber can be more strongly reverse biased, reducing τ_a while still maintaining a long enough gain region to allow the laser to reach threshold.

The spectral dependence of the gain and absorption levels is now considered. The center lasing frequency, in the absence of frequency pulling effects due to the cavity and the carrier density modulation, occurs at the peak of the net gain, $\tilde{g}_0 + \tilde{a}_0$, which can be expanded to second order about the center frequency, ω_0 as:

$$\tilde{g}_0(\omega) + \tilde{a}_0(\omega) = \tilde{g}_0(\omega_0) + \tilde{a}_0(\omega_0) + \frac{1}{2}(\frac{d^2\tilde{g}_0}{d\omega^2} + \frac{d^2\tilde{a}_0}{d\omega^2})|_{\omega_0}(\omega - \omega_0)^2 \qquad (2.76)$$

since the sum of the first derivatives vanishes at the net gain peak. This parabolic

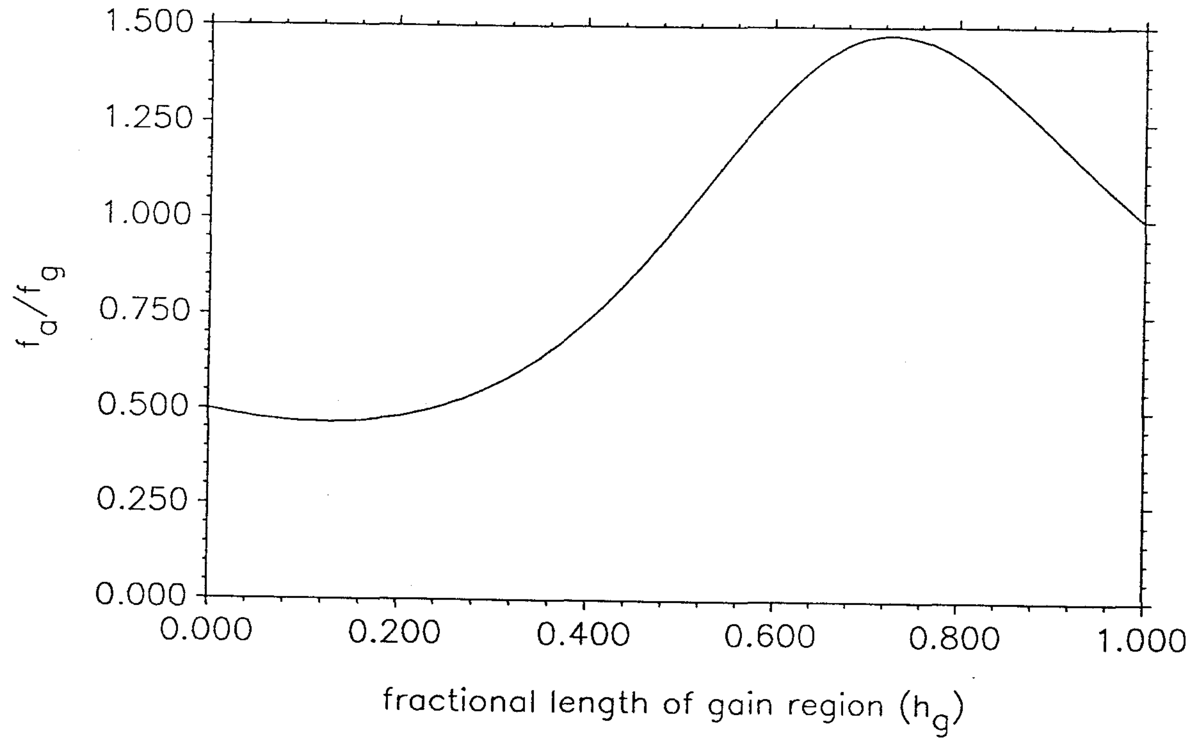

Figure 2.3: Effective enhancement of $\frac{A}{G}$ ratio as a function of fraction of cavity occupied by gain medium; f_a and f_g are the geometric factors in brackets in κ_a and κ_g, respectively.

form for the net gain is used to model the DC net gain in equation 2.74. The gain and absorber modulations, however, will cause a modulation of the shape of the gain spectrum, with different linear and quadratic terms describing their respective modulations, which can cause chirping and frequency pulling. However, these spectral effects of the modulation will not be considered here, and the variation of the modulation strength with wavelength will also be neglected, since its contribution to the mode-coupling is several orders of magnitude less than the κ's. The mode-coupling equation then takes the form:

$$\begin{aligned} &2\tau_p \dot{E}_m - i2\tau_p[(\Omega_m - \omega_m) - \dot{\phi}_m]E_m = \\ &\quad [(\tilde{g}_{00} + \tilde{a}_{00})f_m - 1]E_m + (1+i\alpha)\{\tfrac{E_{m-1}}{2}[\kappa_g e^{i(\phi_{m-1}-\phi_m+\psi_g)} + \kappa_a e^{i(\phi_{m-1}-\phi_m+\psi_a)}] + \\ &\qquad \tfrac{E_{m+1}}{2}[\kappa_g e^{i(\phi_{m+1}-\phi_m-\psi_g)} + \kappa_a e^{i(\phi_{m+1}-\phi_m-\psi_a)}]\}s_1 \end{aligned} \tag{2.77}$$

where

$$f_m = 1 - bm^2 \tag{2.78}$$

and $b \sim 10^{-4} - 10^{-3}$ for a 100 GHz mode spacing.

2.2.3 Self-consistent solutions for small-saturation passive mode-locking

Steady-state solutions to equation 2.77 will be found where the $\dot{E}_m$ are all zero, and the $\dot{\phi}_m$ are all constant and independent of m, corresponding to a uniform shift of the mode spectrum. The solution for three lasing modes, with α equal to zero, will be found as an approximation to the high frequency limit of mode-locking. This solution has been determined in reference [8], and will be derived here more directly. In addition, the current treatment will account for the spatial variation of the modulation, as developed in the previous section. The phases of the locked modes have the form:

$$\phi_m = \Psi_0 + m\Psi_1 + m^2\Psi_2 \tag{2.79}$$

where Ψ_0 is an arbitrary phase and can be set to zero, and Ψ_1 corresponds to a trivial shift of the time origin of the intensity modulation, since we are only concerned with the relative phase between $\psi_{(g/a)}$ and ψ_s. The first non-trivial phase is Ψ_2, which gives rise to a chirping of the pulse, but will be zero for the pure AM mode-coupling case, when $\alpha = 0$.

Neglecting the modulation of the refractive index ($\alpha = 0$), the mode-coupling equation gives:

$$-2i\tau_p\delta(1+b)E_{-1} = [\hat{g}_{00} - (1+b)]E_{-1} + \tilde{\eta}^*\frac{s_1}{s_0}E_0 \tag{2.80}$$

$$0 = (\hat{g}_{00} - 1)E_0 + (\tilde{\eta}E_{-1} + \tilde{\eta}^*E_1)\frac{s_1}{s_0} \tag{2.81}$$

$$2i\tau_p\delta(1+b)E_1 = [\hat{g}_{00} - (1+b)]E_1 + \tilde{\eta}\frac{s_1}{s_0}E_0 \tag{2.82}$$

where

$$\tilde{\eta} = (\kappa_g e^{i\psi_g} + \kappa_a e^{i\psi_a})\frac{s_0}{2} \equiv \eta e^{i\psi_\eta} \tag{2.83}$$

and is determined completely by the material parameters and DC operating point. The definitions:

$$\hat{g}_{00} = \tilde{g}_{00} + \tilde{a}_{00} \tag{2.84}$$

and

$$\delta = \Delta - (\Omega_{n+1} - \Omega_n) \tag{2.85}$$

the detuning of the mode-spacing from the cold cavity mode spacing, have been used.

The zero center frequency detuning and zero chirp can be seen by examining the mode-coupling equations 2.77 for the symmetric solution $E_1 = E_{-1}$ with $\alpha = 0$. Defining

$$x = \hat{g}_{00} - (1 + b) \tag{2.86}$$

we find from the real part of equation 2.81 that the relationship between the side modes and the center mode is

$$E_1 = -\frac{\eta \frac{s_1}{s_0} E_0 \cos \psi_\eta}{x} \tag{2.87}$$

where x determines the DC saturated net gain level and is determined by combining equation 2.87 and equation 2.81 to obtain the equation:

$$x^2 + bx = 2\eta^2 \cos^2 \psi_\eta (\frac{s_1}{s_0})^2. \tag{2.88}$$

The self-consistency can be invoked analytically by using equation 2.61 in equation 2.87 to write:

$$1 = -\frac{4\eta \cos \psi_\eta}{x[1 + 2(\frac{E_1}{E_0})^2]}. \tag{2.89}$$

Evaluating $\frac{1}{1+2(\frac{E_1}{E_0})^2}$ using equations 2.87 and 2.88 gives:

$$x = -2\eta \cos \psi_\eta - \frac{b}{2} \tag{2.90}$$

from the self-consistency equation 2.89. Substituting this expression for x into equation 2.88 then gives the final result:

$$\frac{s_1}{s_0} = \sqrt{2[1 - (\frac{b}{4\eta\cos\psi_\eta})^2]} \tag{2.91}$$

where the $\sqrt{2}$ depth for large η actually corresponds to a depth of 1, when the second harmonic of the optical modulation is added in the evaluation of the optical intensity. This result differs from reference [8] in the definition of η, which is half the value of the equivalent ψ, which also neglects the effects of the spatial variation of the carrier density modulation that have been included in η. Since η is a function of the saturated gain, saturated absorption, optical power, and material and geometric parameters, this expression can be used to determine the limits on the repetition rate for passively inducing a strong modulation in the optical intensity. As b becomes very small, however, and side modes become strong due to spontaneous excitation, a more appropriate parameter to describe the required modulation strength will need to consider the energy transferred to a mode in phase compared with the energy added with random phase due to amplified spontaneous emission.

2.3 Stability of the average power in a semiconductor laser containing saturable absorption

2.3.1 Rate equations and stability analysis

The saturable absorption in the laser cavity that creates the instability resulting in passive mode-locking can also lead to intensity instabilities at lower frequencies, due to the coupling of the average photon and carrier densities. These instabilities usually result in large relaxation oscillations or self-sustained pulsations at a few GHz, and the conditions where they may occur can be determined from the spatially averaged rate equations [18,19], since the time scales are much longer than the cavity round-trip time. These conditions will be rederived here in terms of the parameters most relevant to passive mode-locking, in order to find regimes where stable passive mode-locking may occur. The rate equations for the gain region carrier density, n_g, absorber carrier density, n_a, and photon intensity, s, are:

$$\dot{n}_g = \frac{J_g}{ed} - \hat{g}(n_g)s - \frac{n_g}{\tau_g} \tag{2.92}$$

$$\dot{n}_a = \frac{J_a}{ed} - \hat{a}(n_a)s - \frac{n_a}{\tau_a} \tag{2.93}$$

$$\dot{s} = \Gamma[\hat{g}(n_g)h_g + \hat{a}(n_a)h_a]\frac{c}{\mu_r}s - \frac{s}{\tau_p}. \tag{2.94}$$

In terms of the normalized single pass gain and loss, $\tilde{g}$ and $\tilde{a}$, respectively, (equations 2.65 and 2.66):

$$\dot{s} = (\tilde{g} + \tilde{a} - 1)\frac{s}{\tau_p}. \tag{2.95}$$

Expanding about the DC operating point gives:

$$\hat{g}(n_g) = \hat{g}_0 + Gn_{1g} = \hat{g}_0 + \hat{g}_1 \tag{2.96}$$

$$\hat{a}(n_a) = \hat{a}_0 + An_{1a} = \hat{a}_0 + \hat{a}_1 \tag{2.97}$$

$$s = s_0 + s_1 \tag{2.98}$$

leading to the dynamic equations for a small-signal fluctuation from the steady-state:

$$\begin{pmatrix} \dot{\tilde{g}}_1 \\ \dot{\tilde{a}}_1 \\ \dot{s}_1 \end{pmatrix} = \begin{pmatrix} -\gamma_g & 0 & -G\tilde{g}_0 \\ 0 & -\gamma_a & -A\tilde{a}_0 \\ \frac{s_0}{\tau_p} & \frac{s_0}{\tau_p} & 0 \end{pmatrix} \begin{pmatrix} \tilde{g}_1 \\ \tilde{a}_1 \\ s_1 \end{pmatrix} . \tag{2.99}$$

Stability of the steady-state is then determined by the eigenvalues of this matrix, which are given by the characteristic equation:

$$\lambda^3 + \lambda^2(\gamma_a + \gamma_g) + \lambda[\gamma_a\gamma_g + \frac{s_0}{\tau_p}(A\tilde{a}_0 + G\tilde{g}_0)] + \frac{s_0}{\tau_p}(A\tilde{a}_0\gamma_g + G\tilde{g}_0\gamma_a) = 0. \tag{2.100}$$

The real parts of all three eigenvalues must be negative to ensure stability, although other instabilities, electrooptic in origin, and which will not be considered here, can arise if the absorber bias voltage is chosen to be in a region of negative differential resistance [20].

Invoking the Hurwitz criterion on equation 2.100 requires:

$$\begin{vmatrix} \gamma_a + \gamma_g & \frac{s_0}{\tau_p}(A\tilde{a}_0\gamma_g + G\tilde{g}_0\gamma_a) \\ 1 & \gamma_a\gamma_g + \frac{s_0}{\tau_p}(A\tilde{a}_0 + G\tilde{g}_0) \end{vmatrix} > 0 \tag{2.101}$$

and

$$\begin{vmatrix} \gamma_a + \gamma_g & \frac{s_0}{\tau_p}(A\tilde{a}_0\gamma_g + G\tilde{g}_0\gamma_a) & 0 \\ 1 & \gamma_a\gamma_g + \frac{s_0}{\tau_p}(A\tilde{a}_0 + G\tilde{g}_0) & 0 \\ 0 & \gamma_a + \gamma_g & \frac{s_0}{\tau_p}(A\tilde{a}_0\gamma_g + G\tilde{g}_0\gamma_a) \end{vmatrix} > 0 \tag{2.102}$$

to have the real parts of all three eigenvalues negative. In terms of the material and geometric parameters of the laser, stability requires:

$$\frac{A}{G} < \frac{\tilde{g}_0\gamma_a}{|\tilde{a}_0|\gamma_g} \tag{2.103}$$

and

$$\tau_p > -\frac{s_0(A\tilde{a}_0\gamma_a + G\tilde{g}_0\gamma_g)}{\gamma_a\gamma_g(\gamma_a + \gamma_g)}. \tag{2.104}$$

It can be seen immediately from this expression that increasing the photon lifetime can alleviate the self-sustained pulsation problem.

2.3.2 Relationship between external conditions and internal DC operating point

The saturated DC operating point can be related to the external conditions by considering a given photon intensity, s_0, and an unsaturated DC absorption, $\hat{a}'_0$. From the rate equation 2.93, the saturated DC absorption can be related to the unsaturated level, which is determined by the quantum well material properties. Assuming that the absorption is linearly related to the absorber carrier density by:

$$\hat{a} = A(n_a - n_{0a}) \tag{2.105}$$

equation 2.93 in steady-state gives:

$$0 = \frac{\hat{a}_0' - \hat{a}_0}{\tau_a} - A\hat{a}_0 s_0 \tag{2.106}$$

resulting in

$$\hat{a}_0 = \frac{\hat{a}_0'}{1 + A\tau_a s_0}. \tag{2.107}$$

The DC saturated gain level can be determined from the threshold condition, which requires:

$$\tilde{g}_0 = 1 - \tilde{a}_0. \tag{2.108}$$

However, when the laser is mode-locked, $\tilde{g}_0$ will vary from this level by a small amount, on the order of η, determined from the mode-coupling equations, since energy is added to the lasing modes by the modulation. This small correction will be neglected in section 2.3.3.

2.3.3 Conditions for passive mode-locking without self-sustained pulsation

Passive mode-locking requires a positive modulation depth in equation 2.91:

$$4\eta \cos \phi_\eta > b \tag{2.109}$$

or

$$-2s_0[\frac{G\tilde{g}_0\gamma_g}{\Delta^2 + \gamma_g^2} f_g + \frac{A\tilde{a}_0\gamma_a}{\Delta^2 + \gamma_a^2} f_a] > b. \tag{2.110}$$

The mode-locking ranges are shown in figures 2.4 and 2.5 for laser cavities with 50 GHz and 100 GHz pulse repetition frequencies, respectively, along with the conditions for self-sustained pulsation. An unsaturated absorption level, $\tilde{a}'_0$, of -1.5 is used, comparable to the experimental conditions of Chapter 3. The region to the left of the dashed line is unstable against relaxation oscillations, and the region to the right of the solid line represents conditions where passive mode-locking does not occur. (The region to the left of the dashed line that is very close to the y-axis is stable against self-pulsation.) For a fixed power level, as the absorber recovery time is reduced by decreasing the absorber voltage bias, the laser output will go from CW to mode-locked, and then to self-sustained pulsation. Increasing the ratio of differential absorption to differential gain allows mode-locking to occur with longer absorber lifetimes and at higher repetition rates with less power in the cavity, but it also increases the parameter ranges where the laser is unstable, as shown in figure 2.5, since higher intensities become necessary to prevent self-sustained pulsation. For a fixed absorber recovery time, the laser does not mode-lock at low power because the net gain modulation, proportional to s_0, is too small. If the power becomes too large, however, mode-locking is inhibited because the absorber becomes too strongly saturated, again reducing the net gain modulation below the threshold of equation 2.109.

Two ways to achieve mode-locking over a large range of bias conditions without self-pulsing are to extend the cavity length and, therefore, operate at lower repetition rates, or to increase the photon lifetime and intensity in the laser cavity by applying high reflectivity coatings to the laser facets. Figure 2.6 shows the expected effects of changing the mirror reflectivities to 70%. The mode-locking regime becomes larger, since the unsaturated gain and absorption levels can now be made much larger relative

(a) s=1.5

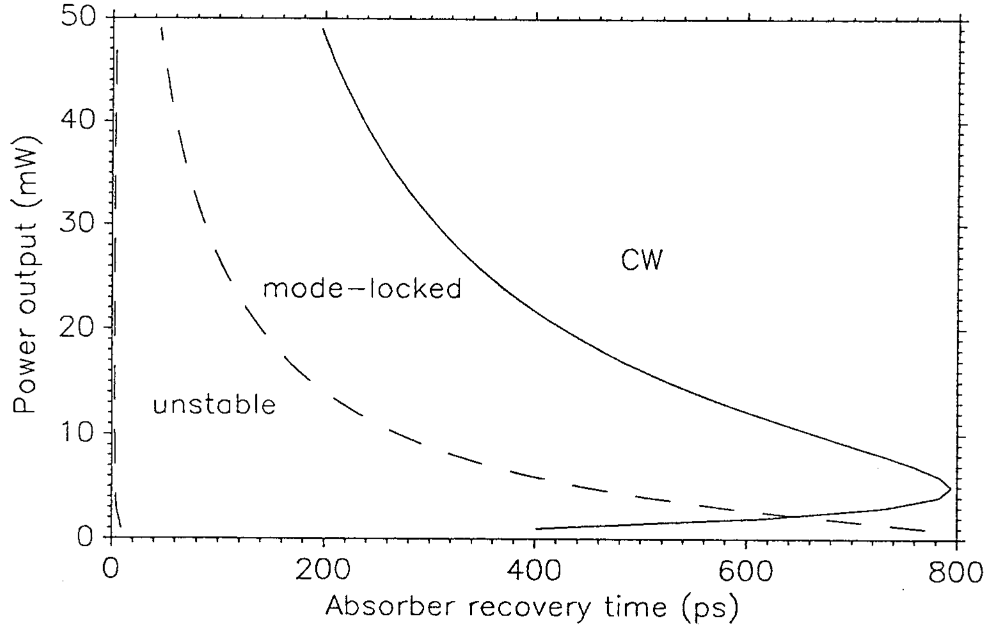

(b) s=3.0

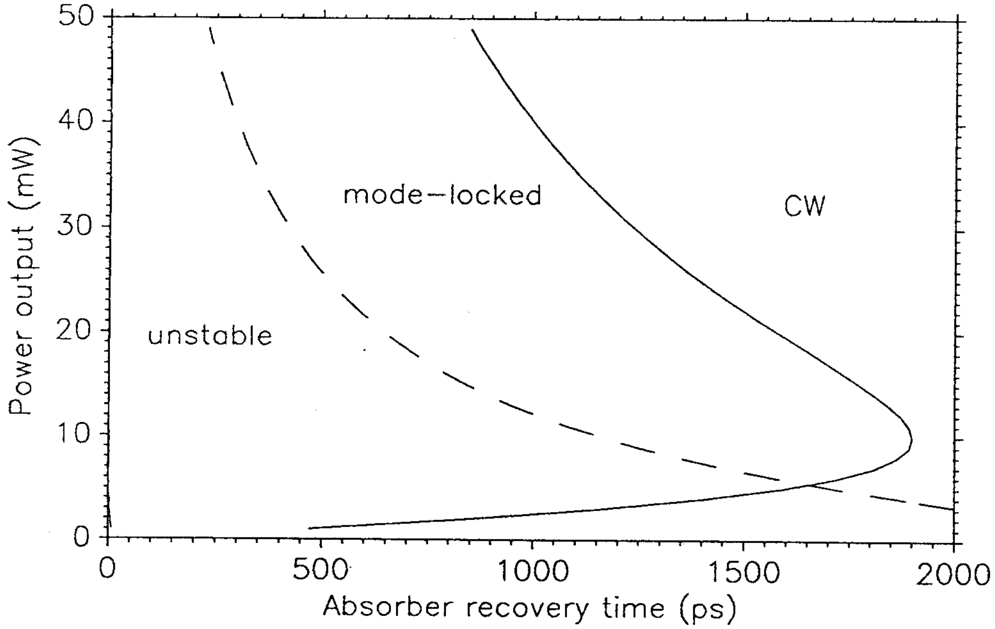

Figure 2.4: Ranges for 50 GHz passive mode-locking and self-sustained pulsation with (a) s $\equiv \frac{A}{G}$ = 1.5 and (b) s=3.0 ($\tilde{a}_0 = -1.5$; $h_g = 0.75$; $\tau_g = 1.0$ns; $A = 10^{-15} cm^2$; $b = 2.5X10^{-5}$; $\alpha_{int} = 10\text{cm}^{-1}$). The laser is unstable to the left of the dashed line and mode-locked to the left of the solid line.

(a) s=1.5

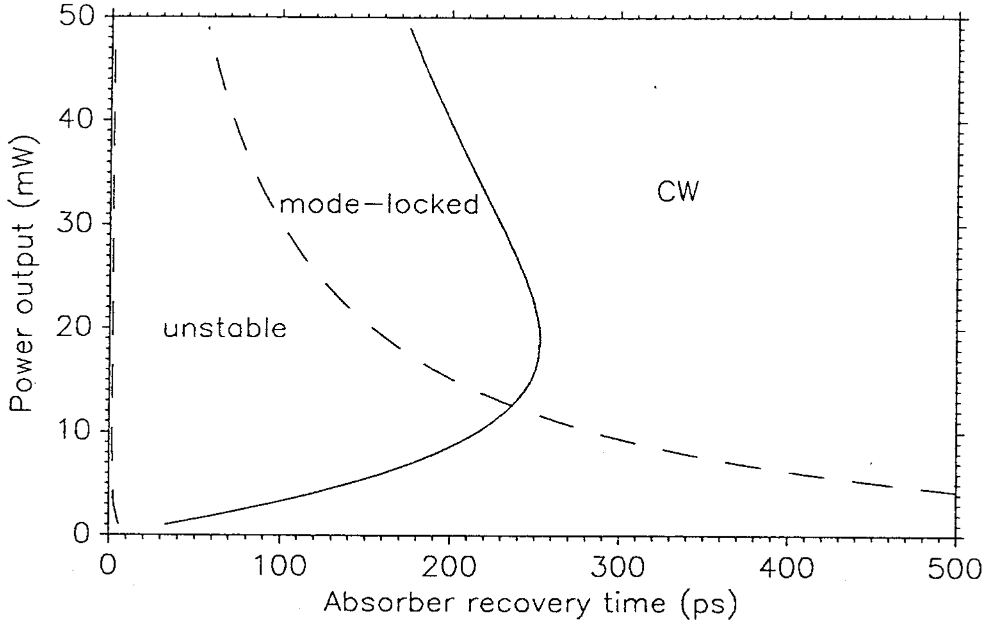

(b) s=3.0

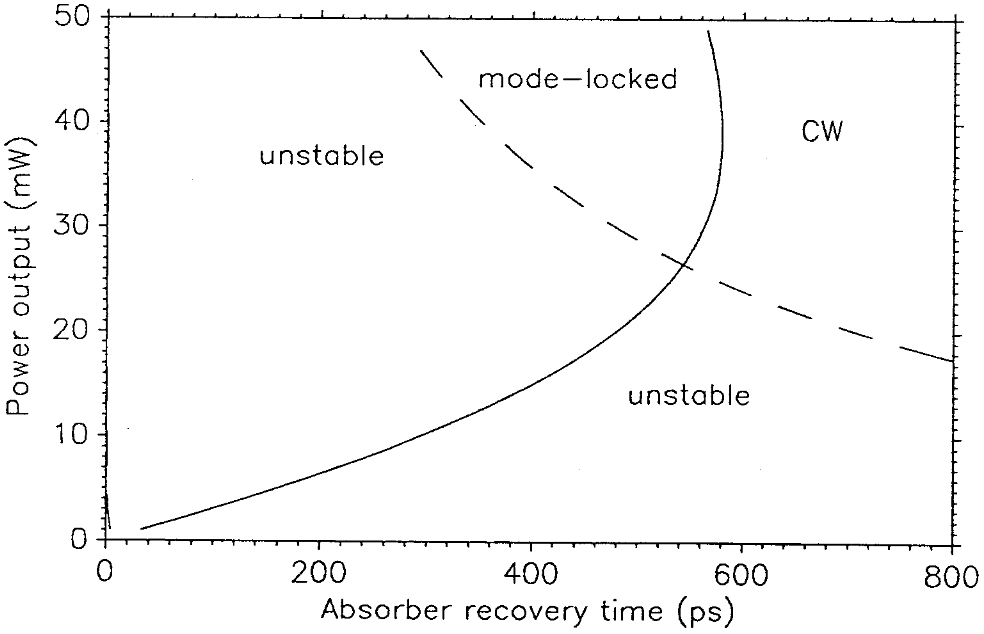

Figure 2.5: Ranges for 100 GHz mode-locking and self-pulsation with (a) s=1.5 and (b) s=3.0 ($\tilde{a}_0 = -1.5$; $h_g = 0.75$; $\tau_g = 1.0$ns; $A = 10^{-15} cm^2$; $b = 10^{-4}$; $\alpha_{int} = 10$cm^{-1}).

to the linear losses, and the self-pulsations are suppressed at much lower output power levels. Recent experimental results [21] clearly show the stabilizing effect of high reflectivity coatings, which should also facilitate mode-locking at higher repetition rates.

The results in this chapter demonstrate that it is in theory possible to achieve a strong passively induced modulation at millimeter-wave repetition rates using quantum well lasers. However, the more stringent requirements on gain and absorber recovery between pulses for conventional passive mode locking with a slow saturable absorber, to be discussed in Chapter 4, are usually not satisfied at these high repetition rates. The resulting pulse trains, therefore, may suffer from problems of stability and may not reach the minimum possible pulsewidth allowed by the gain bandwidth and dispersion of these lasers.

(a) s=1.5

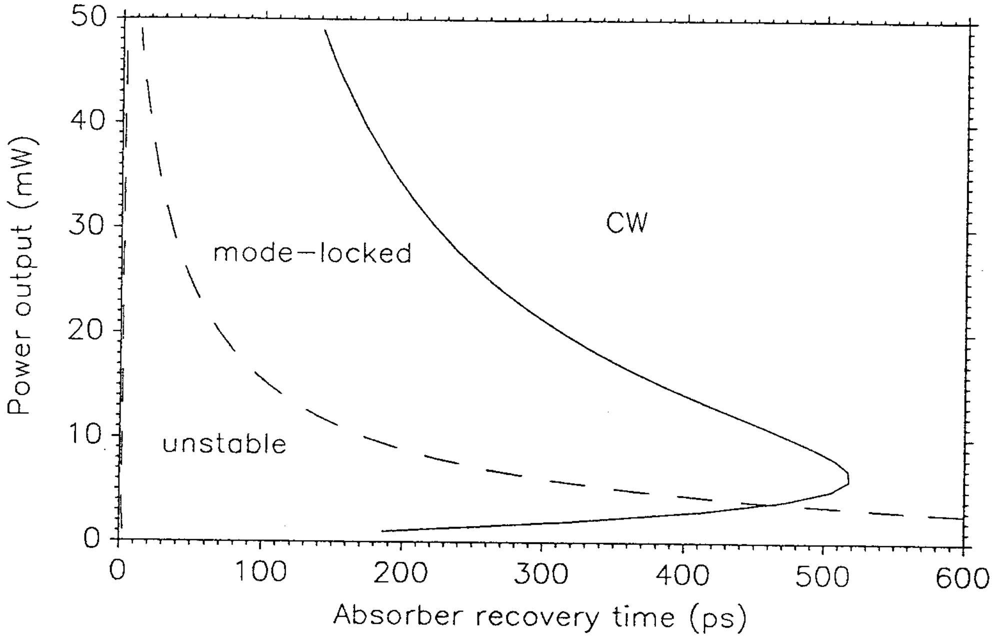

(b) s=3.0

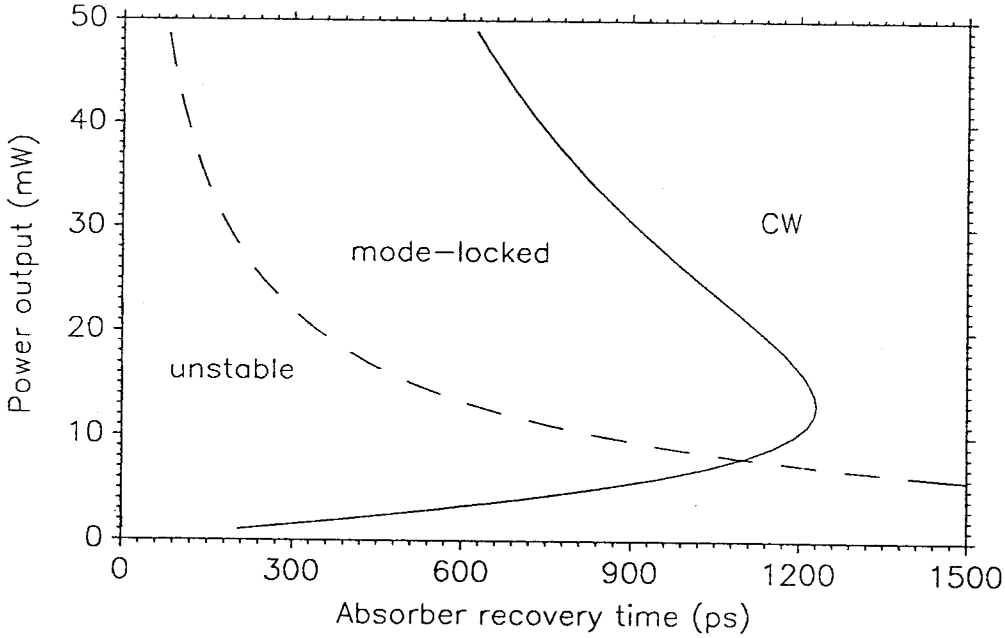

Figure 2.6: Ranges for 100 GHz mode-locking and self-pulsation for laser with 70% facet reflectivities for (a) s=1.5 and (b) s=3.0; ($\tilde{a}_0 = -3.19$; $h_g = 0.75$; $\tau_g = 1.0$ns; $A = 10^{-15} cm^2$; $b = 10^{-4}$; $\alpha_{int} = 10\text{cm}^{-1}$).

References

[1] D.A.B. Miller, D.S. Chemla, T.C. Damen, A.C. Gossard, W. Wiegmann, T.H. Wood and C.A. Burrus, *Phys. Rev. Lett.*, **53**, 2173 (1984).

[2] K.Y. Lau, S. Xin, W.I. Wang, N. Bar-Chaim and M. Mittelstein, *Appl. Phys. Lett.*, **55**, 1173 (1989).

[3] Y. Arakawa and A. Yariv, *IEEE J. Quantum Electr.*, **QE-21**, 1666 (1985).

[4] W. Rideout, B. Yu, J. LaCourse, P.K. York, K.J. Beernink and J.J. Coleman, *Appl. Phys. Lett.*, **56**, 706 (1990).

[5] T. Takahashi, M. Nishioka and Y. Arakawa, *Appl. Phys. Lett.*, **58**, 4 (1990).

[6] K.Y. Lau, *Appl. Phys. Lett.*, **52**, 2214 (1988).

[7] Joel Paslaski, private communication.

[8] K.Y. Lau, *IEEE J. Quantum Electr.*, **QE-26**, 250 (1990).

[9] A. Larsson, A. Yariv, R. Tell, J. Maserjian and S.T. Eng, *Appl. Phys. Lett.*, **47**, 866 (1985).

[10] G. Livescu, A.M. Fox, D.A.B. Miller, T. Sizer, W.H. Knox, A.C. Gossard and J.H. English, *Phys. Rev. Lett.*, **63**, 438 (1989).

[11] A.E. Siegman, *Appl. Phys. Lett.*, **36**, 412 (1980).

[12] Anthony E. Siegman, **Lasers**, University Science Books, ch. 24 (1986).

[13] Murray Sargent III, Marlon O. Scully, and Willis E. Lamb, Jr., **Laser Physics**, Addison-Wesley Publishing Co., ch. 8 (1974).

[14] W. Lin, R.W. Schoenlein, J.G. Fujimoto and E.P. Ippen, *IEEE J. Quantum Electr.*, **24**, 267 (1988).

[15] C.H. Henry, *IEEE J. Quantum Electr.*, **QE-18**, 259 (1982).

[16] Amnon Yariv, **Quantum Electronics**, 3rd ed., ch. 8 (1989).

[17] H.A. Haus, *IEEE J. Quantum Electr.*, **QE-12**, 169 (1976).

[18] N.G. Basov, *IEEE J. Quantum Electr.*, **QE-4**, 855 (1968).

[19] C.H. Henry, *J. Appl. Phys.*, **51**, 3051 (1980).

[20] C. Harder, K.Y. Lau and A. Yariv, *IEEE J. Quantum Electr.*, **QE-18**, 1351 (1982).

[21] J. Paslaski and K.Y. Lau, *Appl. Phys. Lett.*,**59**, 7 (1991).

Chapter 3

Millimeter-wave passive mode-locking experiments

3.1 Introduction

Having shown theoretically in the last chapter that quantum well lasers can be passively mode-locked at repetition rates exceeding 100 GHz, experimental observations of quantum well lasers generating picosecond optical pulse trains at millimeter-wave repetition rates are now presented. The basic device design and fabrication procedures are described, followed by a discussion of ultrafast pulse train measurement techniques. Single shot streak camera measurements are used for all the observations in this chapter, while both streak camera and autocorrelation techniques are used in Chapter 4. Measurements of the pulse train from a two-section GaAs/AlGaAs laser mode-locked at 108 GHz generating 2.4 ps pulses are shown, and more stable pulse trains are generated from longer three-section InGaAs/AlGaAs double quantum well lasers mode-locked at a 42 GHz repetition rate, where large bias ranges for passive mode-locking without strong simultaneous relaxation oscillations of the average power in the laser cavity are observed.

3.2 Device design and structure

The devices described in this chapter were all fabricated from molecular beam epitaxy (MBE) grown quantum well materials. Approximate layer thicknesses, doping levels, and mole fractions are shown in figure 3.1. The stripe laser structure, shown in figure 3.2, is formed by etching mesas to a depth of 1.0 to 1.5 μm, using a mask of 5 μm lines. An insulating layer of SiO_2 is grown by chemical vapor deposition (CVD). Contact openings are etched in the SiO_2 along the length of the mesas, and a contact pattern, with gaps in the metallization, is defined by liftoff. The laser sections are isolated by a 5-7 μm wide, 0.3-0.5 μm deep etch through the highly conductive cap layer, giving resistances of 1-5 kΩ between the regions. After annealing, laser bars are cleaved with a scalpel and tested with microsecond injection current pulses. More detailed fabrication techniques are given in appendix A, and more specific structural information is given with the description of the individual experiments.

Multiple quantum well materials with threshold current densities under 500 $\frac{\mathrm{A}}{\mathrm{cm}^2}$ are used, giving typical threshold values of 15-30 mA for a 300 μm long stripe laser with both sections pumped; there is little change if only the longer region is pumped

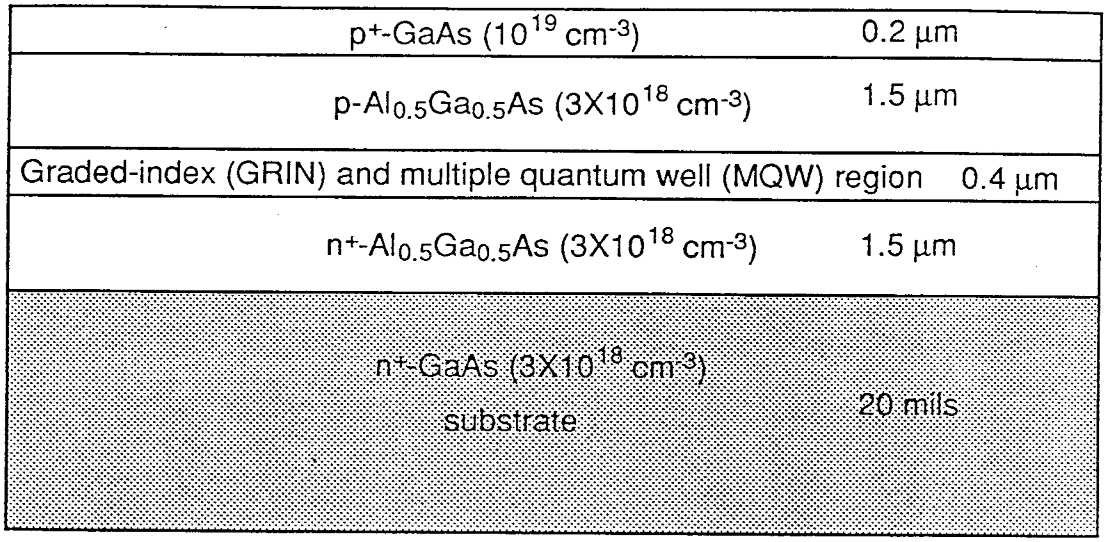

Figure 3.1: MBE grown material used for monolithic passively mode-locked laser fabrication; thicknesses and doping levels are estimated from earlier MBE calibrations.

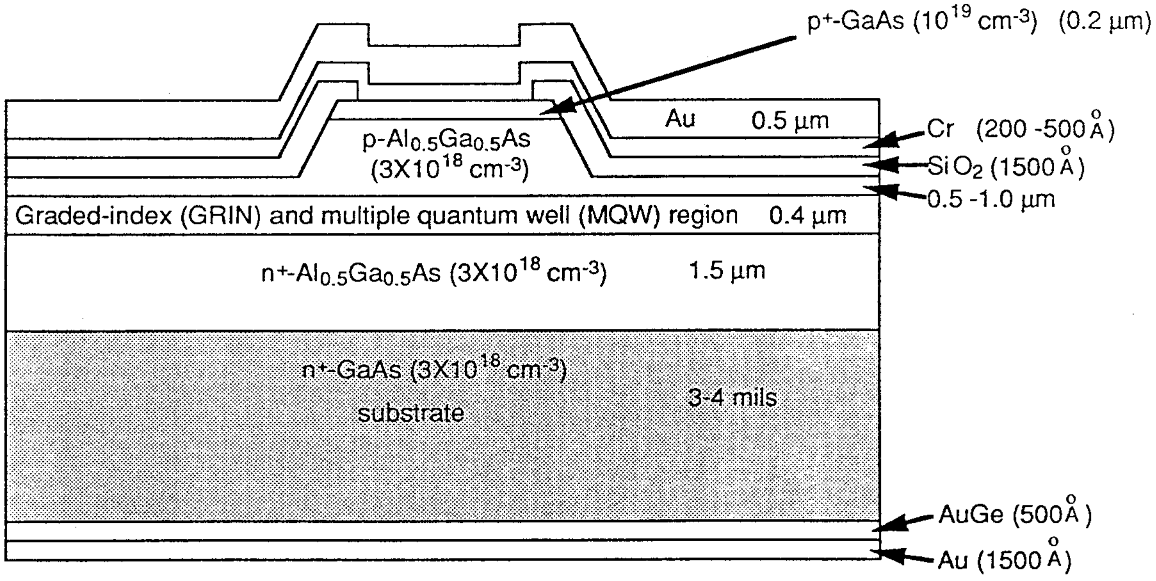

Figure 3.2: Structure of stripe lasers after processing.

while the shorter region is left floating. However, single quantum well lasers show much higher thresholds when only one section is pumped, due to the rapid saturation of gain with increasing carrier density, and were not successfully mode-locked, although some unstable millimeter-wave modulation was observed when one facet was coated to have $> 70\%$ reflectivity.

3.3 Measurement of ultrafast pulse trains

The ultrafast pulse trains generated by mode-locked lasers have intensity changes that are too fast to be measured by conventional optical detectors. The two basic instruments used to measure pulse durations, and repetition rates in the case of millimeter-wave mode-locking, are streak cameras and autocorrelation systems.

3.3.1 Streak Camera System

The streak camera operates by transforming the temporal variation of a light signal into a spatially dispersed electrical signal. Light incident on the photocathode of the streak tube, as shown in figure 3.3, generates photoelectrons that are accelerated toward a phosphor at the rear of the tube. While traversing the length of the tube, these electrons are deflected by a time varying electric field, so that their vertical position is proportional to the time they left the photocathode. The electron current is then amplified by a microchannel plate, which preserves its spatial distribution, and the electrons strike a phosphor, which emits light that is imaged onto a cooled CCD camera, interfaced to a video computer for control and readout. The Hamamatsu C1587 temporal disperser with an S-1 photocathode is used for all the measurements described later.

The streak camera can operate in either a single shot or a synchroscan mode. In the single shot mode, the camera streaks once to obtain an image of the light and has a 2 ps temporal resolution, while in the synchroscan mode, the camera streaks repetitively, at approximately 100 MHz, thus averaging the optical signal. While synchroscan operation gives much better signal-to-noise performance, it requires that the optical output be phase-locked to the 100 MHz scan. It also averages out pulse-to-pulse fluctuations, and temporal resolution is degraded to 5-10 picoseconds by the camera's internal timing jitter. For the passive mode-locking experiments, single shot measurements were required to maintain the higher time resolution, to overcome the lack of suitable synchronization signals, and to observe variations in the laser output intensity on nanosecond time scales. The primary disadvantage of single shot measurements is the high level of shot noise due to the low quantum efficiency ($<$ 0.05%) of the photocathode and low powers ($<$ 100 mW peak) of the semiconductor lasers. On the fastest streak scale, fewer than 100 photoelectrons per channel are generated for a 100 mW instantaneous power input.

Some systematic errors in the streak camera system include accuracy and linearity of the streak speed, linearity of the intensity response of the system, uniformity over the two spatial dimensions, and dark signals. Only the last of these errors will actually require correction in the measurements presented in this thesis. Streak

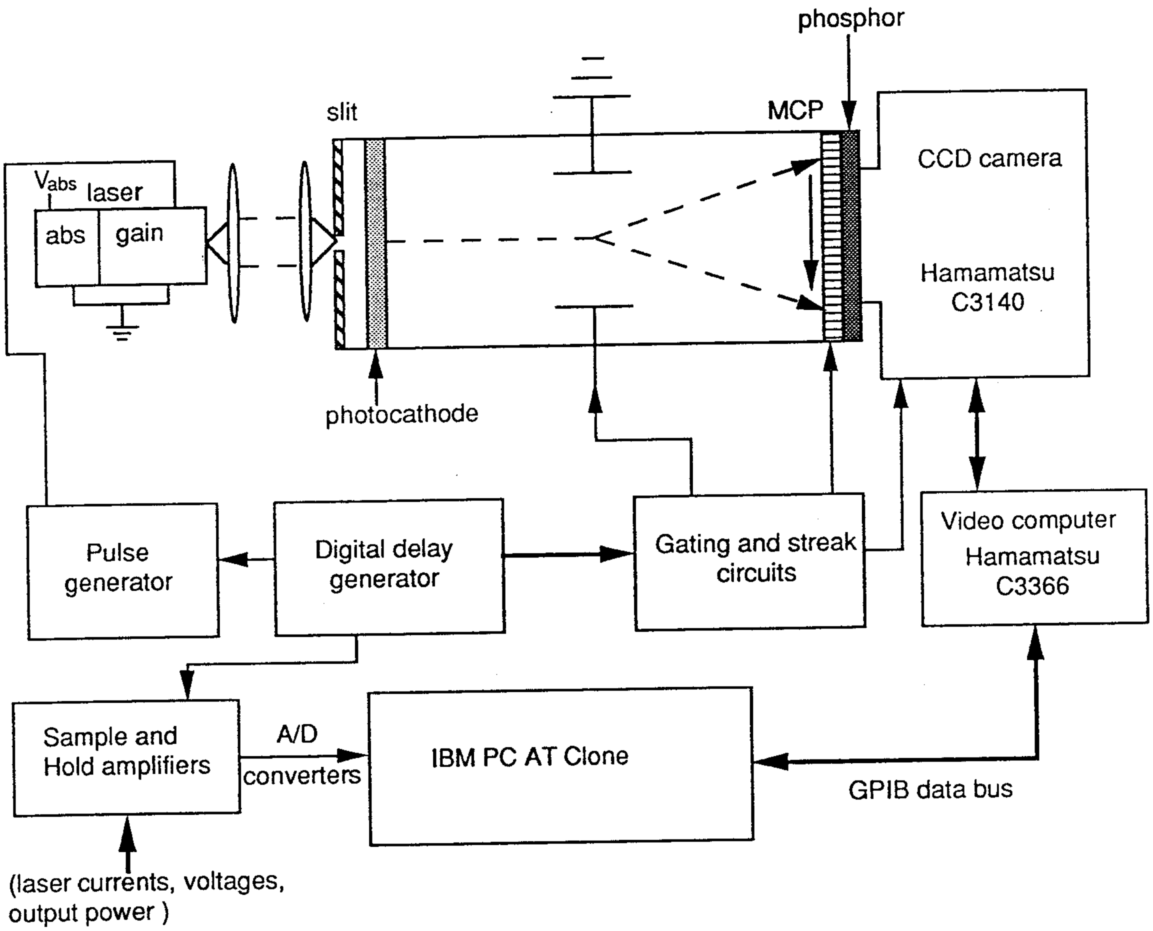

Figure 3.3: Streak camera system and associated synchronization and measurement electronics.

speed calibration was performed by the manufacturer and confirmed to 4% accuracy on the highest streak scale by a picosecond dye laser. Intensity response of the system becomes substantially sublinear at intensities higher than those used in pulsewidth measurements performed in this thesis, resulting in overestimation of the pulse width. The system response nonuniformity over the direction of the streak can be corrected by normalizing the data to the response to a continuous signal, but this error is limited to a few per cent, at the edges of the streak, when the camera is operated at its two highest streak speeds. The signal along the length of the photocathode can also be corrected the same way, but this is unnecessary for the present measurements, since the laser beam is focused to a small spot. The only correction performed in the data is subtraction of the background noise collected in the CCD camera in response to no optical input signal. Dark noise from the photocathode is approximately 10^{-2} photoelectrons per sweep on the slowest streak scale [1] and is, therefore, insignificant for single shot measurements.

3.3.2 Intensity autocorrelation

The duration of ultrashort pulses can also be determined indirectly by autocorrelation of the intensity using second harmonic generation. While this technique enhances temporal resolution to the femtosecond regime, it requires assumption of a pulse shape and gives no information about pulse train stability, since it averages over many pulses. In addition, for high repetition rate mode locking, very unstable, weak, noisy pulses can appear like very short pulses due to correlation of intensity noise.

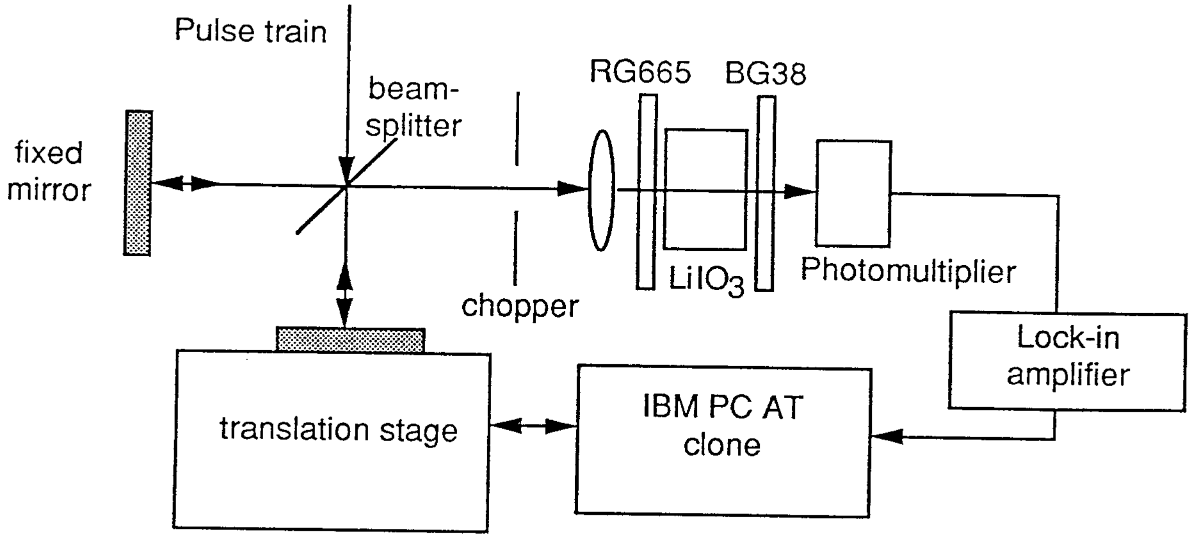

Figure 3.4: Collinear autocorrelation system.

The autocorrelation system is shown in figure 3.4. An optical signal is split into two equal intensity beams, and the delay in one arm is swept by a stepper motor. The beams recombine collinearly and enter a $LiIO_3$ crystal after propagating through a cutoff filter that passes only infrared wavelengths. The light generated in the $LiIO_3$ crystal is then filtered to pass only the second harmonic light, whose average intensity is used to determine the autocorrelation [2]. The essential features of this measurement are explained here to emphasize the difference between measurements of randomly phased modes and high repetition rate pulse trains.

The electric field incident on the $LiIO_3$ crystal is:

$$E^{\omega}(t) = \varepsilon_1(t)e^{i\omega t} + \varepsilon_1(t+\tau)e^{i\omega(t+\tau)} + c.c. \tag{3.1}$$

The second harmonic field is proportional to:

$$E^{2\omega}(t) = \varepsilon_2 e^{2i\omega t} + c.c. \tag{3.2}$$

where

$$\varepsilon_2 = \varepsilon_1^2(t) + 2\varepsilon_1(t)\varepsilon_1(t+\tau)e^{i\omega\tau} + \varepsilon_1^2(t+\tau)e^{2i\omega\tau}. \tag{3.3}$$

The current generated by the photomultiplier is proportional to the intensity of the second harmonic field and is averaged over a time period much longer than the pulse duration.

$$\begin{aligned} i_d \propto\ & < \varepsilon_1^2(t)\varepsilon_1^{*2}(t) > +4 < \varepsilon_1(t)\varepsilon_1(t+\tau)\varepsilon_1^*(t)\varepsilon_1^*(t+\tau) > + < \varepsilon_1^2(t+\tau)\varepsilon_1^{*2}(t+\tau) > + \\ & f_1(t,\tau)e^{i\omega\tau} + f_2(t,\tau)e^{2i\omega\tau} \end{aligned} \tag{3.4}$$

The terms with factors of $e^{i\omega\tau}$ and $e^{2i\omega\tau}$ are averaged out either by sweeping the delay fast enough or slightly misaligning the two beams to obtain several interference fringes, so that the averaged voltage from the lock-in amplifier is then proportional to a background level added to twice the second order intensity autocorrelation, $1 + 2G^{(2)}(\tau)$, where

$$G^{(2)}(\tau) = \frac{\int_{-\infty}^{\infty} I(t)I(t+\tau)dt}{\int_{-\infty}^{\infty} I^2(t)dt}. \tag{3.5}$$

For an ultrashort pulse, $G^{(2)}(\tau)$ goes to zero for $\tau >> \tau_p$, where τ_p is the pulsewidth, and the ratio of the peak signal to the background signal is 3 to 1. However, if the optical signal consists of randomly phased modes, instead of a pulse train, the intensity distribution will be approximately

$$p(I) = \frac{1}{<I>}e^{-I/<I>} \tag{3.6}$$

with increasing accuracy as the number of modes increases [3], and the optical signal will be periodic, changing slowly due to lower frequency intensity fluctuations, so that for delays of several inverse mode spacings, the autocorrelation will appear periodic, with a frequency equal to the laser mode spacing. Using $p(I)$ it can be shown that the peak to background signal ratio for a pure noise signal is 3 : 2, while in the case of background free autocorrelation measurements, where the input beams are not collinear, the peak to background ratio is 2 : 1.

3.4 Experimental results

3.4.1 108 GHz passive mode-locking of a GaAs/AlGaAs laser

The structure of the laser used in this experiment is very similar to one used earlier for active Q-switching [4], and is shown in figure 3.5. This laser has three 75 Å quantum wells, a parabolically graded index waveguide, and $Al_{0.5}Ga_{0.5}As$ in the cladding layers. The laser structure is defined by etching a 3-5 μm wide stripe, using a 5 μm wide mask and the 1:3:40 etch described in appendix A for 14 minutes at room temperature. The gain section is approximately 245 μm long, and the absorber is 90 μm, with the sections separated by a 5-7 μm wide etch through the highly conductive cap layer, giving 5 kΩ electrical isolation. With the absorber section open circuited, this device has a threshold current of 30 mA.

Pulses at a repetition frequency exceeding 100 GHz are produced by reverse biasing the absorber section and forward biasing the gain section with 3.8 μsec electrical

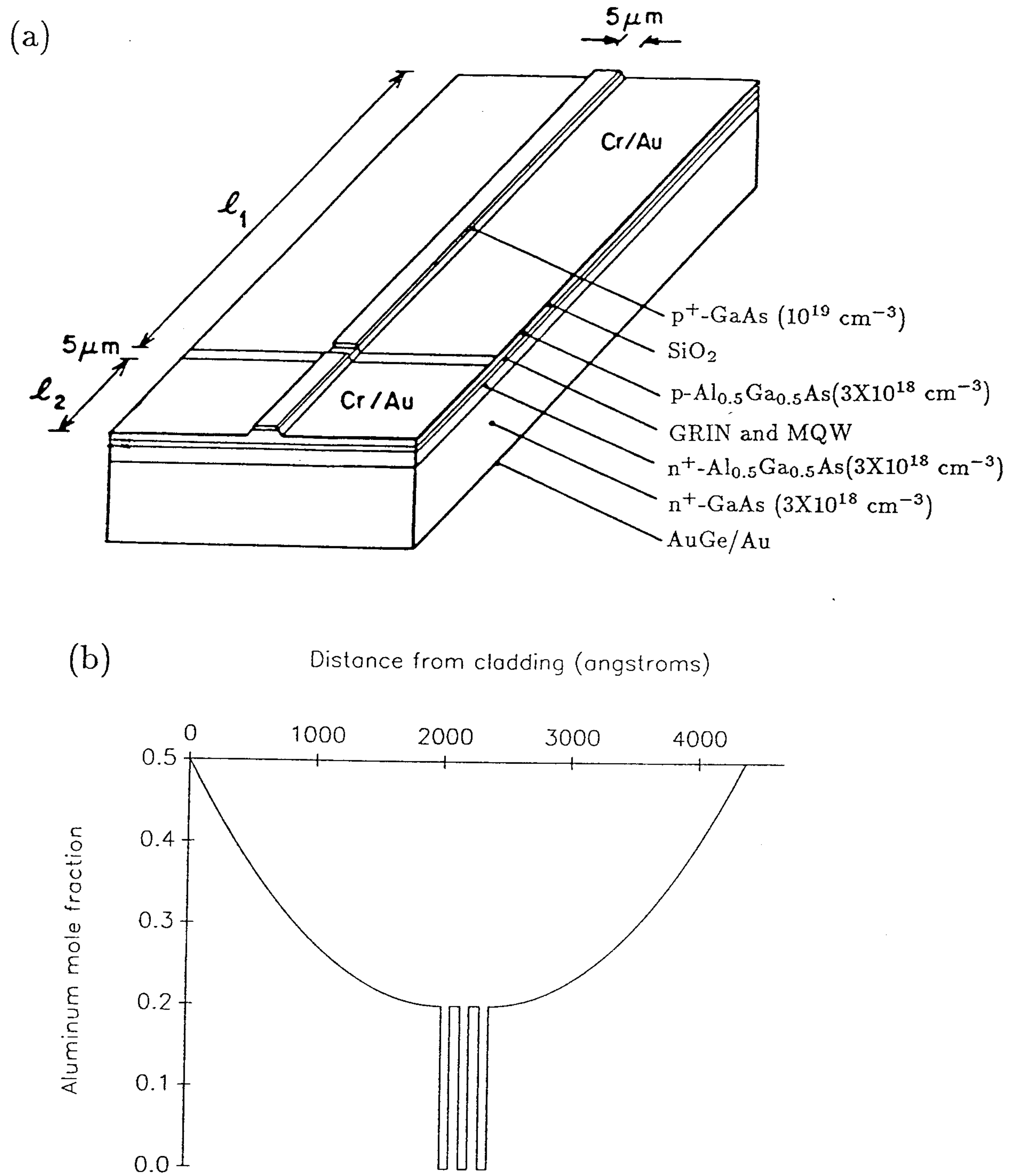

Figure 3.5: Two-section GaAs/AlGaAs laser: (a) laser structure; (b) quantum well and graded index region.

pulses. Data are taken using the streak camera in its single shot mode, and the intensity is integrated over the width of the slit illuminated by the laser diode, after correcting for the dark current in the readout system. All observations are of the gain section end of the laser diode.

Figure 3.6(a) shows the light output when the absorber has a bias of -0.67 V, and the gain section is given 90 mA current pulses. The average light pulse spacing is 9.3±0.4 ps, corresponding to a 108 GHz repetition rate. The power spectrum calculated from the streak image, which gives 6 GHz resolution due to the short observation time, is shown in figure 3.6(b) and is peaked at 109 GHz. Many pulses show full widths at half-maximum (FWHM) of 2 ps, the resolution limit of the camera, and the average pulse width, convolved with the streak camera response, is 2.4 ps, with a standard deviation of 0.7 ps. There is substantial variation in the pulse shapes on this trace and on others, and it is not clear how much fluctuation is due to the laser and how much is due to noise in the streak camera. Shot noise from the photocathode is substantial since a single channel sees signal from only tens of photoelectrons at the peak powers, which are estimated from the average power to be 30 mW. Pulse trains as long as 450 ps, the maximum time range of the streak camera for which there is sufficient resolution, have been observed, as shown in figure 3.7. The optical spectrum, shown in figure 3.8, has a FWHM of 470±40 GHz, giving a time-bandwidth product of <1.1±0.3. The average mode spacing, determined under slightly lower forward bias where the mode structure is clearer, is 2.63 ± 0.09 Å, which is 107 ±4 GHz at 0.86 μm.

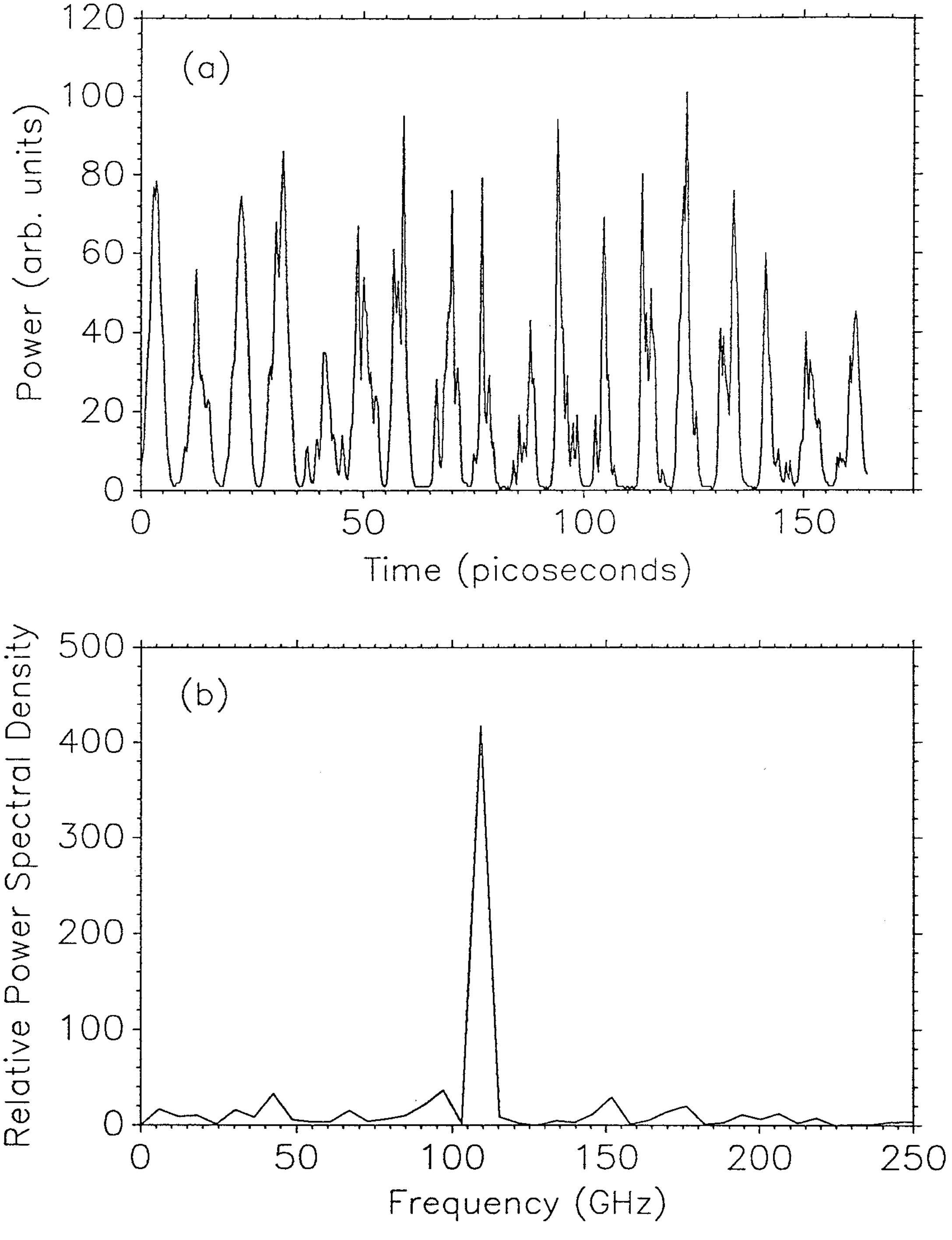

Figure 3.6: (a) Streak camera observation of 108 GHz pulse train; (b) power spectrum of (a) with DC level subtracted; $I_g = 90mA; V_a = -0.67V$.

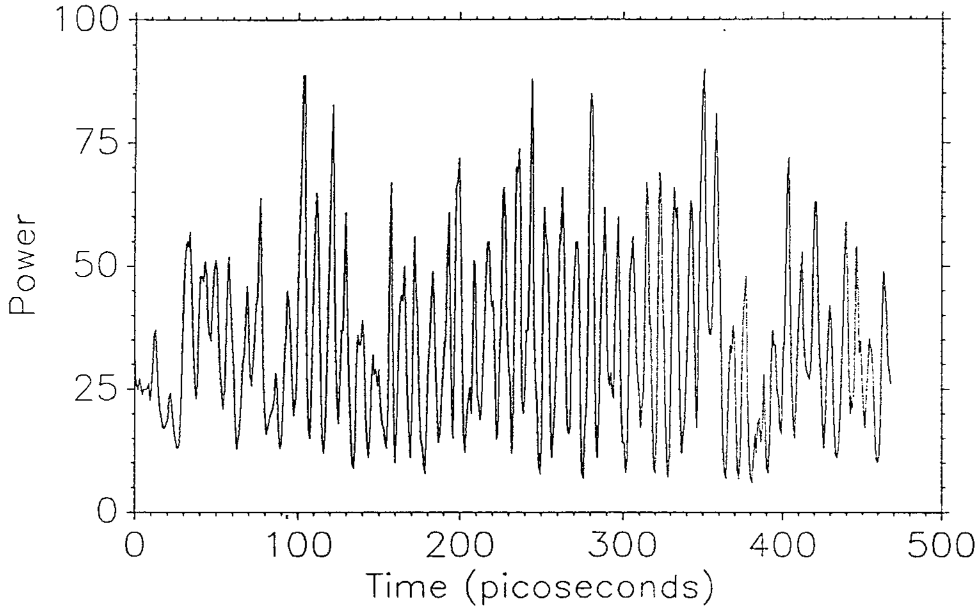

Figure 3.7: Streak image of pulse train at 6 ps resolution showing sustained modulation.

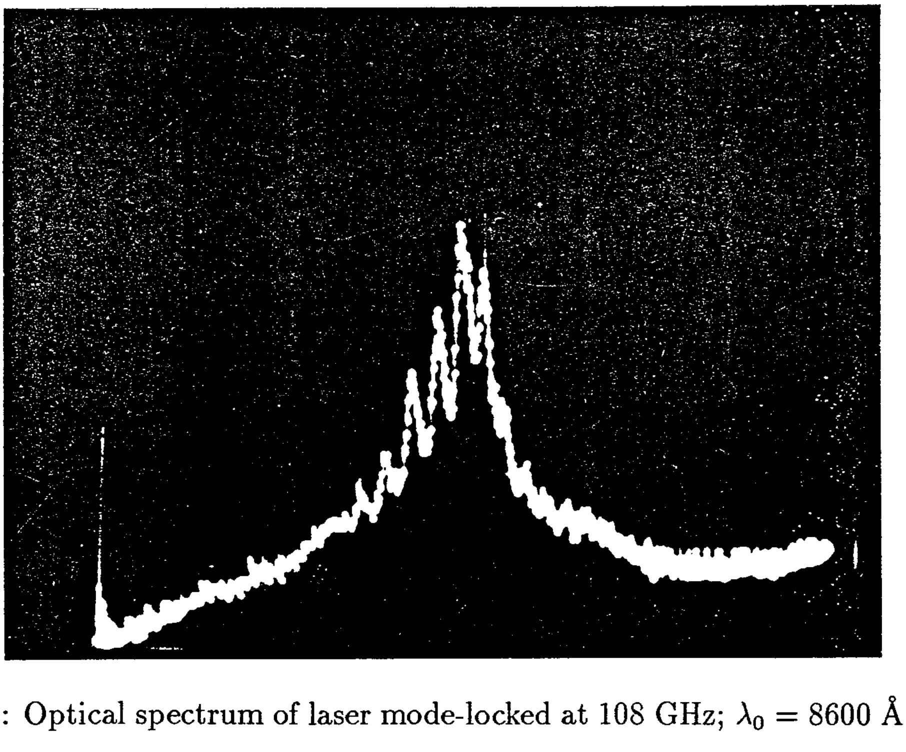

Figure 3.8: Optical spectrum of laser mode-locked at 108 GHz; $\lambda_0 = 8600$ Å; FWHM $= 470$ GHz; $\Delta = 107 \pm 4$ GHz.

The best pulse stability and lowest time-bandwidth products are observed for absorber biases around -0.6 to -0.8 volts; as the absorber bias is made more negative, individual modes and the entire spectrum broaden. For an absorber bias of -1.09 V and a forward bias of 105mA, the spectrum broadens to 30 Å and the center wavelength shifts to 8630 Å.

Under slightly different pumping conditions, the laser displays self-sustained pulsations. With the absorber bias fixed, and the gain section current below that necessary for mode-locking, the laser emits pulses at less than 2 GHz. When the current is raised to levels above where mode-locking occurs, pulses at frequencies up to 8 GHz are observed.

In figure 3.9, the different modes of behavior displayed by this laser are shown as the gain section current is increased, with the absorber bias fixed at -0.80 V. At threshold, 60 mA, the laser pulses at 0.6 GHz, and as the current is increased, the pulsation frequency increases, as expected from the decrease in the stimulated carrier lifetime at higher photon densities. As the current is increased to 95mA, a transition is observed to passive mode-locking. At 82mA, double pulses are seen at irregular intervals, and at 90mA, mode-locked pulse trains are seen on some streak images, while large, slower pulsations are seen on others. The mode-locked pulse train is sustained from streak image to streak image at 95mA and remains so until 120mA, where self-pulsations at 6 GHz with a higher frequency substructure are observed. As the current is further increased, the self-pulsations are no longer seen, and the output shows unstable periodic structure, as shown at 140 mA.

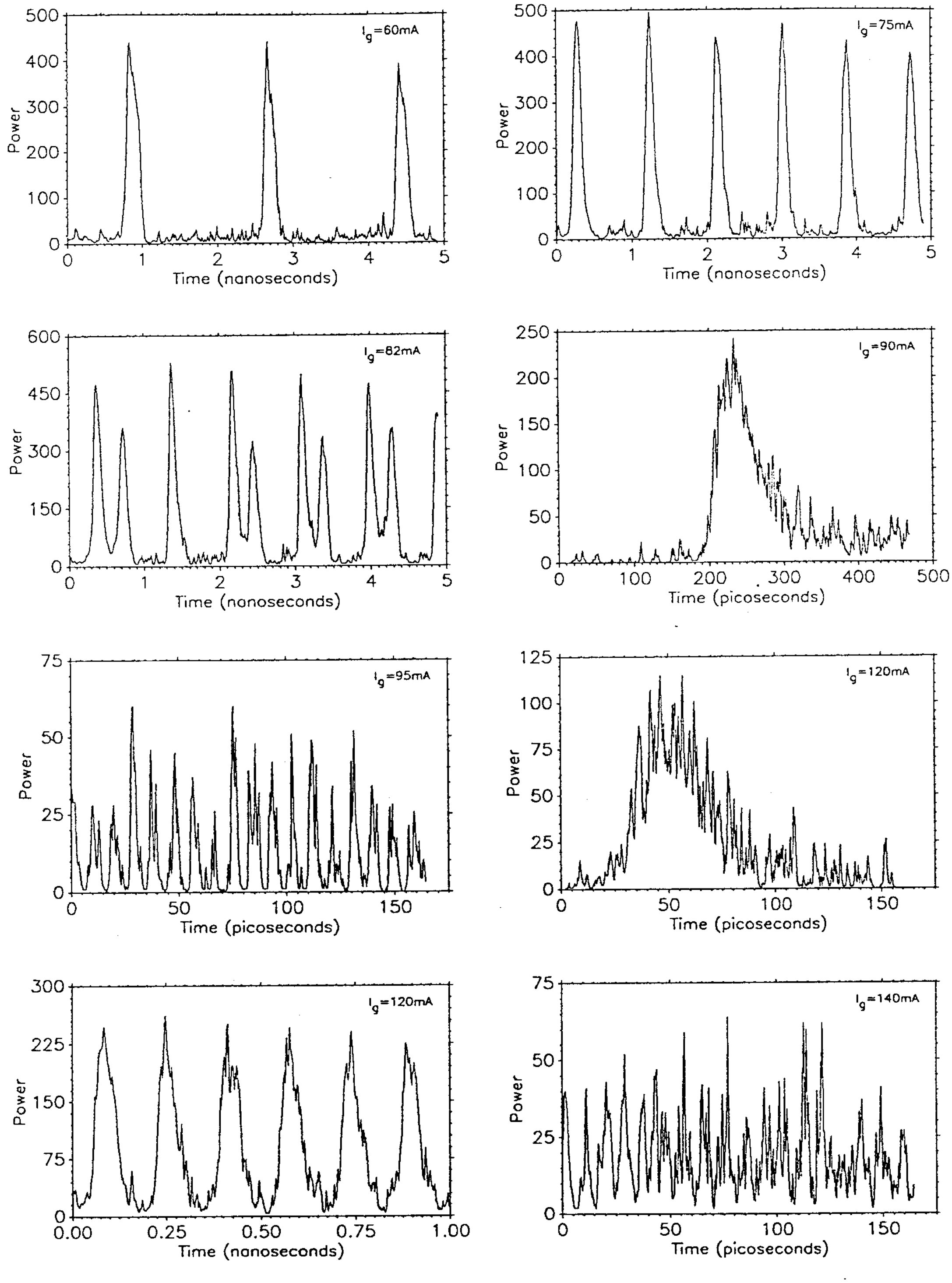

Figure 3.9: Laser output as a function of gain current for absorber bias fixed at -0.80 V.

3.4.2 42 GHz passive mode-locking of InGaAs/AlGaAs lasers

While some of the observed instability in the 108 GHz pulse train can be attributed to streak camera noise, it is clear that there are large pulse-to-pulse energy fluctuations. Greater stability can be achieved in longer lasers, which have higher photon lifetimes, making them less susceptible to self-sustained pulsations and large relaxation oscillations, as discussed in Chapter 2. It is demonstrated that lasers made from strained InGaAs/AlGaAs double quantum well material can be passively mode-locked to produce pulses at 9850 Å, with substantially more stable pulse trains when the repetition rate is reduced to 42 GHz, by cleaving longer devices. It is possible that the larger decrease of differential gain with increasing carrier density expected from the strained-layer InGaAs/AlGaAs compared to GaAs/AlGaAs lasers may allow mode-locking at higher repetition rates [5], but such enhancements have not yet been systematically investigated.

The laser, illustrated in figure 3.10, is grown by molecular beam epitaxy on an n-type GaAs substrate and consists of a 1.5 μm n-type $Al_{0.5}Ga_{0.5}As$ cladding layer, the graded-index and double quantum well region, a 1.5 μm p-type $Al_{0.5}Ga_{0.5}As$ layer, and a 2000Å heavily p-doped cap layer. The double quantum well structure consists of two 50Å InGaAs layers spaced by a 100Å GaAs barrier, between two 40Å GaAs layers. Each graded index region is 2000Å thick.

The laser mesa is formed by etching 3 μm wide stripes to a depth of 1.2 μm,

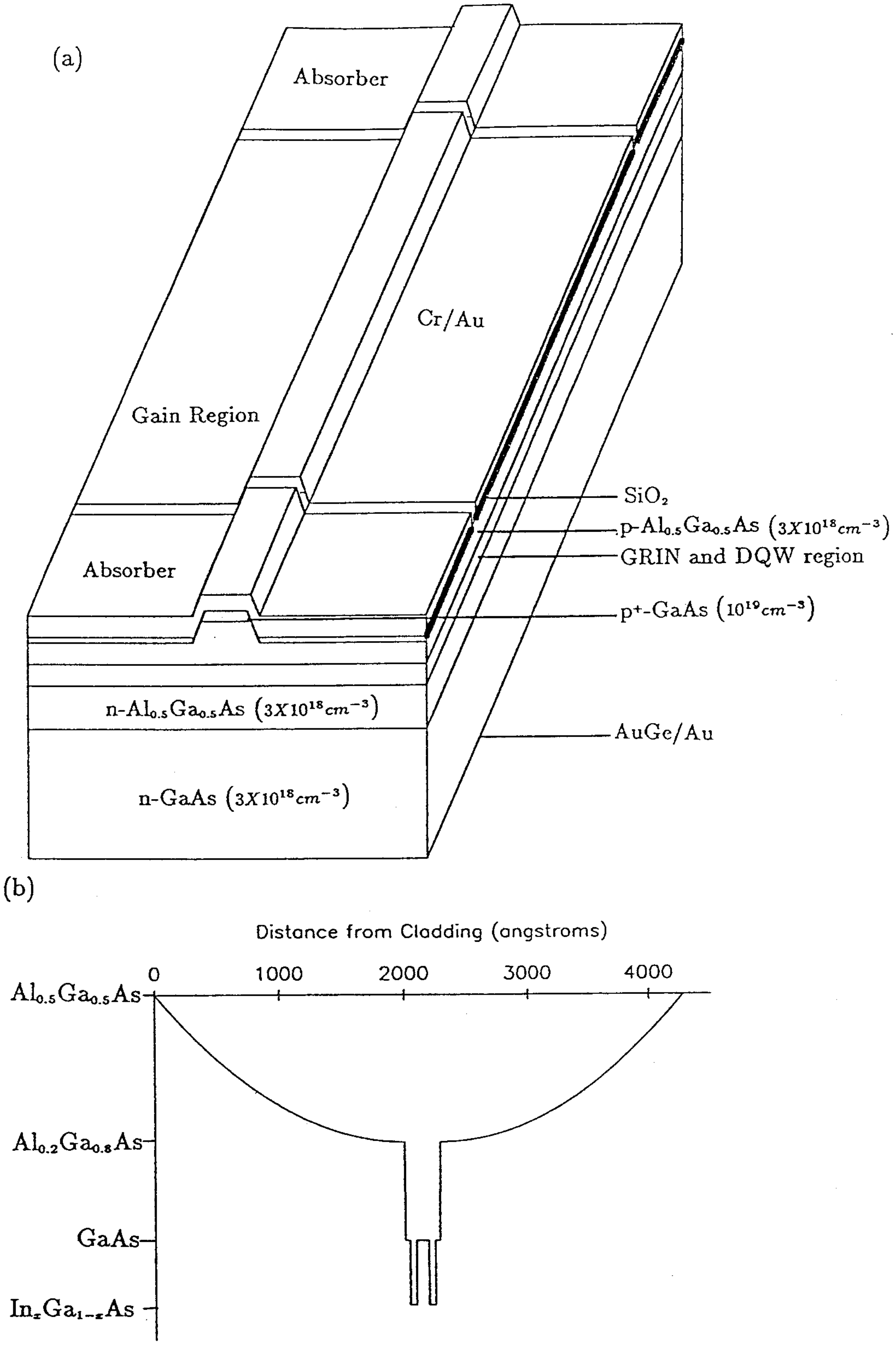

Figure 3.10: (a) Structure of 3-section InGaAs/AlGaAs laser; (b) graded index and double quantum well region.

using a 5 μm wide mask. The top metallization is defined by liftoff, leaving 20 μm gaps between the sections, and electrical isolation of 1 kΩ is effected by etching 7 μm gaps through the cap layer. The gain region is 595 μm long, and the front and rear absorbers are 140 μm and 180 μm long respectively. The gain region is driven by 50 μsec electrical pulses, while the front absorber is left open-circuited and the rear absorber DC biased through a 100Ω series resistor, across which the current is measured by sample-and-hold amplifiers while the gain section current is on. Measurements are typically performed 25 μsec after the start of the gain section pulse, and the pulse trains are less susceptible to relaxation oscillations when the front absorber is left open-circuited than when it is driven in parallel with the gain region. The primary effect of the floating absorber is to extend the cavity length, since it is bleached close to transparency by the light in the cavity.

The average output power as a function of current is shown in figure 3.11 for two bias conditions. In curve (a), all three sections of the laser are driven in parallel, and the threshold current is 28 mA, with a linear dependence of output power on current above threshold and a differential external quantum efficiency of 60%. When the rear absorber is reverse biased, a light jump occurs at threshold. At higher gain currents, where the absorber is becoming more saturated, there is another large differential increase in light output, after which conditions where passive mode-locking can be observed are reached. At gain section currents above 145 mA, the power drops, and streak camera measurements show self-sustained pulsations.

The ouput from the front facet is measured using the streak camera in its single-

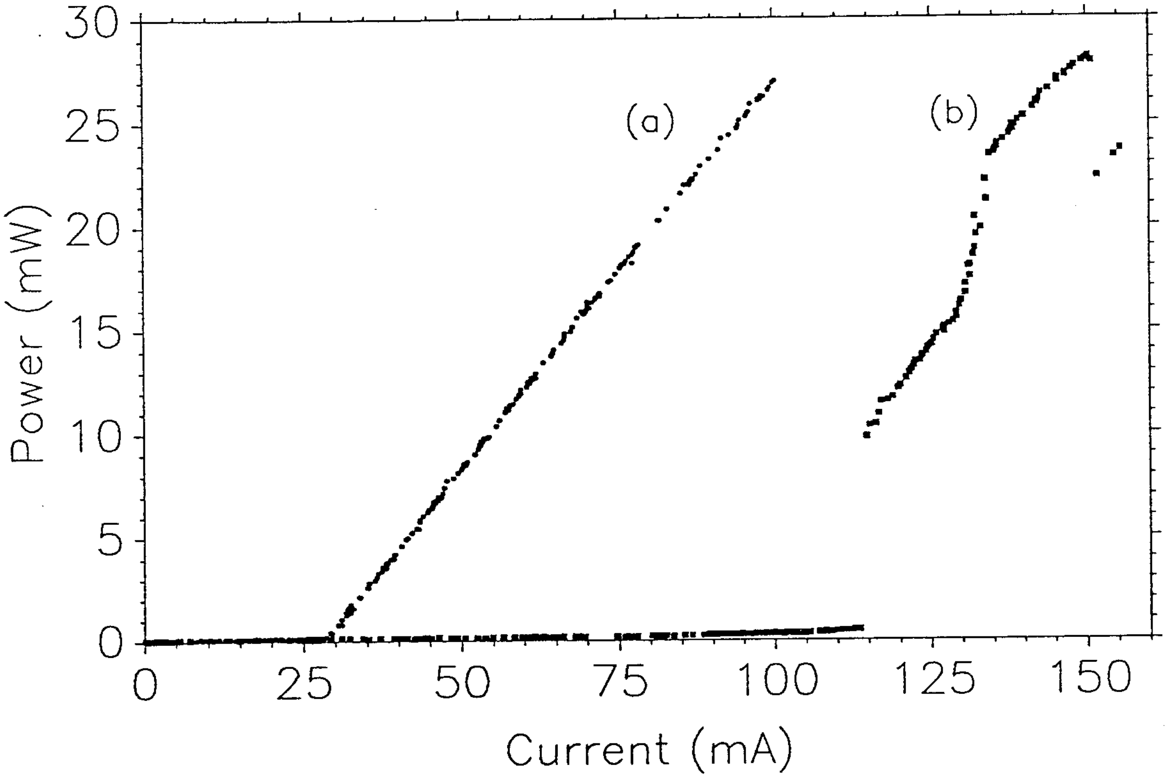

Figure 3.11: Average output power vs. current for (a) all three sections driven in parallel and (b) rear absorber reverse biased.

shot mode. Figure 3.12 shows typical pulse trains near optimum bias conditions on the three fastest streak scales. The pulsewidths average 5.9 ps, and have a 42 GHz repetition rate. The average peak power is approximately 80 mW, and the modulation depth exceeds 98%. Integrating under the peaks in figures 3.12(a) and 3.12(b) gives standard deviations in the pulse energies of 9% and 14% respectively, while photocathode shot noise can account for about a 3% deviation. Other sources of the variations include lower frequency intensity relaxation oscillations, amplified spontaneous emission noise, and inhomogeneities in the streak camera system. Only a small number of pulses are compared, however, and more accurate noise characterization will require measurements over longer time periods, possibly using a very fast photodetector and spectrum analyzer. The optical spectra were typically very broad, with full-widths at half-maximum of 400 GHz or higher, and centered near 9850Å.

The ranges of both gain and absorber current where mode-locking is consistently observed are shown in figure 3.13. To perform these measurements, the gain section current is held fixed, while the absorber bias is swept in the negative direction. First, the output is unmodulated or shows some unstable structure at frequencies near the cavity mode spacing. At stronger bias, the current flowing out of the absorber continues to increase, and the output appears similar to that in figure 3.12. The sustained pulse train remains until the absorber bias is increased to where the laser self-pulsates, at which point the current flowing out of the absorber drops by several milliamperes. A second laser on the same cleaved bar had almost the same locking ranges. Except for the pulsation at very high gain currents, the locking and self-

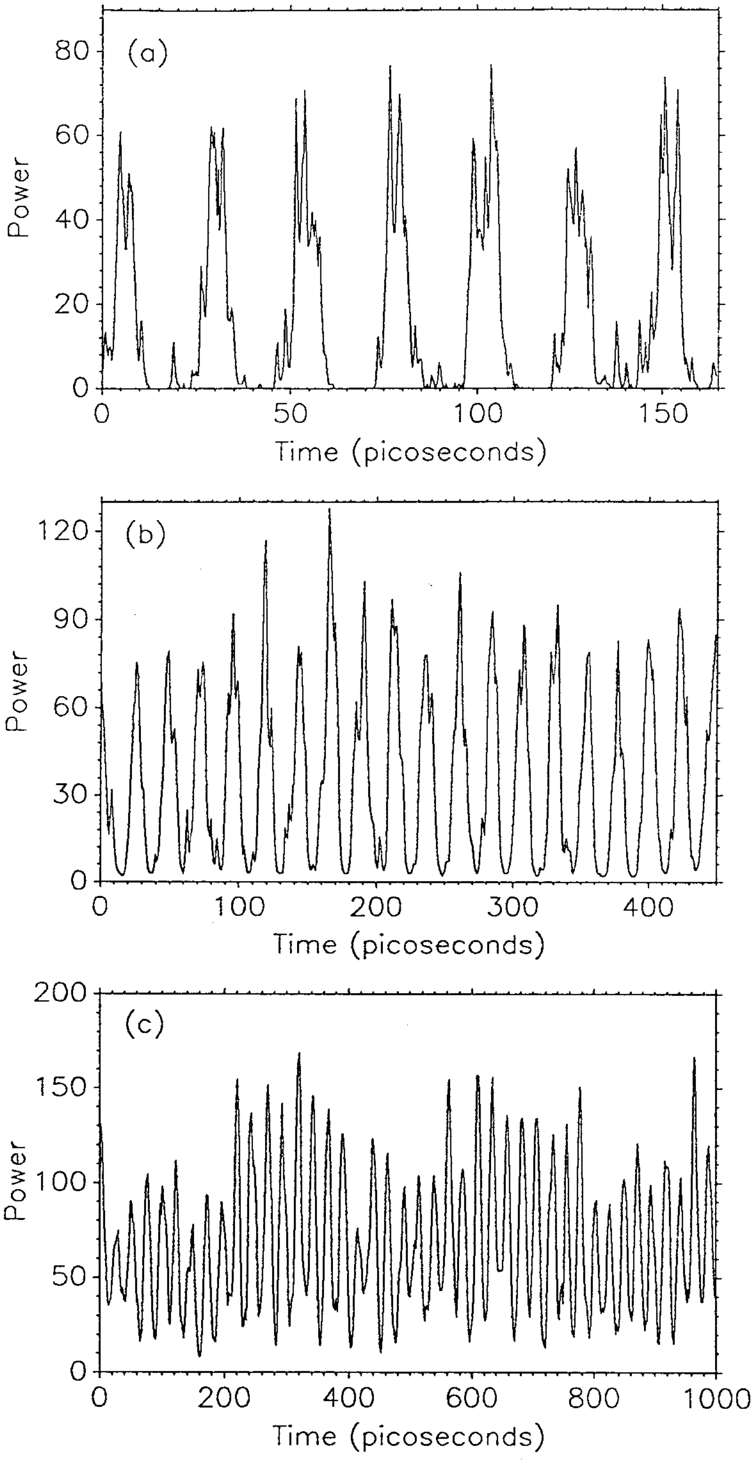

Figure 3.12: Optical pulse trains from mode-locked InGaAs laser with $I_g = 140mA$ and $I_r = -24.3mA$ (a) 2 ps resolution, (b) 6 ps resolution, (c) 12 ps resolution.

pulsing ranges are qualitatively consistent with those predicted from the mode-locking theory of Chapter 2, as shown in figure 2.4. The larger reverse bias corresponds to a faster absorber recovery time, and higher gain current results in higher output power levels.

Self-sustained pulsation and large relaxation oscillations greatly limit the range of stable passive mode-locking in this and other devices. A shorter, two-section laser, whose output is shown in figure 3.14, displays a 4 GHz, 80% modulation in the envelope of the mode-locked pulse train, indicating that the modes remain in phase while their amplitudes oscillate. Under some conditions, the laser mode-locks at its second harmonic, as shown in figure 3.15. Picosecond pulses were generated at rates up to 100 GHz in InGaAs lasers, and evidence for mode-coupling at rates up to 130 GHz in GaAs lasers was observed, as shown in figure 3.16, but the trains were very unstable and not present on all streak shots.

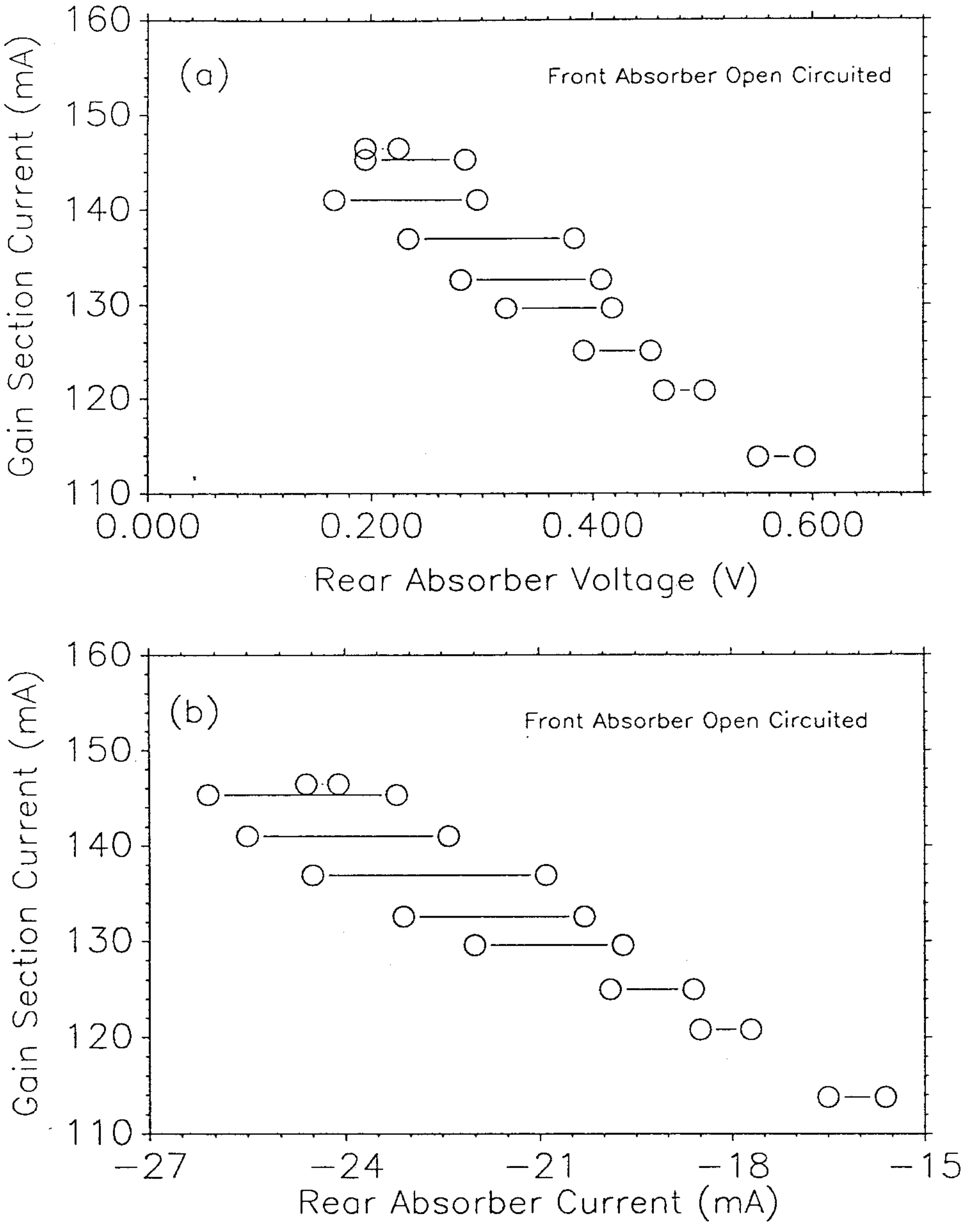

Figure 3.13: Ranges for passive mode-locking for gain section current and: (a) voltage at absorber contact; (b) absorber current.

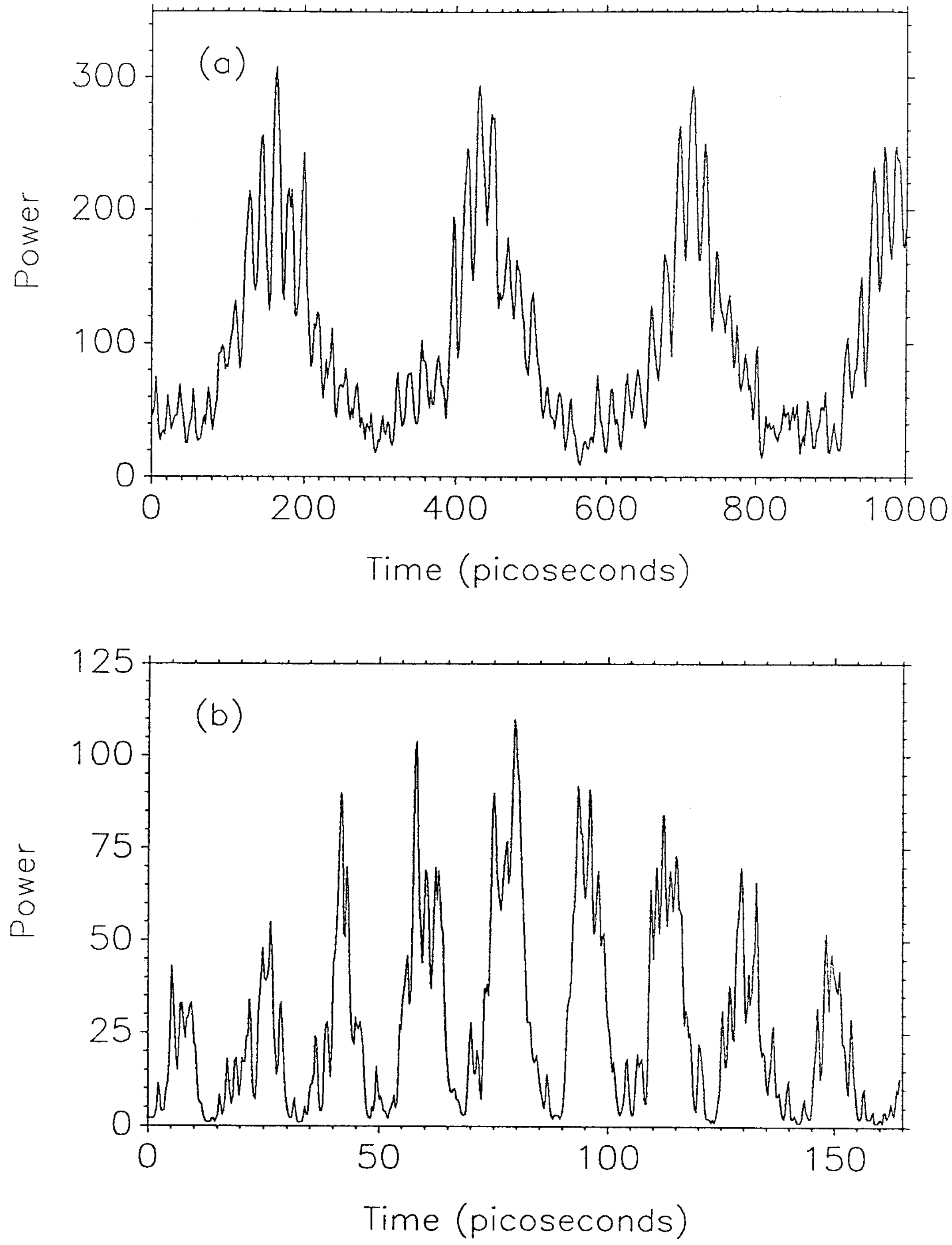

Figure 3.14: Simultaneous self-sustained pulsation at 4 GHz and mode-locking at $\sim$ 60 GHz; $I_g = 84mA; I_a = -13.9mA$.

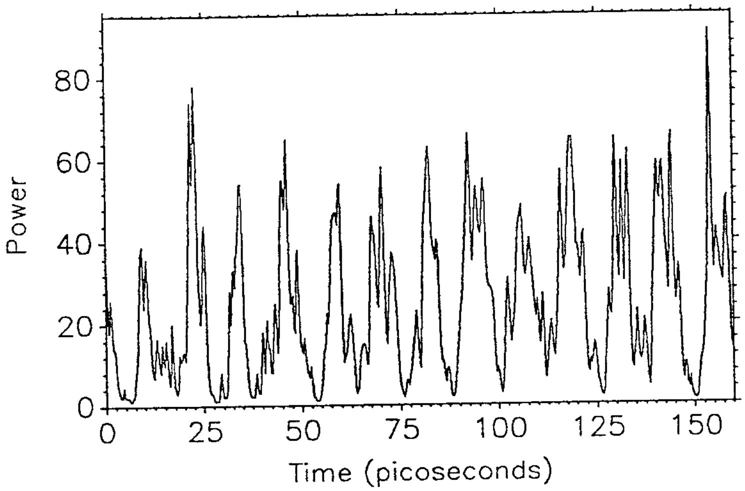

Figure 3.15: InGaAs laser passively mode-locked at its second harmonic of 84 GHz; $I_g = 152\text{mA}; I_a = -20.5\text{mA}$.

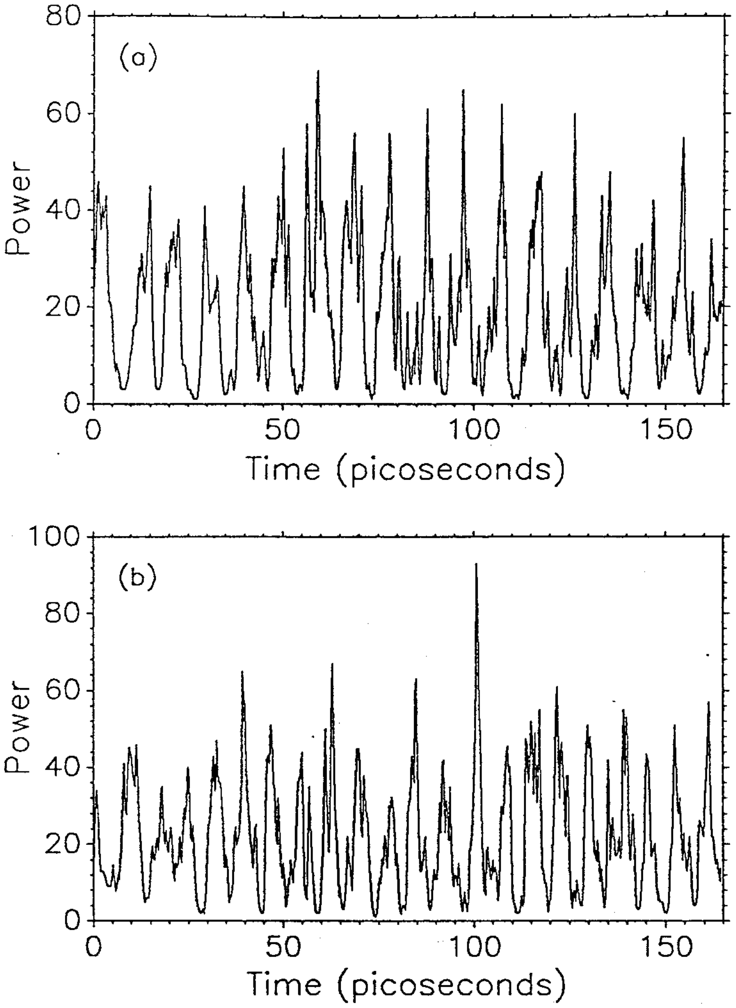

Figure 3.16: Unsustained passive mode-locking of (a) InGaAs laser at 100 GHz and (b) GaAs laser at 130 GHz.

References

[1] Y. Tsuchiya, H. Suzuki, M. Koishi, K. Kinoshita and T. Nakamura, *Proceedings of SPIE*, **569**, 181 (1985).

[2] A. Yariv, **Optical Electronics**, 3rd ed., Wiley, 173 (1985).

[3] J.W. Goodman, **Statistical Optics**, Wiley, ch. 4 (1985).

[4] Y. Arakawa, A. Larsson, J. Paslaski and A. Yariv, *Appl. Phys. Lett.*, **48**, 561 (1986).

[5] K.Y. Lau, S. Xin, W.I. Wang, N. Bar-Chaim and M. Mittelstein, *Appl. Phys. Lett.*, **55**, 1173 (1989).

Chapter 4

Passive mode-locking of external cavity quantum well lasers

4.1 Introduction

In Chapters 2 and 3, it was shown theoretically and experimentally that monolithic passively mode-locked quantum well lasers can generate picosecond pulse trains at repetition rates in excess of 100 GHz. However, at these high frequencies, pulsewidth limitations arise from the small degree of gain and absorber saturation, and large instabilities in the pulse train are often present. By coupling the two-section multiple quantum well laser to an external cavity, as shown in figure 4.1, the repetition rate can be reduced to allow large absorber and gain recovery between pulses, with the net result of much greater saturation under steady-state mode-locked operating conditions and the locking of hundreds of cavity modes to produce pulses that are very short

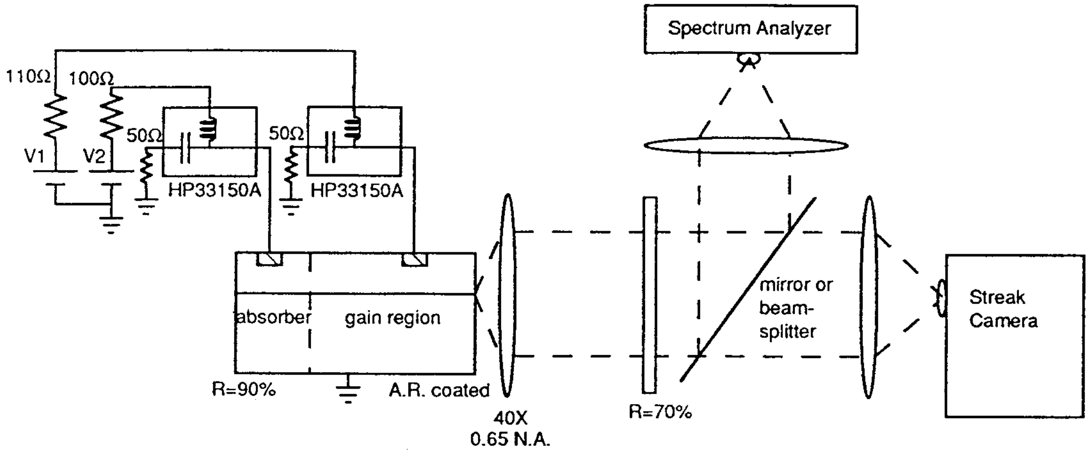

Figure 4.1: Two-section quantum well laser coupled to an external cavity.

compared to the spacing between them. Pulsewidths as short as 5 ps have been observed from these external cavity quantum well lasers; the lower repetition rate pulse trains are more compatible with conventional electronics, and can be studied in greater detail to assess amplitude and timing stability. For the first time, it is quantitatively demonstrated that a passively mode-locked semiconductor laser can produce pulse trains with low timing jitter and very small pulse energy fluctuations.

To theoretically analyze the basic operation of this laser, the earlier assumption from Chapter 2 of small-signal saturation is abandoned, and a pulse is followed in a time-domain analysis as it passes through the different regions of the cavity. Changes in the pulse energy and in the gain and absorption are calculated, and conditions for stable pulse generation are derived. These conditions are much more stringent than those of the high repetition rate analyses, for they require that the pulse be compressed on every pass through the cavity, until it becomes limited by effects of dispersion, chirp, and gain bandwidth. From the large quantum well gain spectrum, it would be expected that pulses on the order of 10-100 femtoseconds could be produced, but experimental results are still two orders of magnitude longer. Some of the discrepancy can be attributed to dispersion and to chirping due to the dependence of refractive index upon carrier density and to the shifting of the gain and absorption spectra during saturation by the pulse, but a complete quantitative explanation still does not exist. The goal of the theories in this chapter is to calculate conditions on the material, cavity, and external bias parameters where passive mode-locking occurs, such that a pulse circulating through the cavity always sees net loss at its leading and trailing edges. The pulse width will not be calculated in these theories, since the effects of dispersion and chirp are neglected, resulting in the prediction that the pulse width should be limited only by the system bandwidth. However, the conditions for stable passive mode-locking will be determined, from which future experimental and theoretical work should lead to stable subpicosecond pulses.

4.2 Strong saturation passive mode-locking theory: analytic model

With the cavity extended so that the pulse is much shorter than the round-trip time and so that the gain and absorber media occupy only a small fraction of the cavity length, the passive mode-locking problem can be divided into two simpler parts. A pulse circulating in the cavity passes through the regions of gain and absorption in the semiconductor laser, saturating them at a rate much faster than their recovery, which, therefore, can be neglected during this time. The degree of saturation before any given point on the pulse passes through depends upon the preceding fluence, so the net gain experienced by different regions of the pulse will vary. When the pulse propagates in the external cavity, the gain and absorber recover until the pulse returns to the semiconductor laser and saturates them again. The pulse will see losses due to the mirrors and imperfect coupling with the semiconductor laser, and in the steady-state, the pulse and saturation dynamics will be periodic, at approximately the round-trip time of the composite semiconductor laser and external cavity. Stable mode-locking occurs when the leading and trailing edges of the pulse see net loss in a round-trip while part of the pulse sees net gain. Under steady-state conditions, the dispersion due to bandwidth limitation causes the energy gained in a round-trip by the peak of the pulse to spread into its wings, so that all parts of the pulse see unity net gain.

The two-section quantum well laser is analyzed by applying Haus' original theory of passive mode-locking with a slow saturable absorber [1,2], which gives analytic solutions for mode-locking conditions and pulse shape. This theory is primarily intended to show approximate trends in the mode-locking conditions, since it is only quantitatively valid for small cavity losses. A model for the cavity is illustrated in figure 4.2, where the dispersive element represents the system bandwidth. Summing the cavity modes of Chapter 2, the electric field can be represented as:

$$E(t) = v(t)e^{i\omega_0 t} \tag{4.1}$$

where ω_0 is the center lasing frequency; t is the local time on the pulse, and $v(t)$ is the envelope of the field, normalized so that $v^2(t)$ is equal to $s(t)$, the photon intensity. During one round trip, the pulse will travel twice through the gain medium and absorber medium, be dispersed by the bandwidth limiting element, and have linear losses due to the mirrors and internal scattering. In addition, there may be a shift in the pulse repetition rate from the cavity round trip time due to shaping of the pulse in the saturable media. A reference plane is chosen between the bandwidth limiting element and the gain section, and a pulse traveling to the left is followed. After one round-trip pass through the semiconductor laser, the electric field envelope will be:

$$v_2(t) = e^{\frac{g(t)}{2}l_g} e^{\frac{a(t)}{2}l_a} e^{\frac{a(t)}{2}l_a} e^{\frac{g(t)}{2}l_g} v_1(t) \tag{4.2}$$

where only the saturation due to the double passage of earlier parts of the pulse is considered, so that $a(t)$ and $g(t)$ are the same during both passes. While propagating through the rest of the cavity, the pulse is modified by the linear losses and the bandwidth limiting element to give:

$$v_3(t) = \exp[(\frac{-T_r}{2\tau_p})(1 - \frac{1}{\omega_c^2}\frac{d^2}{dt^2})]v_2(t) \tag{4.3}$$

where T_r is the round-trip time, and the bandwidth-limiting lineshape transforms from

$$1 + (\frac{\omega_k - \omega_0}{\omega_c})^2 \tag{4.4}$$

to

$$1 - \frac{1}{\omega_c^2}\frac{d^2}{dt^2} \tag{4.5}$$

in the time domain. Assuming that the single pass gain and loss are small enough to be expanded to first order, which is acceptable for low loss cavities, the condition that the pulse repeat itself after a round-trip can be expressed by the nonlinear integro-differential equation:

$$[\tilde{g}(t) + \tilde{a}(t) - 1 + \frac{1}{\omega_c^2}\frac{d^2}{dt^2} - \delta\tau(\frac{2\tau_p}{T_r})\frac{d}{dt}]v(t) = 0. \tag{4.6}$$

Using the quantum well laser model developed in Chapter 2, the saturation and recovery can be described by the equations:

$$\frac{d\tilde{g}}{dt} = \frac{\tilde{g}_0 - \tilde{g}}{\tau_g} - \tilde{g}Gs(t) \tag{4.7}$$

$$\frac{d\tilde{a}}{dt} = \frac{\tilde{a}_0 - \tilde{a}}{\tau_a} - \tilde{a}As(t) \tag{4.8}$$

where $\tilde{a}_0$ and $\tilde{g}_0$ are the unsaturated absorption and gain exponents, respectively, normalized to the linear cavity loss exponent. (In Chapter 2, they represented the

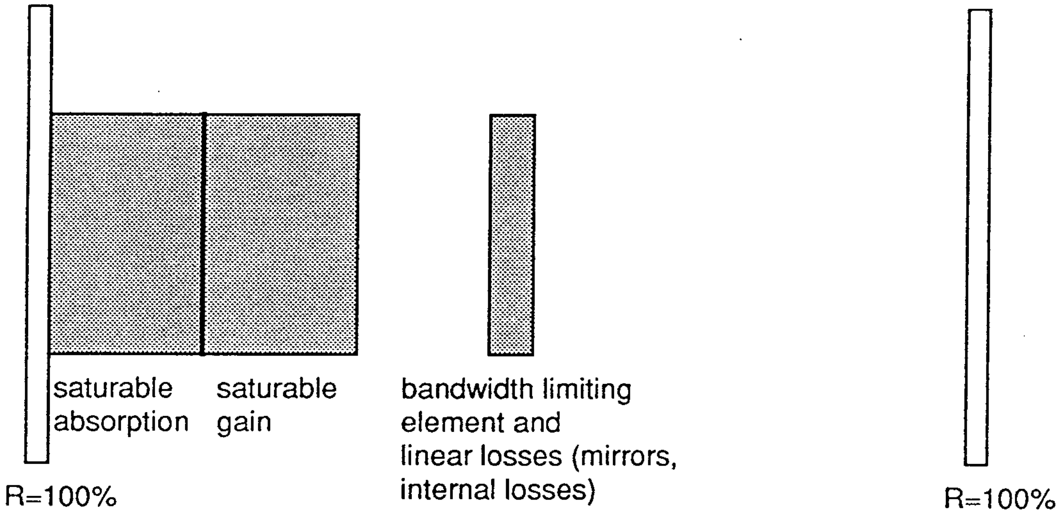

Figure 4.2: Cavity model for analytic passive mode-locking theory.

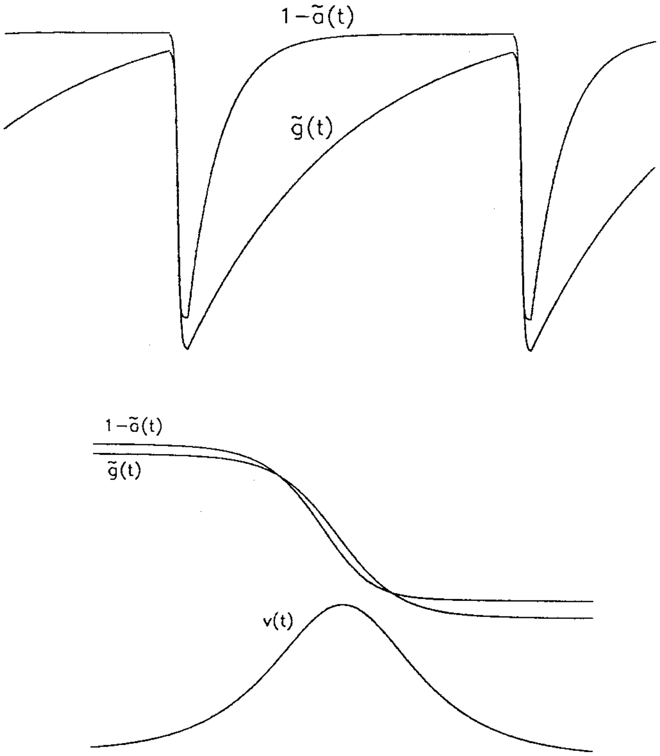

Figure 4.3: Saturation and recovery dynamics: The quantitity $1 - \tilde{a}(t)$ represents the net round-trip normalized loss, and $\tilde{g}(t)$ is the net round-trip normalized gain. As shown in the expanded view of the saturation dynamics, the leading and trailing edges of the pulse see net loss in a round-trip, while the center sees net gain.

DC *saturated* levels.) The gain and absorption are assumed to be linear functions of carrier density in the models in this chapter, but have different first derivatives with respect to carrier density, represented by G and A, respectively as in Chapter 2. During the double-pass saturation, the recovery is neglected so that:

$$\tilde{g}(t) = \tilde{g}_i e^{-2GW(t)} \tag{4.9}$$

and

$$\tilde{a}(t) = \tilde{a}_i e^{-2AW(t)} \tag{4.10}$$

where $\tilde{g}_i$ and $\tilde{a}_i$ are the gain and absorption respectively just before arrival of the pulse, and

$$W(t) = \int_{-\infty}^{t} s(t')dt'. \tag{4.11}$$

The gain and absorber dynamics under stable mode-locking conditions are illustrated in figure 4.3. The essential properties for stable passive mode locking are the lower saturation fluence of the absorption than the gain, and the slower recovery of the gain than the absorption, both achievable using two-section quantum well lasers. For the rest of the analysis, we will assume that the absorber recovers completely between pulses, so that $\tilde{a}_i = \tilde{a}_0$. The gain recovers exponentially between pulses and is periodic under steady-state mode-locking conditions. The gain just before a pulse's arrival can then be related to the unsaturated gain by:

$$\tilde{g}_o = \tilde{g}_i \left(\frac{e^{T_r/\tau_g} - e^{-2U_0/s}}{e^{T_r/\tau_g} - 1}\right) \tag{4.12}$$

where

$$U_0 = AW(\infty). \tag{4.13}$$

Assuming that the exponents in equations 4.9 and 4.10 are small enough to expand them to second order, an analytic solution to equation 4.6 has the form

$$v(t) = \sqrt{\frac{V_0}{2}}\mathrm{sech}(\frac{t}{\tau}) \tag{4.14}$$

where V_0, τ and $\delta\tau$ are determined self-consistently. The determination of V_0 at the limits of $\tilde{g}_i$ for passive mode-locking will allow us to find the corresponding unsaturated gain limits.

To determine mode-locking conditions, we examine the net single pass gain seen by any point on the pulse, which is related to the preceding fluence by:

$$\tilde{g}_T[U(t)] = \tilde{g}_i[1 - 2\frac{U(t)}{s} + 2\frac{U(t)^2}{s^2}] + \tilde{a}_i[1 - 2U(t) + 2U(t)^2] - 1 \tag{4.15}$$

where

$$U(t) = AW(t) \tag{4.16}$$

and $s = \frac{A}{G}$, as in Chapter 2. Stable passive mode-locking requires that the leading edge of the pulse see net loss:

$$\tilde{g}_i + \tilde{a}_i - 1 < 0 \tag{4.17}$$

that the trailing edge of the pulse see net loss:

$$\tilde{g}_i[1 - 2\frac{U_0}{s} + 2\frac{U_0^2}{s^2}] + \tilde{a}_i[1 - 2U_0 + 2U_0^2] - 1 < 0 \tag{4.18}$$

and that the center of the pulse see net gain. To satisfy this last requirement, s must be greater than unity, so that the absorption is saturated more than the gain by the leading edge of the pulse. Net loss for the leading and trailing edges requires maximum and minimum $\tilde{g}_i$ levels respectively for fixed $\tilde{a}_0$. Integrating the square of $v(t)$ in 4.14:

$$W(t) = \frac{V_0}{2}\int_{-\infty}^{t} \operatorname{sech}^2(\frac{t'}{\tau})dt' \tag{4.19}$$

$$= \frac{V_0\tau}{2}[1 + \tanh(\frac{t}{\tau})] \tag{4.20}$$

and using the saturation expansions in equation 4.6, the pulse fluence can be determined from the equations:

$$\tilde{g}_i[1 - \frac{U_0}{s} + \frac{U_0^2}{s^2}] + \tilde{a}_i[1 - U_0 + U_0^2] - 1 + \frac{1}{\omega_c^2\tau^2} = 0 \tag{4.21}$$

$$\tilde{g}_i\frac{U_0^2}{2s^2} + \tilde{a}_i\frac{U_0^2}{2} - \frac{2}{\omega_c^2\tau^2} = 0. \tag{4.22}$$

The passive mode-locking ranges in the $\tilde{a}_0$-$\tilde{g}_0$ plane are shown in figure 4.4, for increasing values of s, showing the larger mode-locking ranges as the absorber saturation intensity becomes smaller relative to the gain saturation intensity. Only ranges where $U_0 \leq 0.5$ are shown, since the second order expansion of the saturation exponentials fails at higher U_0. For mode-locking periods much shorter than the gain recovery time, very high gain levels are required, and for repetition rates that are too slow, the locking ranges are very small, which may lead to unstable pulse trains.

Additionally, we must ensure that the laser will be stable against self-sustained pulsations. By coupling the laser to the external cavity, the photon lifetime is increased to where the analysis of Chapter 2 predicts stability.

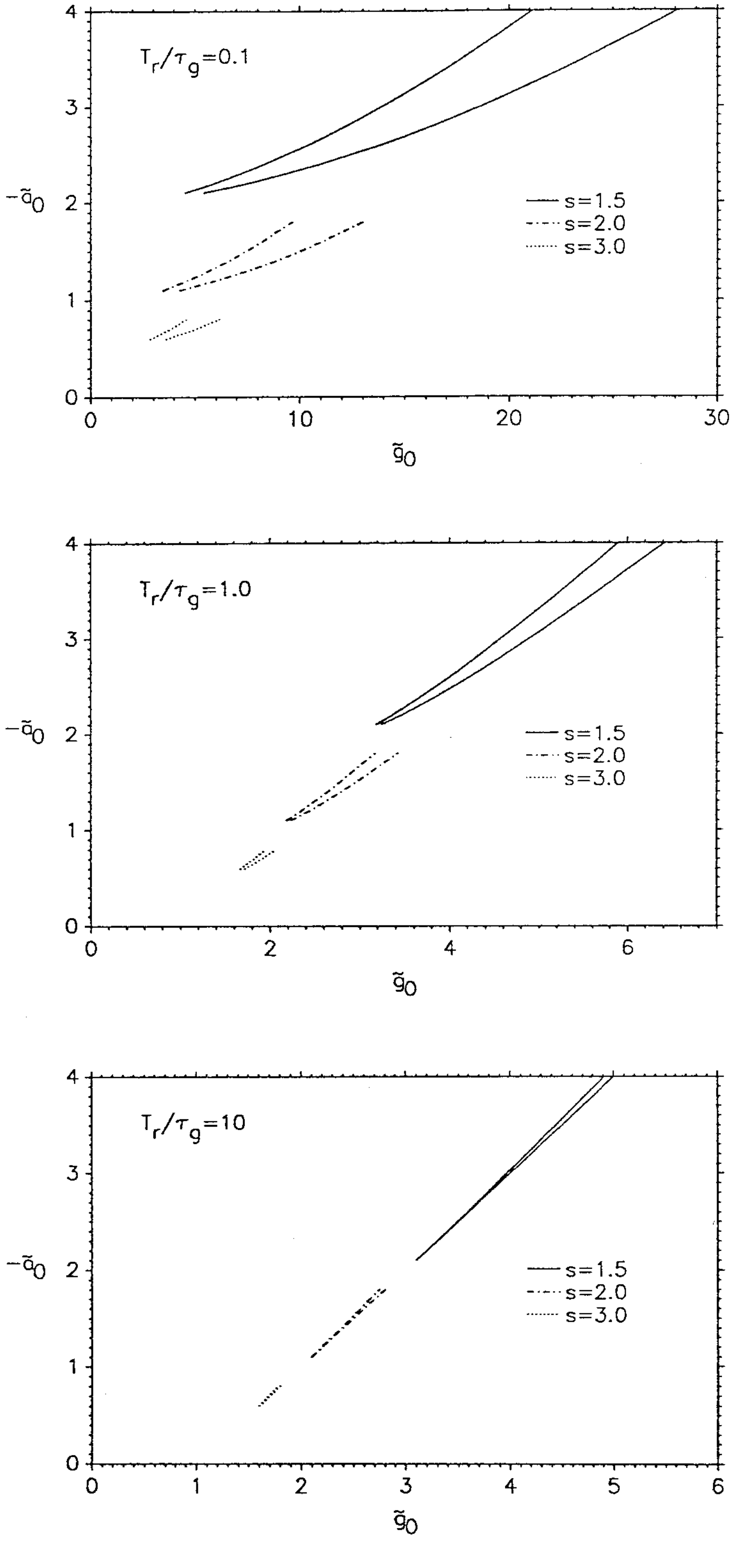

Figure 4.4: Ranges of unsaturated absorption and gain for passive mode-locking: only conditions where $U_0 < 0.5$ are shown; the ranges for s=2.0 and s=3.0 actually extend to all values of $\tilde{g}_0$ above the minimum values shown.

4.3 Harmonic passive mode-locking of an MQW laser coupled to an external cavity

Having demonstrated theoretically that quantum well lasers coupled to an external cavity should produce stable pulses at microwave repetition rates, experimental results on two-section multiple quantum well lasers coupled to external cavities are now presented. The experimental arrangement and observations are discussed, followed by an application of the small-signal saturation theory. A large-signal saturation model is then developed in the following section and used to predict stable mode-locking conditions and pulse energies.

While the results of section 4.2 showed that there is a maximum unsaturated gain level for stable passive mode-locking, only a single pulse circulating in the cavity was considered. When current injection levels are so high that the gain recovers above the loss level during one round-trip, multiple pulses may circulate in the cavity, so that the laser generates a pulse train at a harmonic of the fundamental cavity round-trip frequency. Since the time between pulses is then divided by the harmonic number, the gain recovers less, and net loss is again experienced by the leading edge of each pulse. The following experimental results demonstrate mode-locking at the first six harmonics of a 1.17 GHz cavity, with little dependence of the pulse energies and duration upon the repetition rate, as would be expected from the preceding analysis. Harmonic mode-locking can be beneficial in applications where variable repetition rate pulse trains are required, and may be a useful mechanism for high frequency mode-locking in long cavities, providing room to insert dispersion compensating and bandwidth controlling elements for pulsewidth reduction. Several authors have actively mode-locked semiconductor lasers at different harmonics by adjustment of the driving current frequency [3,4], but there has been very little previous work on harmonic passive mode-locking of semiconductor lasers, with the only reported results involving proton bombarded absorber sections to generate pulses in the tens of picoseconds at repetition rates up to 3.4 GHz, with no measurements of the pulse train power spectra [5].

The device used in this experiment is a buried-heterostructure quadruple quantum well laser whose optical cavity is electrically divided into two regions isolated by a dark resistance of 13 kΩ, one 60 μm long region acting as a saturable absorber, and another 400 μm long region providing gain. Electrical isolation is achieved by masking the zinc diffusion, which is used to increase the conductivity near the surface, between the two sections, along a 50 μm region that remains highly resistive. As illustrated in figure 4.5, the GaAs quantum wells are 75 Å wide, separated by 100 Å $Al_{0.2}Ga_{0.8}As$ barriers. The laser is coupled to the external cavity by a 40 times, 0.65 numerical aperture microscope objective, as shown in figure 4.1, and the cavity is terminated by a 70% reflecting mirror. The rear laser facet is adjacent to the absorber region and is coated to have 90% reflectivity; the front facet is anti-reflection coated to have less than 5% reflectivity. Both sections are driven by direct currents, and with the absorber unbiased, the device has a threshold current of 31 mA without feedback, and a turn-on threshold of 19 mA with feedback. The output from the end of the external

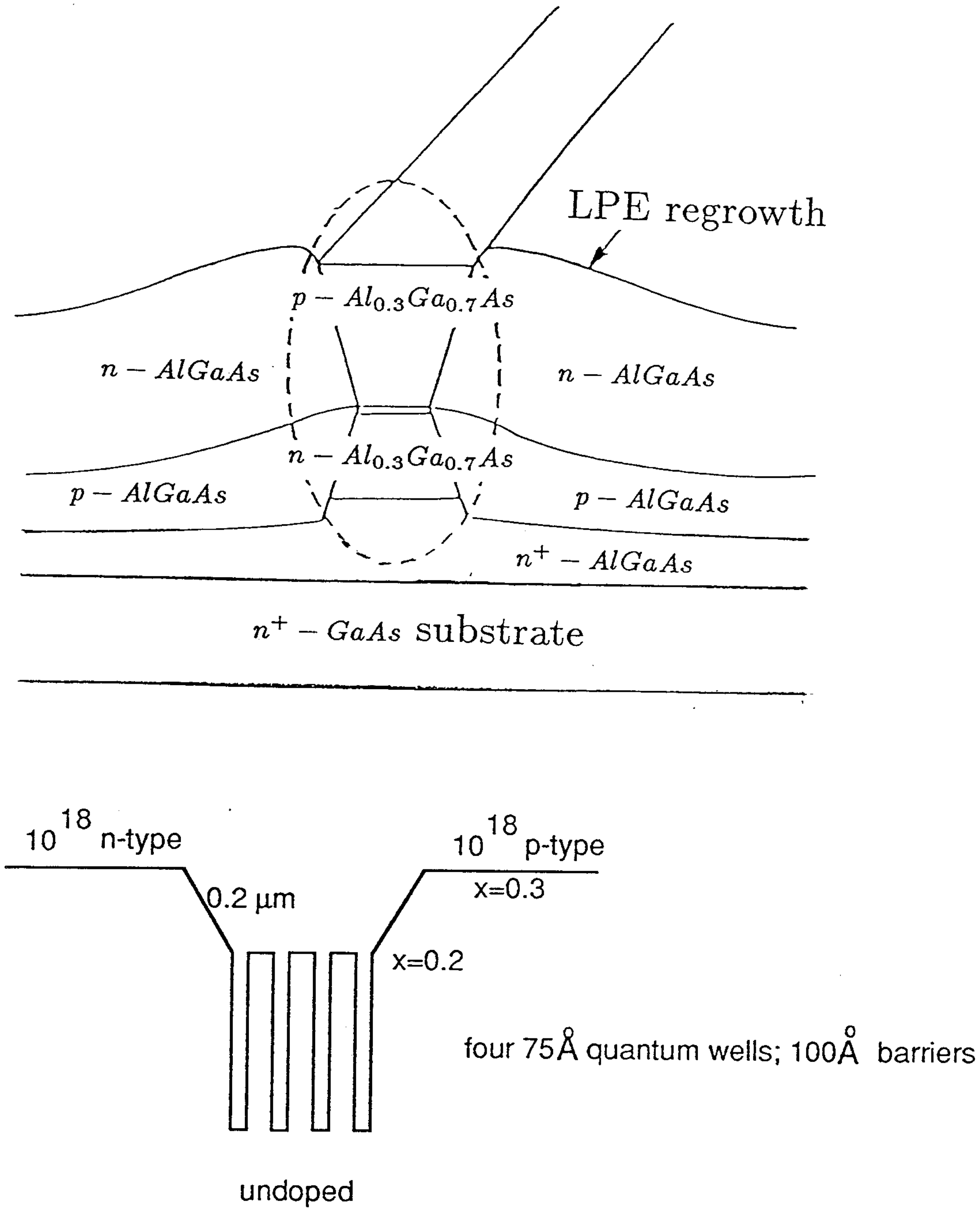

Figure 4.5: Structure of multiple quantum well buried heterostructure laser.

Harmonic	Current (mA)	pulsewidth (psec)	$\sigma_{\text{pulsewidth}}$ (psec)	N
1	34.9	8.1	0.9	5
2	45.1	8.5	1.0	5
3	53.1	8.8	0.6	5
4	65.1	9.0	2.2	9
5	68.5	8.5	1.1	7
6	66.0	8.6	1.3	9

Table 4.1: Pulse FWHM (averaged over N single shot measurements; $V_2 = 0.0$ V).

cavity is monitored by a photodiode with ~ 10 GHz bandwidth and the single-shot streak camera.

Streak traces of the first through sixth harmonic pulse trains are shown in figure 4.6, with their corresponding power spectra in figure 4.7. In each case, the absorber bias before the 100 ohm resistor shown in figure 4.1 is held fixed at 0.0 volts, and the gain current is adjusted so that the lower harmonics of the frequency spectra are suppressed below the spectrum analyzer noise floor, which is at least 40 dB below the frequency component corresponding to the pulse repetition rate. Higher resolution streak images display less than 10 psec average full-widths at half-maxima (FWHM), as shown in figure 4.8 and summarized in table 4.1, which is more than a factor of three shorter than observed from two-section bulk GaAs lasers [6].

The optical spectra have FWHM about twenty-five times greater than the minimum time-bandwidth limit, which may indicate pulse chiriping that can be compen-

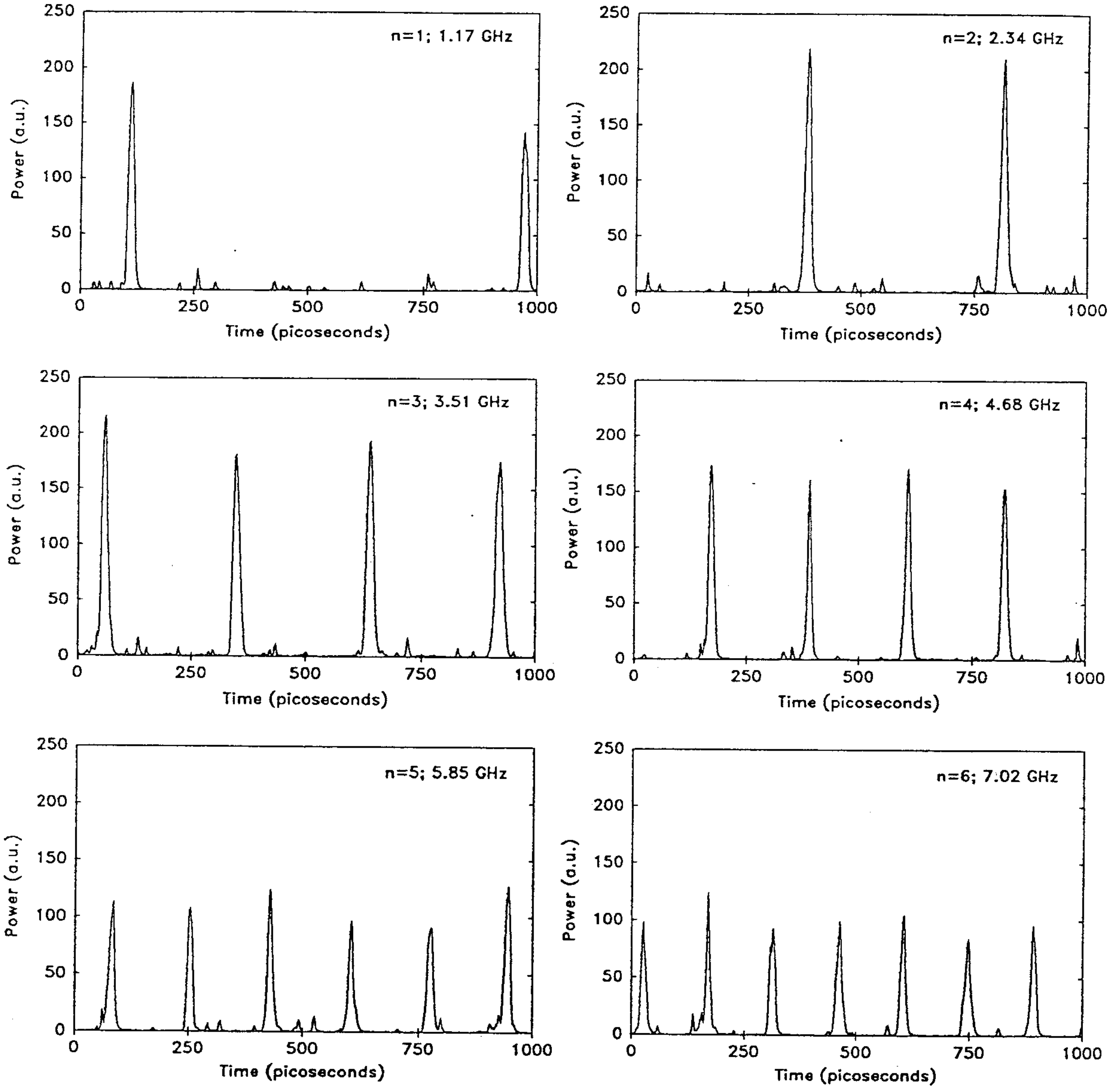

Figure 4.6: Single-shot streak camera traces of first through sixth harmonic passive mode-locking.

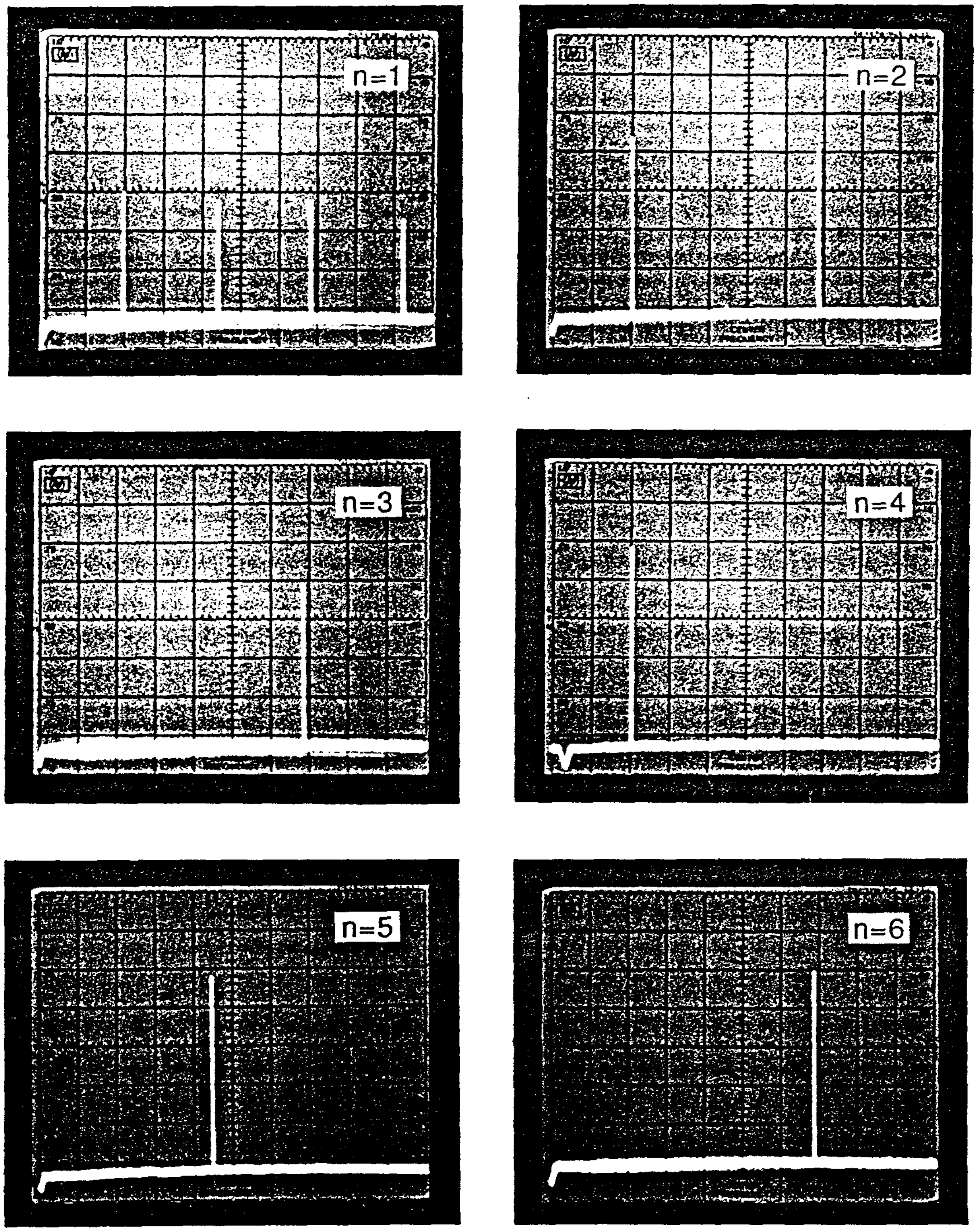

Figure 4.7: Photocurrent power spectra of harmonics 4, 5, 6, and 7 of 1.17 GHz fundamental for mode-locking at first through sixth harmonic repetition rates (10 dB/div; 3 MHz resolution, 3.8-8.5 GHz band).

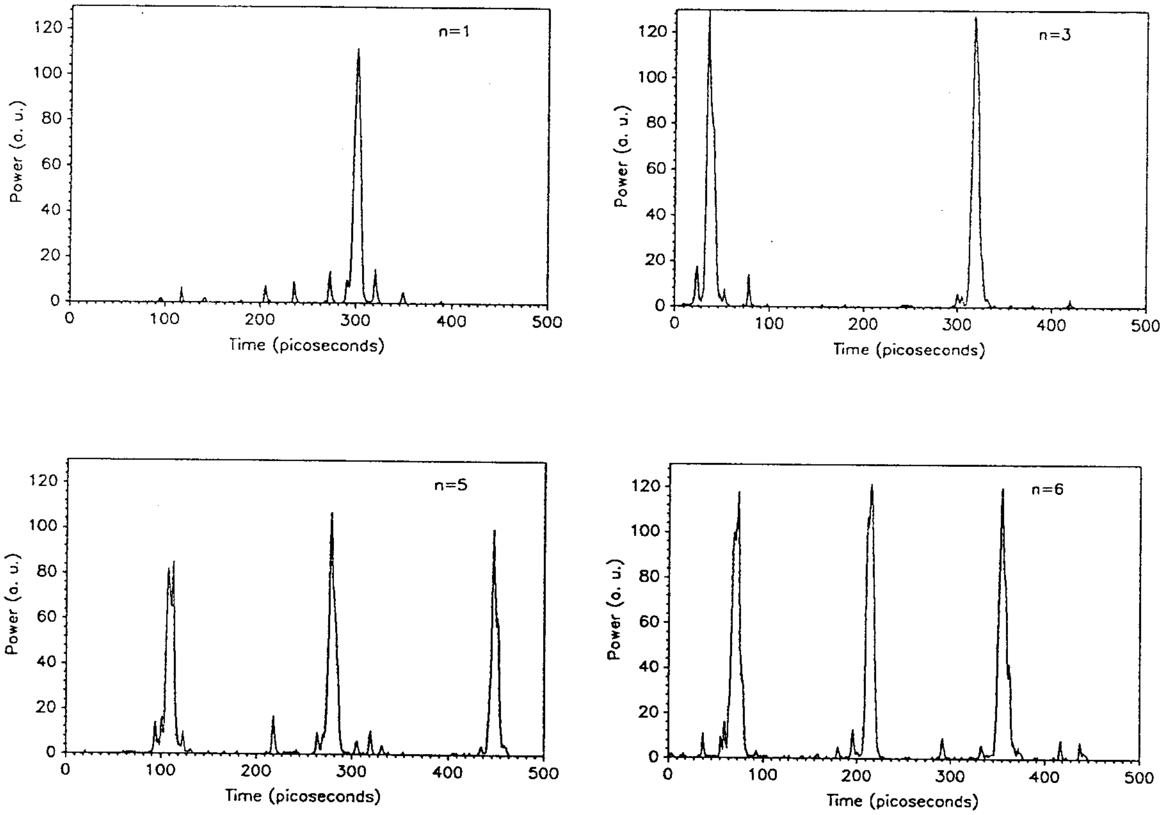

Figure 4.8: 6 ps resolution streak images at first, third, fifth, and sixth harmonic mode-locking.

sated by a grating pair [7,8] or the dispersion in an optical fiber [9], depending upon the sign of the chirp. If the excess bandwidth, however, is due to randomly phased modes, it can be reduced by inserting an etalon in the cavity [10]. More details about the spectra and pulsewidths of a similarly mode-locked laser are discussed in section 4.5.

The gain current levels, with the absorber voltage, V_2, fixed for the first through sixth harmonics are shown in figure 4.9. The output was observed simultaneously by the spectrum analyzer and streak camera, and no adjustments were made to the external cavity throughout these measurements. At threshold, the laser pulses at 1.17 GHz and continues to do so until either the current is reduced below 28mA, the turn-off threshold, or increased above 41 mA, where the repetition rate switches to 2.34 GHz. Second harmonic mode-locking is maintained until either the current is reduced to 33mA, where first harmonic mode-locking returns, or increased to 50 mA, where third harmonic mode-locking commences. This switching behavior with hysteresis is observed up to the sixth harmonic, after which the output is no longer a stable pulse train. Mode-locking occurs at up to five different harmonics for the same gain current, and the size of the hystersis loop increases with the harmonic number. Higher harmonics, up to the eighth, have been observed, but the conditions for their appearance are extremely sensitive to the feedback mirror adjustment.

The existence of stable multiple pulses in the laser cavity can be explained by considering how the recovery of the saturated gain is changed when the pulse repetition rate switches from one harmonic to another [14]. Following the theory from section

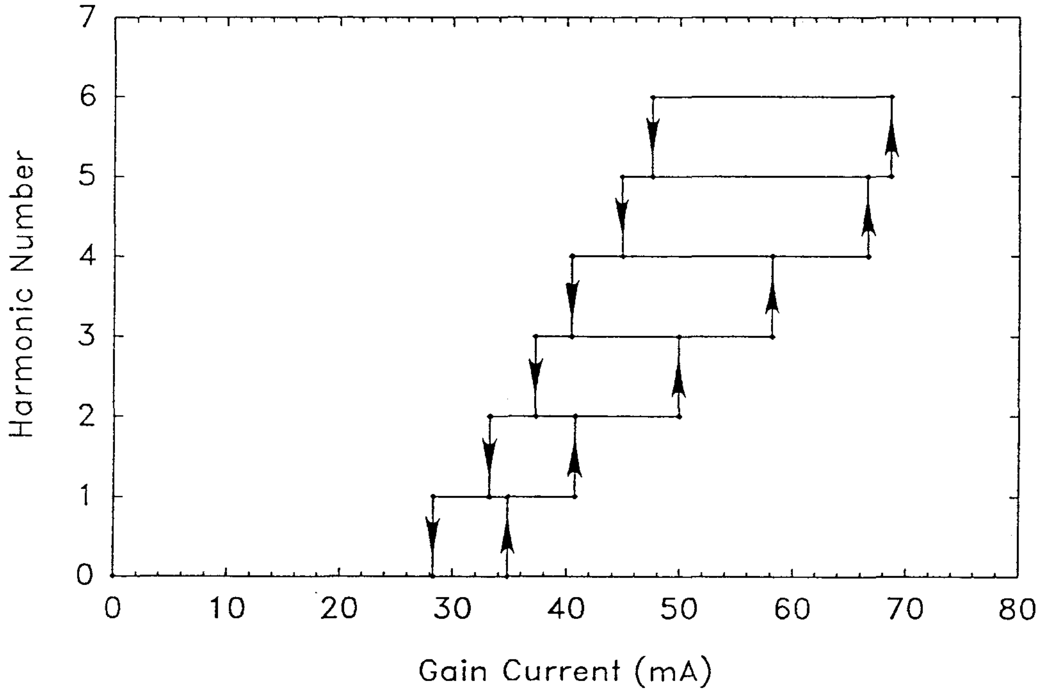

Figure 4.9: Measured repetition rate harmonic versus gain section current.

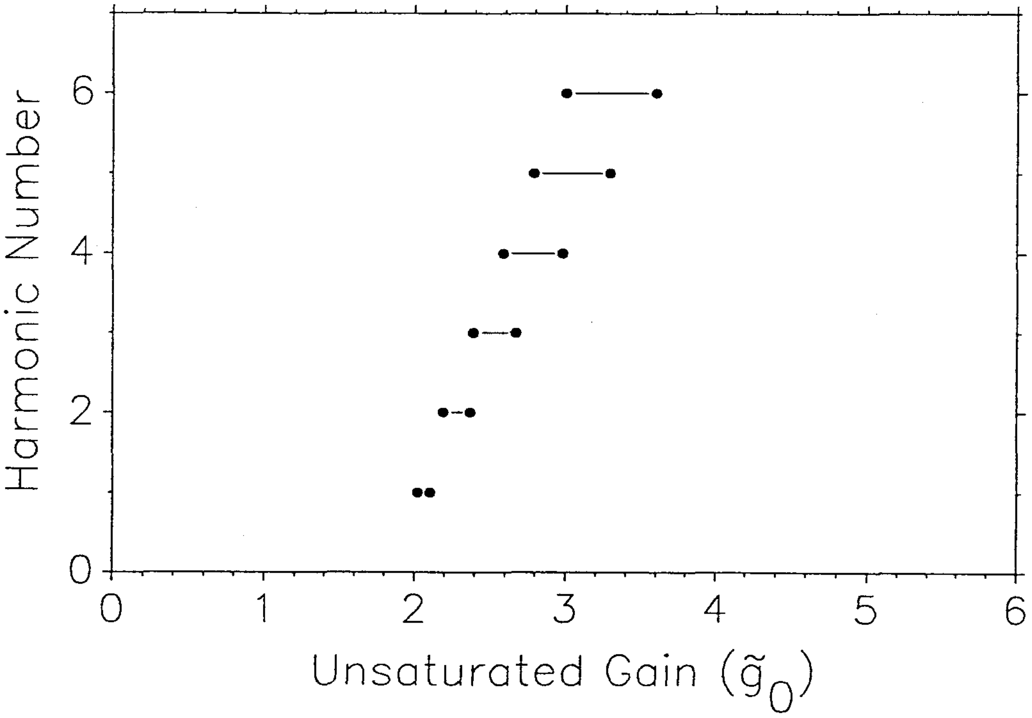

Figure 4.10: Ranges of mode-locking versus unsaturated gain using analytic theory of section 4.2; $\tilde{a}_0$ = -1.0; s = 3; T_r/τ_g = 2.0.

4.2, stability of the pulse requires that net loss be seen by its leading and trailing edges, or:

$$\tilde{g}_{i_{min}}(\tilde{a}_i, s) < \tilde{g}_i < 1 + \tilde{a}_i \tag{4.23}$$

where $\tilde{g}_{i_{min}}$ is the minimum gain required to have net loss after the pulse and depends on $\tilde{a}_i$, and on s. For a constant $\tilde{a}_i$, mode-locking occurs for a fixed range of $\tilde{g}_i$, but the allowed range of the unsaturated gain $\tilde{g}_o$ depends on the harmonic number. After being saturated by a pulse, the gain recovers exponentially with a time-constant τ_g, and the unsaturated gain is then related to the gain just before the pulse by:

$$g_o = g_i\left(\frac{e^{T_r/n\tau_g} - e^{-2U_0/s}}{e^{T_r/n\tau_g} - 1}\right) \tag{4.24}$$

where T_r is the cavity round-trip time; n = the number of pulses in the cavity, and $U_0 = AW(\infty)$, the product of the differential absorption and the pulse fluence.

Figure 4.10 shows the ranges of unsaturated gain where stable pulses can exist for the first six harmonics, using the parameter values shown, and where complete recovery of the absorber between pulses has been assumed. After the laser becomes unstable for mode-locking at a given repetition rate, mode-locking can occur at the next higher harmonic. Upon reduction of unsaturated gain, however, there can be hysteresis before switching back to the lower harmonic. Disturbances between the pulses, which are necessary to redistribute the energy in the cavity and change the harmonic number, are suppressed, since they see net loss in a round-trip until the gain is reduced to where the pulse energy becomes too small to saturate the gain enough for a pulse's trailing edge to see net round-trip loss. In addition, the size of the locking ranges increase with harmonic number, consistent with our observations and with those from reference [5]. The mode-locking ranges using a more accurate numerical model, to be presented in the next section, are shown in figure 4.14.

4.4 Large signal saturation model for passive mode-locking

The model for passive mode-locking presented in section 4.2 was based on assumptions of small cavity losses and small single-pass gain and loss, such that all exponentials could be expanded to first or second order, and the order in which the pulse encountered the various elements of the laser cavity could be commuted. While this model is useful for finding approximate conditions to guide the development of mode-locked laser systems and for demonstrating how passive mode-locking is achieved with a slow saturable absorber, the small-signal expansions greatly underestimate the saturation in semiconductor lasers. We now develop a model more suitable for the semiconductor laser coupled to an external cavity, from which mode-locking conditions and pulse energies will be found.

4.4.1 Large-signal saturation equations

It is first necessary to develop a more accurate model to describe the saturation when the pulse energy undergoes large changes as it propagates through the gain and absorber media. While the solutions for an arbitrary pulse shape propagating through a two-level system can be found [11], for our purposes we need only determine the changes in inversion and fluence due to the passage of the entire pulse. A simple statistical model developed by Frigo [12] is used to determine the stimulated changes in carrier density and pulse fluence given an initial inversion and an initial pulse fluence. It is assumed that the pulse duration is much longer than the ~ 100 femtosecond intraband relaxation times, as discussed in Chapter 2, and much shorter than the ~ 100 ps to nanosecond gain and absorber recovery times. The <10 ps pulsewidths measured in the experiments of section 4.3 show that this second condition is satisfied. As a pulse travels along the x-direction, the stimulated transition rate is

$$\frac{dn_g}{dt} = -G(n_g - n_{g0})S(x)\frac{c}{\mu_g} \tag{4.25}$$

where $S(x)$ is the photon density at x, from which the probability that a given carrier at depth x will be stimulated by a single photon in the pulse is:

$$\frac{dn_g}{(n_g - n_{g0})} = -\frac{G\Gamma}{\Theta} \tag{4.26}$$

where Γ is the optical confinement factor, and Θ is the cross-sectional area of the active region. The probability that a given carrier will be stimulated by any photon in the pulse is then

$$P(x) = 1 - (1 - \frac{G\Gamma}{\Theta})^N \tag{4.27}$$

where N is the total number of photons in the pulse. Using typical values for differential gain and the cross-secitional area of the beam, $P(x)$ is approximated by:

$$P(x) = 1 - e^{-j(x)} \tag{4.28}$$

where the normalized fluence $j(x)$ is:

$$j(x) \equiv \frac{GN\Gamma}{\Theta}. \tag{4.29}$$

The change in photon number in the pulse is given by:

$$\frac{dN}{dx} = [n_g(x) - n_{g0}]\Theta P(x) \tag{4.30}$$

and using the gain exponent as a function of distance in the active medium:

$$\int_0^x g(x')dx' = \int_0^x [n_g(x') - n_{g0}]G\Gamma dx' \tag{4.31}$$

we get the integral:

$$\int_{x=0}^{x=L} \frac{dj}{1 - e^{-j(x)}} = \int_0^L g(x)dx \equiv g_i \tag{4.32}$$

which relates the initial fluence and final fluence to the initial optical thickness,g_i. Performing the integration yields the ultra-short pulse (USP) saturation equation:

$$\frac{e^{j_f} - 1}{e^{j_i} - 1} = e^{g_i} \tag{4.33}$$

which accounts for the growth of the pulse as it propagates through the saturable medium. In addition, the conservation relation:

$$j_i + g_i = j_f + g_f \tag{4.34}$$

can be derived, relating the change in optical thickness to the change in normalized pulse fluence.

4.4.2 Steady-state mode-locking conditions

Referring to figure 4.11, the USP saturation equation can be used to find the steady-state pulse energy and the steady-state saturation behavior of the gain and absorber. Convergence of a steady-state solution, however, is not guaranteed, since unstable solutions, where the cavity energy oscillates as in the case of self-sustained pulsation, can also occur. As before, the recovery of the gain and absorption follow:

$$g_i = (g_0 - g_f')(1 - e^{-\frac{T_r}{\tau_g}}) + g_f' \tag{4.35}$$

where g_f' is the gain exponent after the second passage of the pulse.

The steady-state operating conditions are found by starting with a value for j_1 and determing j_5 with the USP saturation and conservation equations. For example, as $R_2 j_1$ passes through the gain region, which has an initial gain g_i,

$$j_2 = s \ln[e^{g_i}(e^{R_2 j_1/s} - 1) + 1] \tag{4.36}$$

and

$$g_f = g_i + \frac{1}{s}(R_2 j_1 - j_2) \tag{4.37}$$

After propagating through all regions to find j_5, j_1 is set equal to j_5 and the calculation is continued until

$$|j_1 - j_5| < 10^{-7}. \tag{4.38}$$

Having determined the pulse energy at different points in the cavity and the gain and absorption saturation, the conditions for stability from section 4.2 can be invoked.

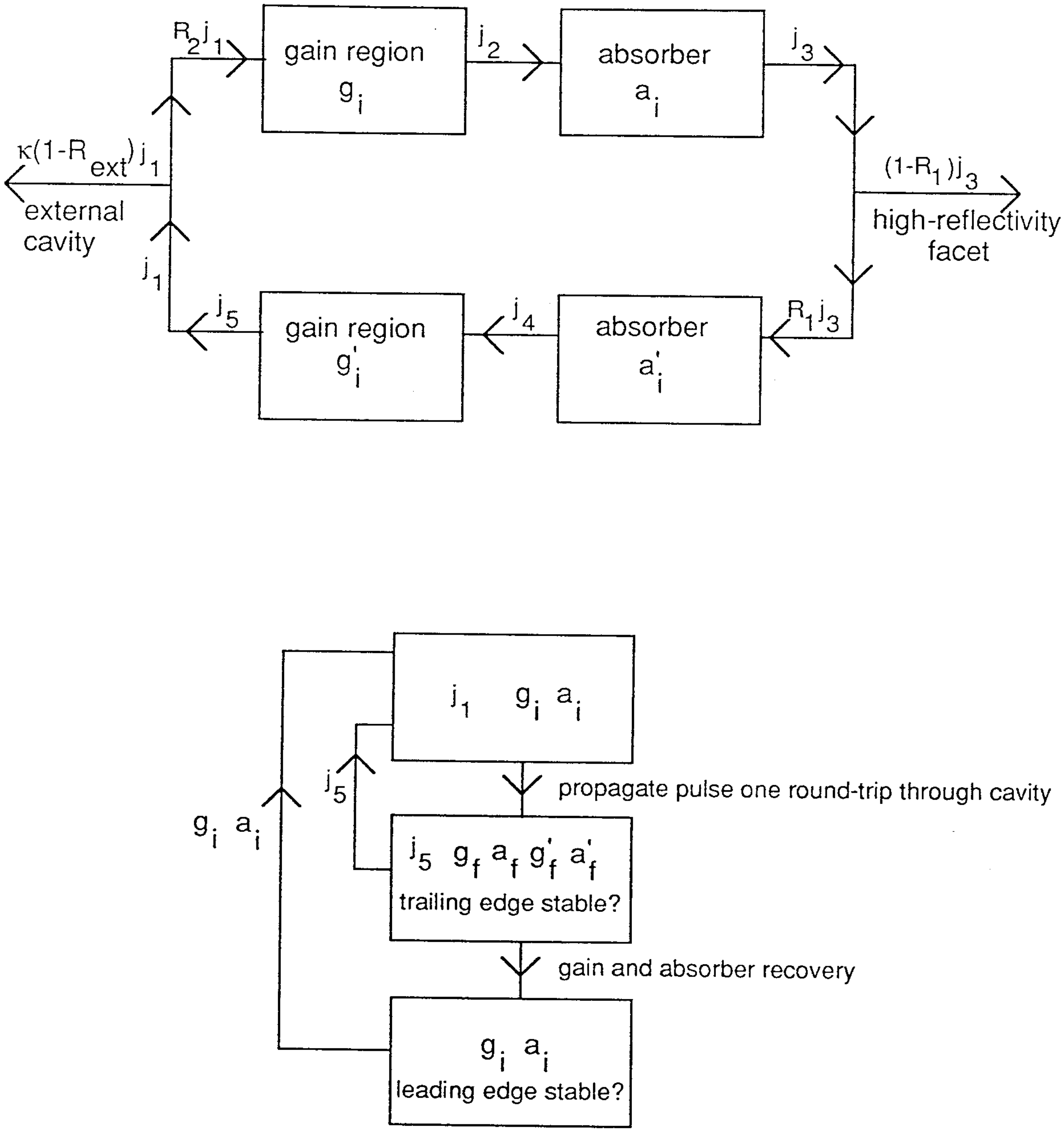

Figure 4.11: Determination of mode-locking conditions and pulse energy using the ultra-short pulse (USP) saturation equation.

Net small signal loss for the leading edge of the pulse requires:

$$2(\tilde{g}_i + \tilde{a}_i) - 1 < 0 \tag{4.39}$$

and net small signal loss for the trailing edge requires:

$$\tilde{g}_f + \tilde{g}'_f + \tilde{a}_f + \tilde{a}'_f - 1 < 0. \tag{4.40}$$

The output fluence from the external cavity end mirror is:

$$\frac{\kappa(1 - R_{ext})j_1}{\Gamma} \tag{4.41}$$

where κ is the coupling efficiency from the front facet through the microscope objective, and the fluence coupled back into the laser is $R_2 j_1$. R_2 can be estimated from the change in laser threshold or external differential quantum efficiency; however, the uncertainty in the reflectivity of the A.R. coated facet makes the estimate very rough, and an approximate value of 10% is used in the calculations.

While the pulse may form a standing wave in the absorber (since its spatial extent is about 10 times the absorber length), the coherence time of the pulse is only about half the absorber length, so this effect is neglected here. It can be partially accounted for by increasing s, since the interference results in more saturation of the absorption for a given pulse fluence compared to the incoherent double passage of the pulse [13].

For a given g_i and a_i, the pulse energy can be found directly by solving the transcendental equation:

$$x_1 = \{\frac{g_1 x_1^{R_2/s}}{g_1(x_1^{R_2/s} - 1) + 1}\{\{\frac{a_1[g_1(x_1^{R_2/s} - 1) + 1]^s}{a_1\{[g_1(x_1^{R_2/s} - 1) + 1]^s - 1\} + 1} \\ \{\{a_1\{[g_1(x_1^{R_2/s} - 1) + 1]^s - 1\} + 1\}^{R_1} - 1\} + 1\}^{1/s} - 1\} + 1\}^s \tag{4.42}$$

where $x_1 = e^{j_1}$; $g_1 = e^{g_i}$ and $a_1 = e^{a_i}$. The graph in figure 4.12 shows the three solutions, one at zero energy, one unstable solution, and the highest power, stable solution. To ensure that the high power solution is reached, rather than the zero power solution, the simulation is started with a normalized fluence of 10. In actual experiments, hysteresis is observed in the laser threshold due to the saturation of the absorption, as would be expected from the two stable solutions in figure 4.12.

4.4.3 Mode-locking conditions for semiconductor laser: harmonic behavior and pulse energies

Employing the model just described, we calculate the locking ranges as a function of $\frac{T_r}{\tau_g}$ for various values of s, as shown in figure 4.13. The single-pass unsaturated gain and absorption levels are normalized to $\frac{T_r}{2\tau_p}$, as in equation 4.6, neglecting the internal losses in the semiconductor laser. To determine the locking ranges for different harmonics directly from this figure, the ratio $\frac{T_r}{\tau_g}$ is divided by the number of pulses in the cavity. The higher harmonics become stable as the unsaturated gain increases, and more than one harmonic may be stable for the same gain level. The locking ranges for the first six harmonics are calculated in figure 4.14, for comparison with the results using the small-signal model. Finite absorber recovery times are considered showing the narrowing of the locking ranges as the upper limit of unsaturated gain is reduced to maintain inequality 4.39, as the recovery becomes slower.

In addition to finding conditions for passive mode-locking, this large signal model

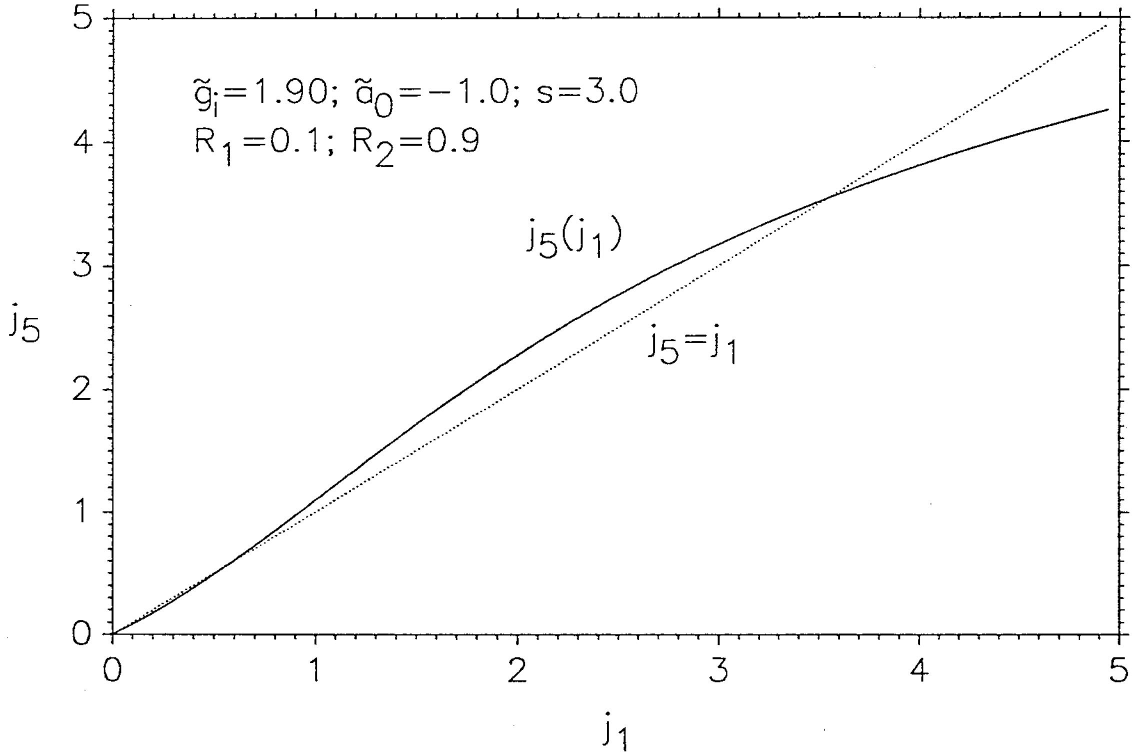

Figure 4.12: Graphical solutions for pulse fluence; stable solutions exist at zero power and high power, while the middle solution is unstable.

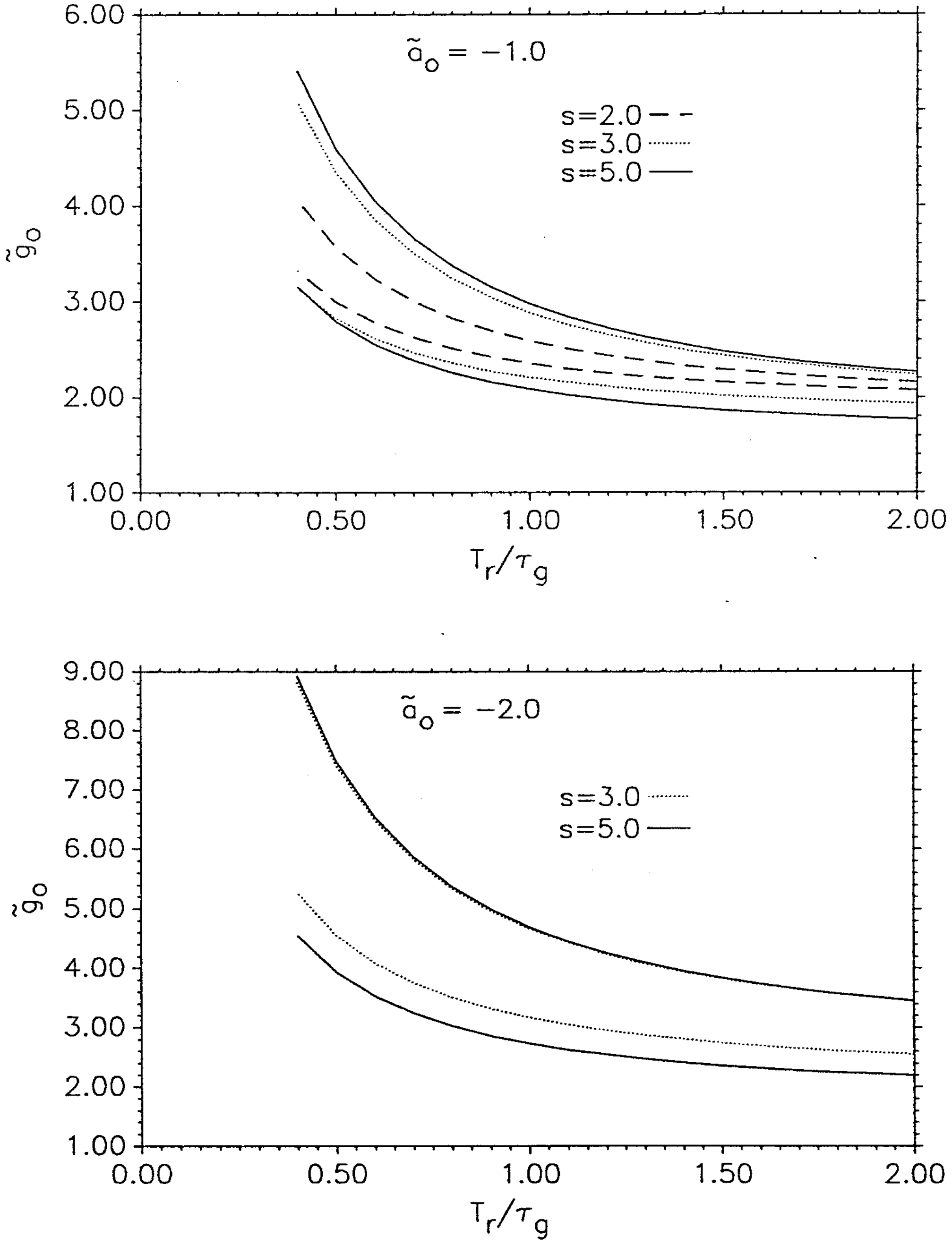

Figure 4.13: Mode-locking ranges using large-signal saturation model.

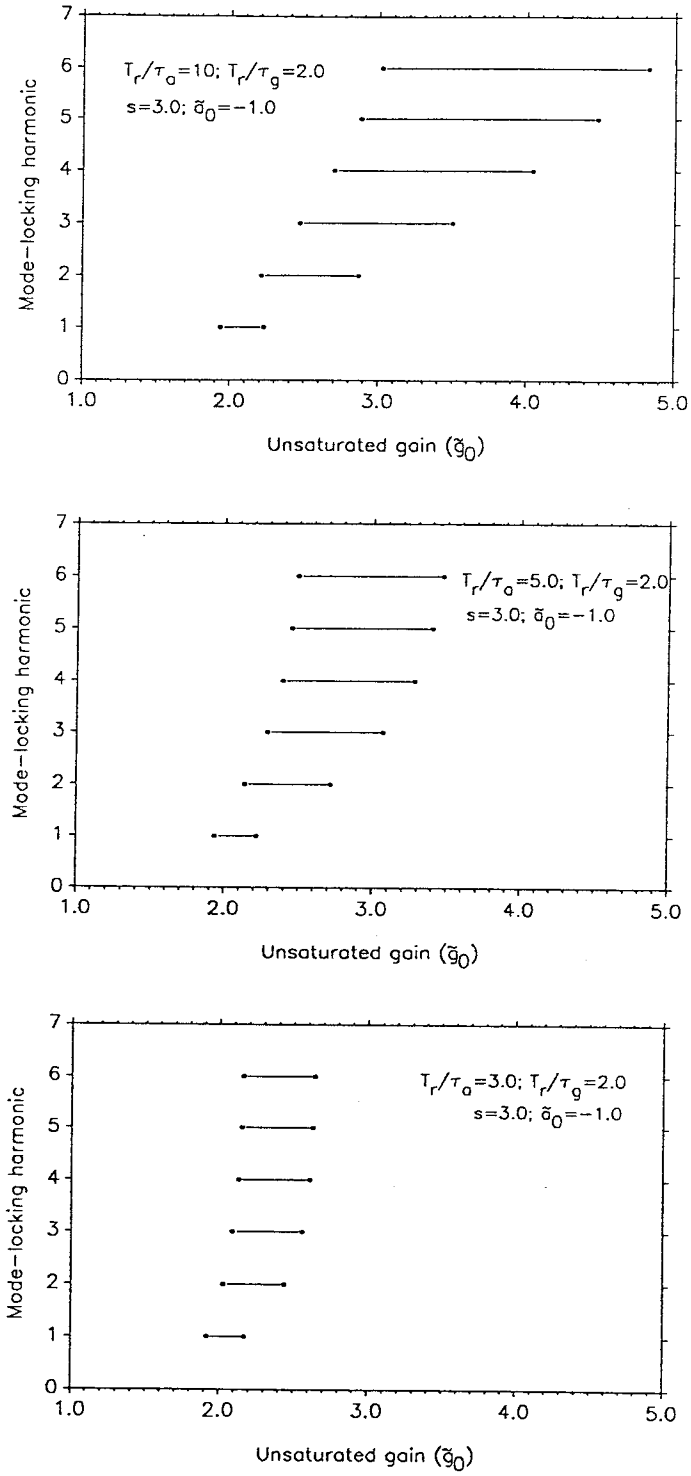

Figure 4.14: Locking ranges of different harmonics for (a) $T_r/\tau_a = 10$; (b) $T_r/\tau_a = 5$; (c) $T_r/\tau_a = 3$.

determines pulse energies. Calculated internal pulse fluences, j_1, are shown in figure 4.15, using the material parameters shown, for different values of s. The average power for two mode-locked quantum well lasers at several harmonics is shown in figure 4.16 and are in reasonable agreement with the calculated values. The approximate normalized pulse fluence in these lasers for 1 mW of output power at 529 MHz is 3.6, using $A = 10^{-15} cm^2$, $l_x = 0.3\mu$m, $l_y = 3\mu$m, $\lambda_0 = 8500$ Å, and $\kappa(1 - R_{ext}) = 0.25$. The total measured average power consists of a noise background and the power in the pulses. The average power increases approximately the same amount from the upper limit of one harmonic locking range to the next, consistent with the two models in this chapter that predict independence of the pulse energy on the harmonic number when the absorber recovers completely between pulses. The data in figure 4.25, near the end of this chapter, show that the absorber has a recovery time of less than 150 ps.

The pulse energy is restricted to a narrow range by the geometric and material conditions and does not change very much with increased gain current. The limitation on pulse energy is one of the most severe problems with mode-locked semiconductor lasers, but some increases in pulse energy should be possible by increasing the absorption using a larger number of quantum wells or longer absorbing region, as shown in figure 4.16, and by optimizing the structure for maximum width and minimum confinement of the optical mode in the active region. In other words, since the fluence of the pulse cannot be changed much, the area of the optical mode needs to be increased. However, the drawbacks to increasing the power by these methods include

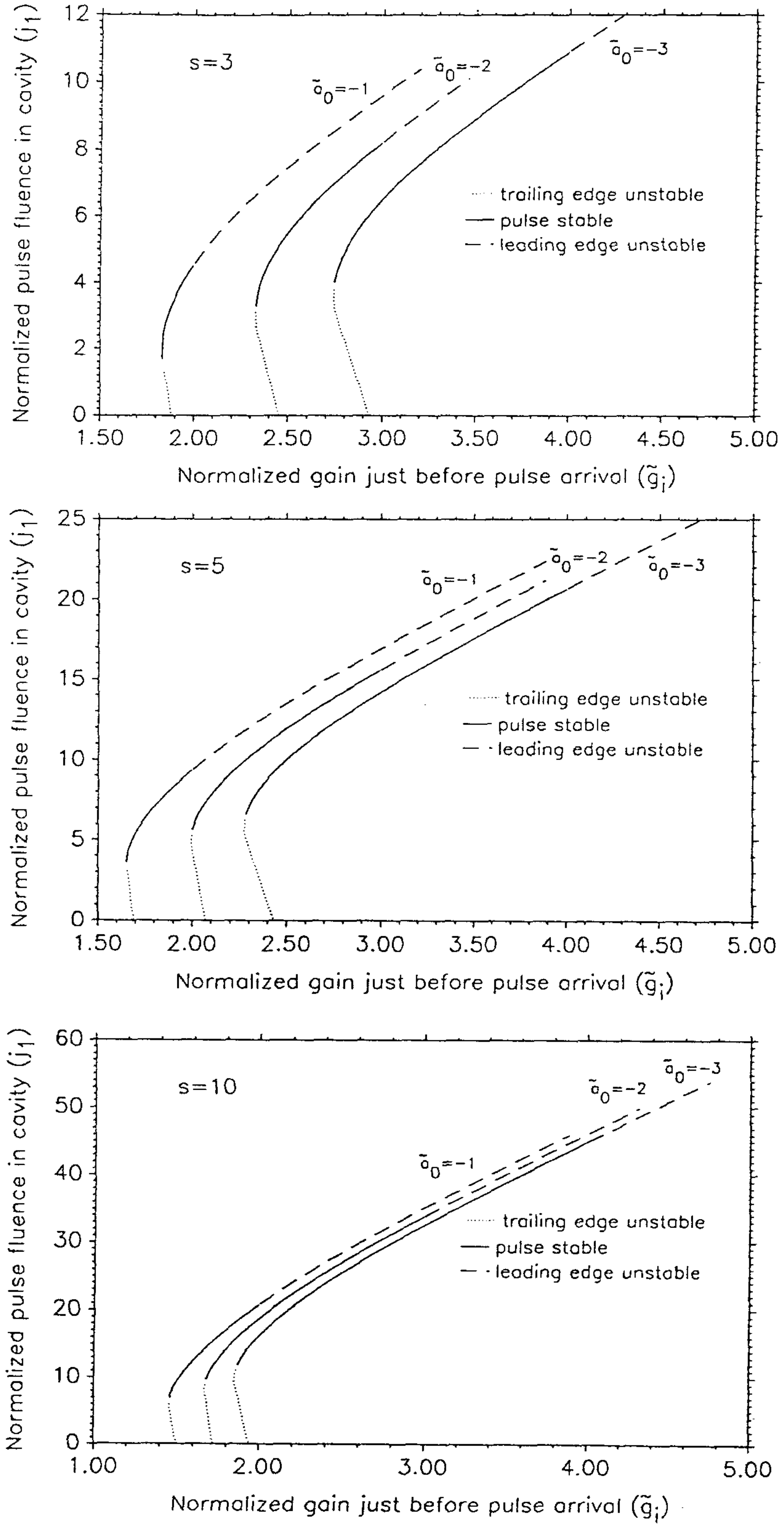

Figure 4.15: Calculated pulse fluence for different values of s and $\tilde{a}_0$.

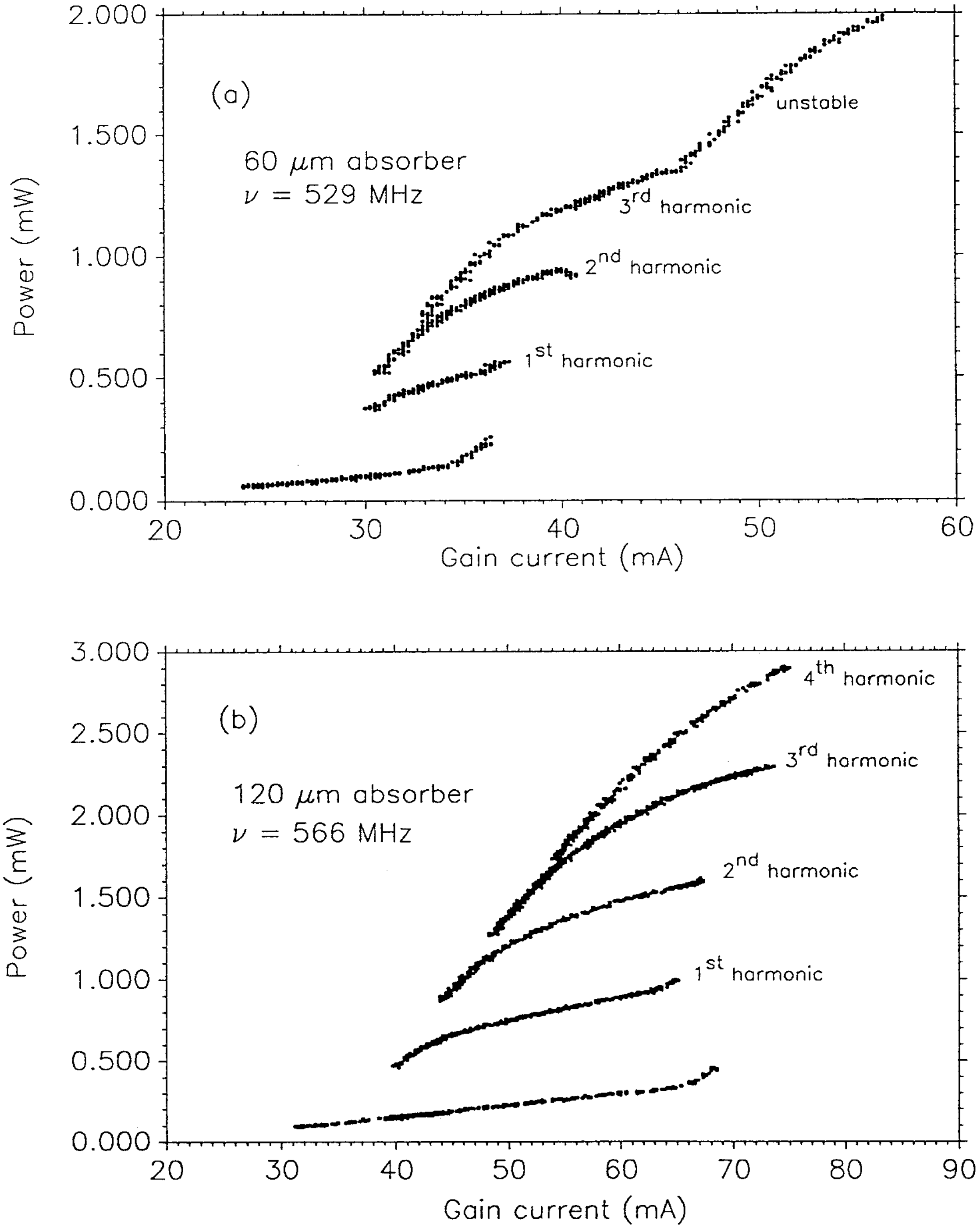

Figure 4.16: Average power from passively mode-locked lasers with absorbers grounded and (a) $l_a = 60\ \mu$m; (b) $l_a = 120\ \mu$m; the laser with the longer absorber can generate higher energy pulses.

increased operating current and possible broadening of the pulse if a longer absorbing region is used.

The model just described is more suitable than the model of section 4.2 for the large losses and large saturation in typical mode-locked semiconductor lasers. Further refinements could include additional non-linearity of gain as a function of carrier density and the dependence of carrier lifetime on carrier density. A complete model of external cavity passively mode-locked semiconductor lasers to predict pulse widths would need to consider the dynamics and shape of the gain and absorption spectra as a function of carrier density, the dependence of refractive index and gain spectra on carrier density, very fast gain absorption transients that occur on picosecond time scales, and the spatial variation of all parameters, including the pulse shape.

4.5 Pulse train stability

A mode-locked pulse train will always have some fluctuations in the pulse repetition rate and in the pulse energies. These fluctuations appear as noise bands in the power spectrum of the intensity, and it is shown how a photodetector and spectrum analyzer with bandwidth one order of magnitude higher than the pulse repetition rate can be used to characterize the root-mean-square (RMS) fluctuations of pulse separation (timing jitter) and pulse energy. The pulse train's power spectrum consists of strong signals at harmonics of the pulse repetition rate, with weak noise sidebands from which the jitter can be determined.

For measurements using ultrafast lasers where synchronization between several lasers or between the laser and an external signal are required, time resolution is severely degraded by large timing jitters. It has been shown that the timing jitter in actively mode-locked semiconductor lasers driven by high purity synthesizers is much smaller than in conventional lasers [16], but there have been no previous measurements of the timing jitter in passively mode-locked semiconductor lasers. The two-section multiple quantum well laser mode-locked in an external cavity operates under the proper saturation conditions to achieve high stability, as will be experimentally demonstrated in the following measurements.

4.5.1 Theory of phase and amplitude jitter measurements

Before deriving the relationships between the noise power spectra and the timing and energy fluctuations, a very simple model illustrated in figure 4.17 describes how timing jitter and amplitude jitter can be separated on the basis of the dependence of the noise power on the carrier harmonic. Considering a train of identical pulses with RMS timing jitter ΔT_r, the spectral decomposition of the train shows that the RMS phase jitter of the first order harmonic is $\frac{2\pi\Delta T_r}{T_r}$, while the jitter of harmonic order n is $\frac{2\pi n\Delta T_r}{T_r}$. The power spectral density then increases as n^2 for phase noise, while the amplitude noise is the same for all harmonic orders.

Following the treatment of reference [15], it will be shown how the RMS timing jitter and pulse energy fluctuations can be related to the power spectrum of the pulse

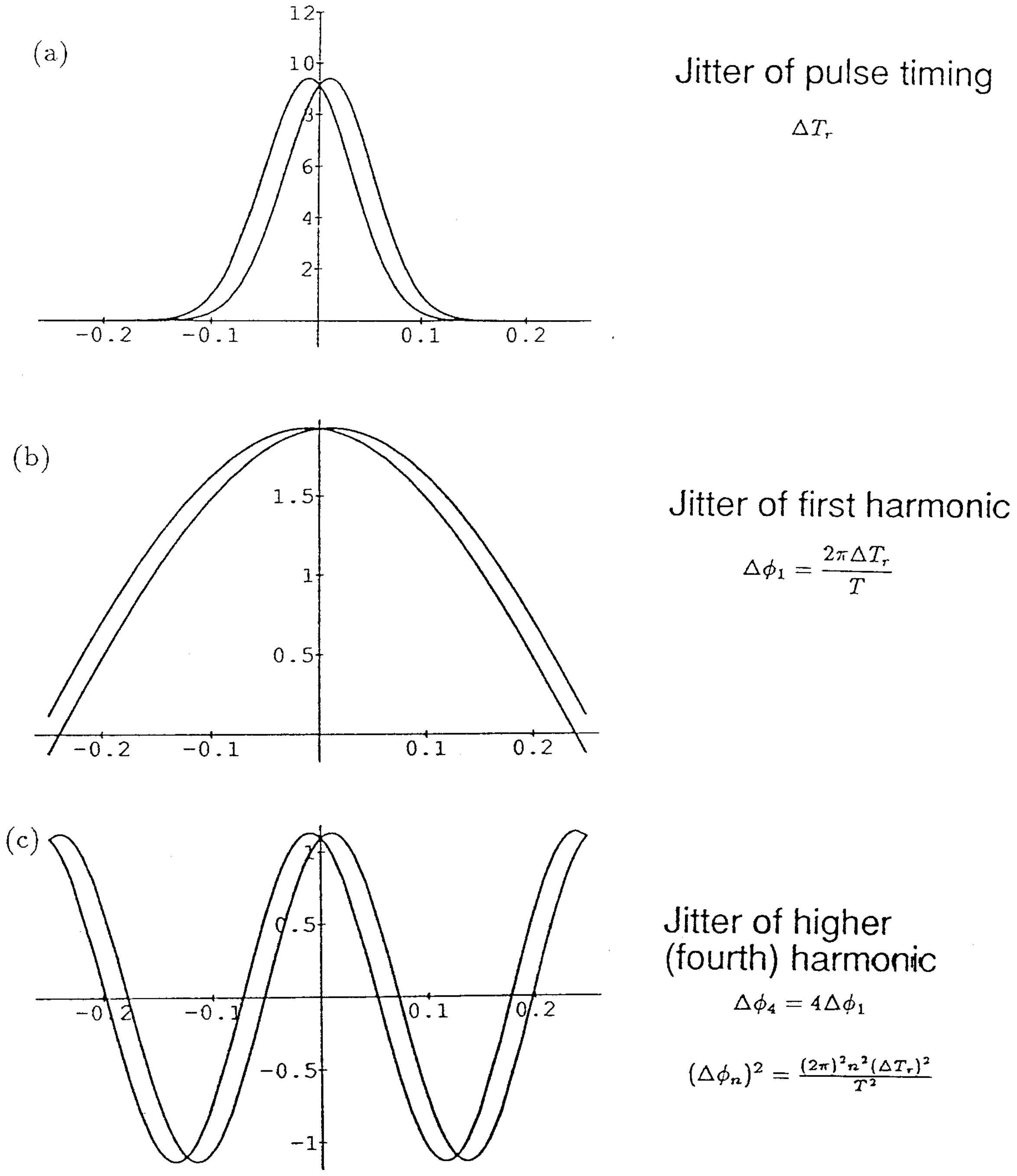

Jitter of pulse timing

ΔT_r

Jitter of first harmonic

$$\Delta\phi_1 = \frac{2\pi\Delta T_r}{T}$$

Jitter of higher (fourth) harmonic

$$\Delta\phi_4 = 4\Delta\phi_1$$

$$(\Delta\phi_n)^2 = \frac{(2\pi)^2 n^2 (\Delta T_r)^2}{T^2}$$

Figure 4.17: Determination of pulse train timing jitter from power spectra: (a) pulse train with RMS jitter ΔT_r; (b) first order harmonic; (c) fourth order harmonic; phase noise power increases as n^2.

train. A perfect pulse train can be represented by:

$$F_0(t) = \sum_{n=-\infty}^{\infty} f(t+nT) \tag{4.43}$$

where $f(t)$ is the intensity of a single pulse and T is the time between pulses. The pulse train with timing and energy fluctuations can be represented by:

$$F(t) = \sum_{n=-\infty}^{\infty} f(t+nT+\delta T_n)[1+A(t)] \tag{4.44}$$

where $A(t)$ is a random variable representing the energy fluctuations, and δT_n is the time shift of pulse n. Under the assumption that the RMS timing jitter is much smaller than the spacing between pulses, the noisy pulse train can be related to the perfect pulse train by a first order Taylor expansion:

$$\begin{aligned} F(t) &\doteq \sum_{n=-\infty}^{\infty} [f(t+nT) + \dot{f}(t+nT)|_{(t+nT)}\delta T_n][1+A(t)] && (4.45) \\ &= F_0(t)[1+A(t)] + \dot{F}_0(t)TJ(t) && (4.46) \end{aligned}$$

where $TJ(t) = \delta T_n$ and the product of $A(t)\dot{F}_0(t)TJ(t)$ has been neglected.

The power spectral density can be calculated from the autocorrelation of $F_0(t)$ using the Wiener-Khintchine theorem:

$$P_F(\omega) = \frac{1}{2\pi}\int_{-\infty}^{\infty} G_F(\tau)e^{i\omega\tau}dt \tag{4.47}$$

where the autocorrelation $G_F(\tau)$ is given by:

$$G_F(\tau) = \int_{-\infty}^{\infty} F(t+\tau)F(t)dt. \tag{4.48}$$

The pulse train has been assumed to be ergodic, so that the ensemble average can be replaced by a time average. The autocorrelation $G_F(\tau)$ is

$$G_F(\tau) = G_{F_0}(\tau)[1+G_A(\tau)] + T^2 G_{\dot{F}_0}(\tau)G_J(\tau) \tag{4.49}$$

where the statistical independence of $A(t)$ and $J(t)$ makes all terms involving their product zero. Fourier transforming the autocorrelation gives the power spectral density:

$$P_F(\omega) = P_{F_0} * [\delta(\omega) + P_A(\omega)] + [(\omega T)^2 P_{F_0}(\omega)] * P_J(\omega). \tag{4.50}$$

To derive this power spectrum, the relationship

$$P_{\dot{F}_0} = \omega^2 P_{F_0}, \tag{4.51}$$

has been obtained from the Fourier transfom of $f(t)$.

The power spectral density of the noiseless pulse train is derived directly from the Fourier transform of $F_0(t)$.

$$\begin{aligned} \tilde{F}_0(\omega) &= \frac{1}{\sqrt{2\pi}} \int_{-\infty}^{\infty} \sum_{n=-\infty}^{\infty} f(t+nT) e^{i\omega t} dt && (4.52) \\ &= \sum_{n=-\infty}^{\infty} e^{-in\omega T} \tilde{f}(\omega) && (4.53) \\ &= \frac{2\pi}{T} \tilde{f}(\omega) \sum_{n=-\infty}^{\infty} \delta(\omega - \frac{2\pi n}{T}) && (4.54) \end{aligned}$$

giving

$$P_{F_0}(\omega) = (\frac{2\pi}{T})^2 |\tilde{f}(\omega)|^2 \sum_{n=-\infty}^{\infty} \delta(\omega - \frac{2\pi n}{T}). \tag{4.55}$$

Finally, the power spectral density of the noisy pulse train is:

$$P_F(\omega) = (\frac{2\pi}{T})^2 |\tilde{f}(\omega)|^2 \sum_{n=-\infty}^{\infty} [\delta(\omega_n) + P_A(\omega_n) + (2\pi n)^2 P_J(\omega_n)] \tag{4.56}$$

where $\omega_n = \omega - \frac{2\pi n}{T}$, and the variation of $|\tilde{f}(\omega)|^2$ over the width of the noise bands is neglected. When the finite bandwidth of the detector is considered, the measured power spectrum is:

$$P_M(\omega) = 2\pi |\tilde{g}(\omega)|^2 P_F(\omega) \tag{4.57}$$

where $\tilde{g}(\omega)$ is the transfer function of the detector.

The measured power spectrum, illustrated in figure 4.18 on a logarithmic scale, consists of a set of sharp peaks at harmonics of the pulse repetition frequency with sidebands of amplitude noise, which is independent of the harmonic order, and phase noise power that rises quadratically with the harmonic. The finite response time of the detector gives an envelope to the harmonics that decreases at higher frequencies. The RMS pulse energy fluctuations and phase jitter can be found from the total integrated power in the noise spectra about a carrier harmonic.

$$\begin{aligned} \sqrt{< \Delta E(t) >^2} &= F_0(t)\sqrt{< [1 + A(t)]^2 - 1 >} && (4.58) \\ &= F_0(t)\sqrt{< A(t)^2 >} && (4.59) \end{aligned}$$

and the RMS fractional pulse energy fluctuation, assumed much smaller than unity, is

$$\frac{\Delta E}{E} = \sqrt{\int_{-\infty}^{\infty} P_A(\omega) d\omega} \qquad (4.60)$$

using Parseval's theorem. The phase noise can be identified from its quadratic dependence on harmonic, and the RMS timing jitter can then be found from:

$$\frac{\Delta T}{T} = \sqrt{\int_{-\infty}^{\infty} P_J(\omega) d\omega}. \qquad (4.61)$$

The ratio of the measured power density due to the phase noise about the nth harmonic carrier to the carrier power is

$$L_P(f) = (2\pi n)^2 P_J(f) \qquad (4.62)$$

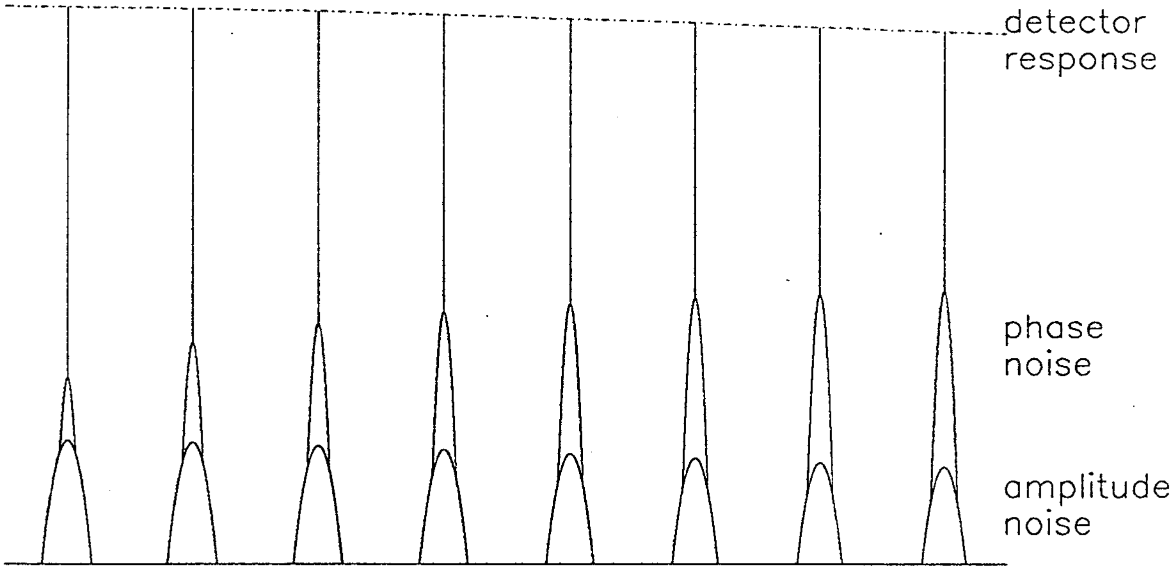

Figure 4.18: Power spectrum of a pulse train including noise bands, bandwidth limitation of detection (logarithmic vertical scale).

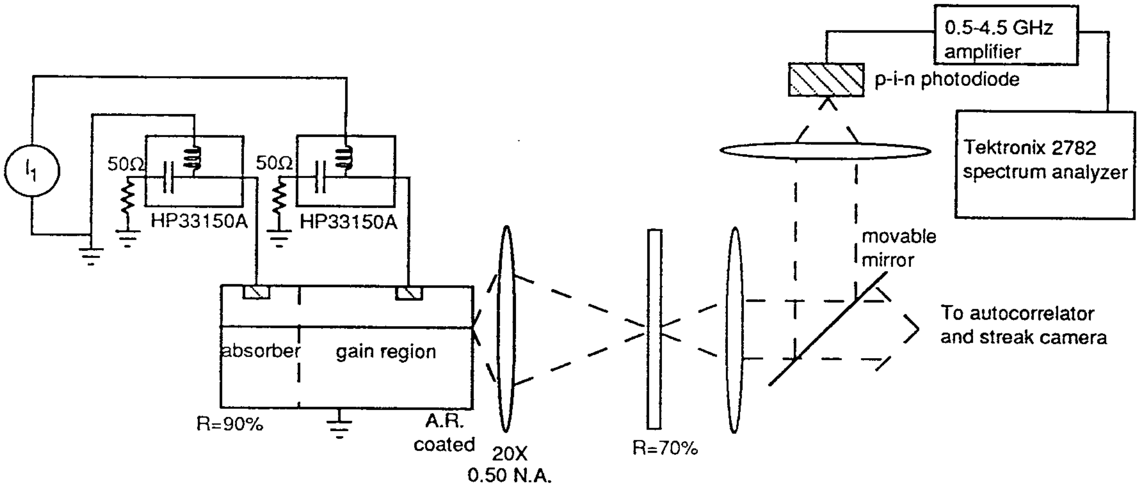

Figure 4.19: Two-section laser passively mode-locked for noise measurements.

from which the timing jitter over a frequency band f_1 to f_2 is

$$\Delta T = \frac{T}{2\pi n}\sqrt{\int_{f_1}^{f_2} L_P(f)df}. \tag{4.63}$$

4.5.2 Measurements of phase and amplitude jitter in mode-locked two-section quantum well lasers

The quadruple quantum well two-section laser is passively mode-locked at the fundamental cavity round-trip frequency, as shown in figure 4.19, with the beam focused on the external cavity mirror using a 20X microscope objective. The pulses have a full-width at half maximum (FWHM) of <8 ps, as determined from the autocorrelation and streak images shown in figure 4.20. The average power of the pulse train is 400 μW, and the spectrum, shown in figure 4.21, has a FWHM of 1.5 THz, a factor of about 25 in excess of the time-bandwidth product of these pulses. The pulse train stability is measured by spectral analysis of the photocurrent by focusing the beam onto an $\sim$ 10 GHz bandwidth detector, after which it is amplified 35 dB and measured with a Tektronix 2782 spectrum analyzer. The power spectrum consists of a set of carriers at harmonics of the 546 MHz pulse repetition frequency with broad noise bands, measurable up to 20 MHz from the carrier, after which the laser noise is smaller than the amplifier noise floor. As described in the preceding section, phase noise can be identified by the quadratic increase in its power spectral density with harmonic order, while the pulse energy noise density is independent of the harmonic.

The RMS timing jitter, ΔT_r, over a frequency band f_1 to f_2 can be determined from:

$$\frac{\Delta T_r}{T_r} = \frac{1}{2\pi n}\sqrt{\int_{-f_2}^{-f_1} L_p(f)df + \int_{f_1}^{f_2} L_p(f)df} \tag{4.64}$$

where T_r is the round-trip time; n is the harmonic order of the carrier being measured about; and $L_p(f)$ is the ratio of the single-side phase noise power spectral density to the carrier power. The RMS pulse energy fluctuations, ΔE, may similarly be found from:

$$\frac{\Delta E}{E} = \sqrt{\int_{-f_2}^{-f_1} L_a(f)df + \int_{f_1}^{f_2} L_a(f)df} \tag{4.65}$$

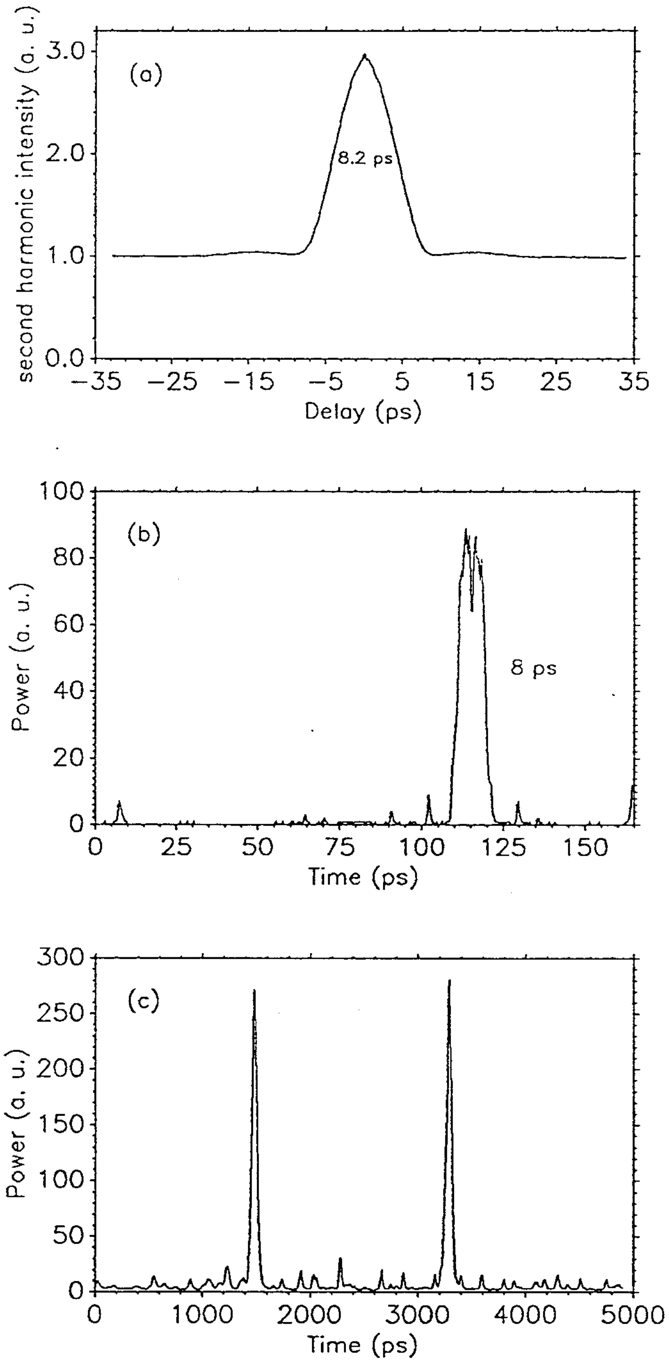

Figure 4.20: Measured pulsewidth using (a) autocorrelation and (b) streak camera (FWHM < 8 ps); (c) pulse train.

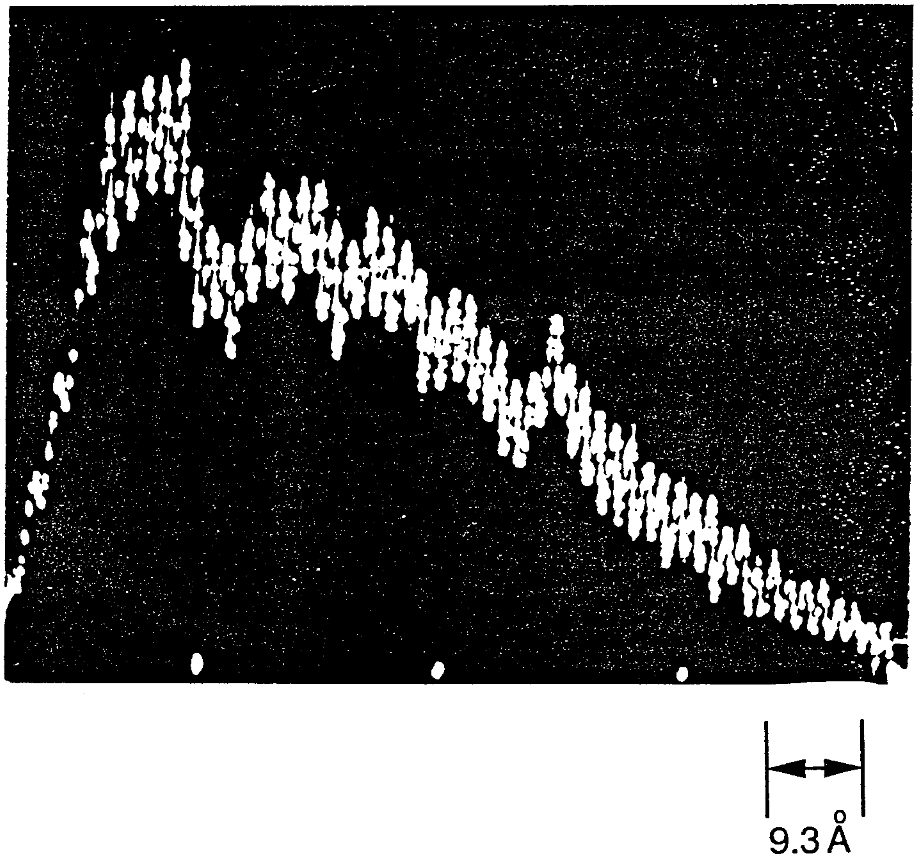

Figure 4.21: Optical spectrum of mode-locked laser ($\lambda_0 = 8510$ Å; scale is 9.3 Å per division).

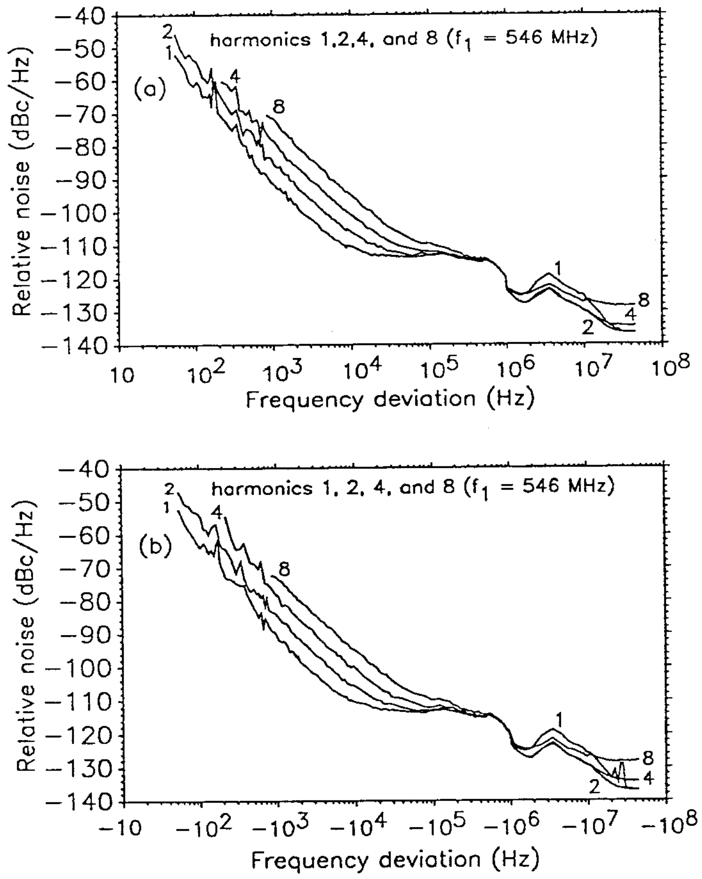

Figure 4.22: Ratio of noise power spectral density to carrier power.

where E is the pulse energy, and $L_a(f)$ is the amplitude noise density to carrier ratio.

The noise density to carrier ratio as a function of offset frequency from the carrier is shown in figure 4.22. Phase noise is much stronger than amplitude noise at frequencies below 10 kHz, while amplitude noise dominates at frequencies above 30 kHz. From 200 Hz to 9 kHz, the timing jitter is determined from a second order fit of the integrated

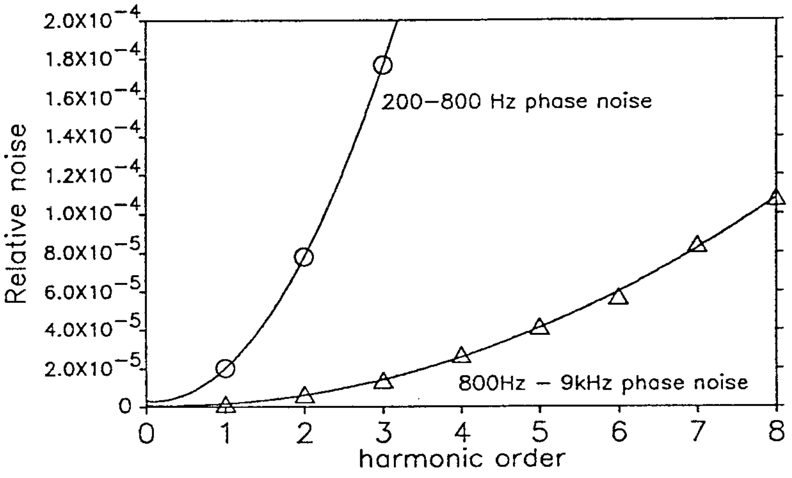

Figure 4.23: Parabolic fit of low frequency noise versus harmonic order.

noise power, as shown in figure 4.23. Between 9kHz and 30kHz, both phase and amplitude noise are present in similar quantities, but the total noise contribution here is negligible, compared to the noise from other frequency bands. The primary amplitude noise contribution is from 30 kHz to 10 MHz, with a peak around 3MHz. These peaks become very strong and narrow as the gain current is increased, and they are also observed at approximately the same frequency in other passively mode-locked quantum well lasers we studied. The apparent increase in noise of the higher harmonics above 1 MHz and the peaks at -20 MHz and -30 MHz are due to the

σ_J(50Hz, 200Hz)	$5.3ps$
σ_J(200Hz, 9kHz)	$1.4ps$
σ_J(9kHz, 273MHz)	$< 0.3ps$
σ_J(50Hz, 273MHz)	$5.5ps$

Table 4.2: Timing jitter.

measurement background level.

From the first and second order harmonics, the 50 Hz to 200 Hz RMS timing jitter, σ_J(50 Hz, 200 Hz), is 5.3 ps, and between 200 Hz and 9 kHz the jitter is 1.4 ps, giving σ_J(50 Hz, 9 kHz) = 5.5 ps. An upper bound on the timing jitter from 9 kHz to half the harmonic spacing of 273 MHz, is established from the eighth order harmonic noise level to be 0.24 ps, with the worst case assumption that the laser noise power is 6 dB below its measured value at offsets above 20 MHz, which is justified because the measured noise power is always within 1 dB of the noise floor throughout this range. The RMS pulse energy fluctuations, $\frac{\Delta E}{E}$, from 200 Hz to 20 MHz are 0.48%, as determined using the first order harmonic noise powers above 9 kHz and the zero order intercepts of the parabolic fits at lower frequencies. An upper bound on the amplitude fluctuations from 20 MHz to 273 MHz is found to be 0.19%, giving a total amplitude noise of $< 0.52\%$ above 200 Hz. These results are summarized in Tables 4.2 and 4.3. Some of the observed low frequency phase noise was traced to vibrations caused by laboratory instruments, so it should be possible to further reduce

σ_A(200Hz, 20MHz)	$< 0.48\%$
σ_A(20MHz, 273MHz)	$< 0.19\%$
σ_A(200Hz, 273MHz)	$< 0.52\%$

Table 4.3: Pulse energy fluctuations.

fluctuations in more mechanically stable cavities and in monolithic configurations.

For applications where an electrical synchronization signal is necessary, such as sampling measurements or synchronization of several mode-locked lasers, electrical pulses generated by the absorber can be extracted and should track fluctuations in the pulse train. For a laser mode-locked at 660 MHz, the FWHM of the electrical pulse is 135 ps and has an amplitude of 270 mV, as shown in the sampling oscilloscope photo in figure 4.24. The oscilloscope was synchronized to the optical pulse train using the PIN photodiode and an amplifier, and a similar measurement, shown in figure 4.25 of the gain section voltage shows that the gain recovery time is on the order of 1 ns. The absorber recovers fully between pulses, and the gain recovers much more slowly, as required to generate stable pulses.

4.6 Conclusions and future directions

In this chapter, it has been demonstrated that the two-section passively mode-locked quantum well laser can generate stable trains of pulses having durations shorter than

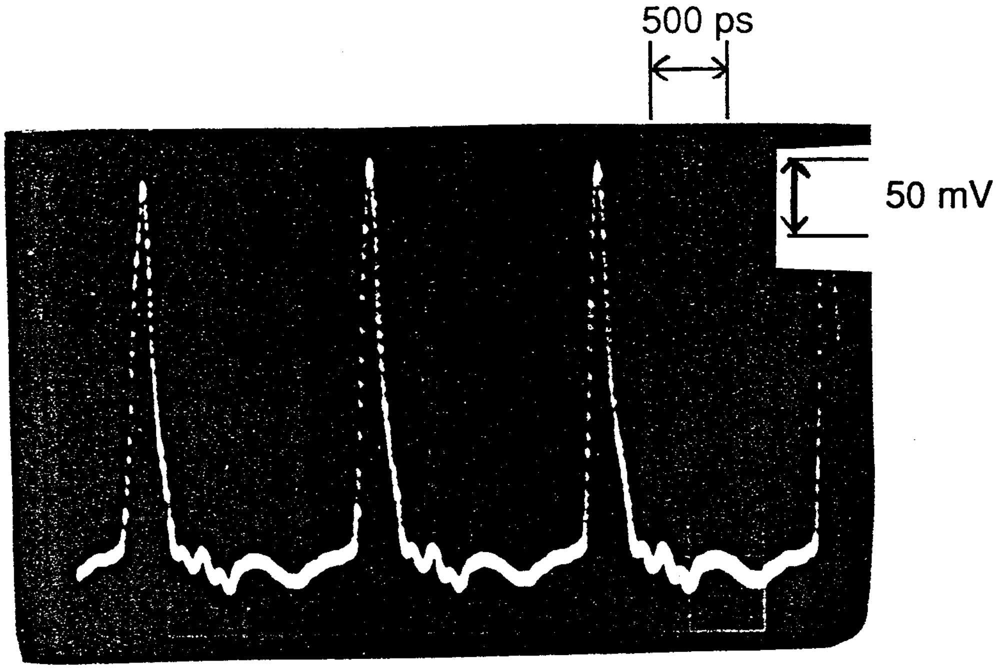

Figure 4.24: Electrical pulses generated by absorber (FWHM = 135 ps).

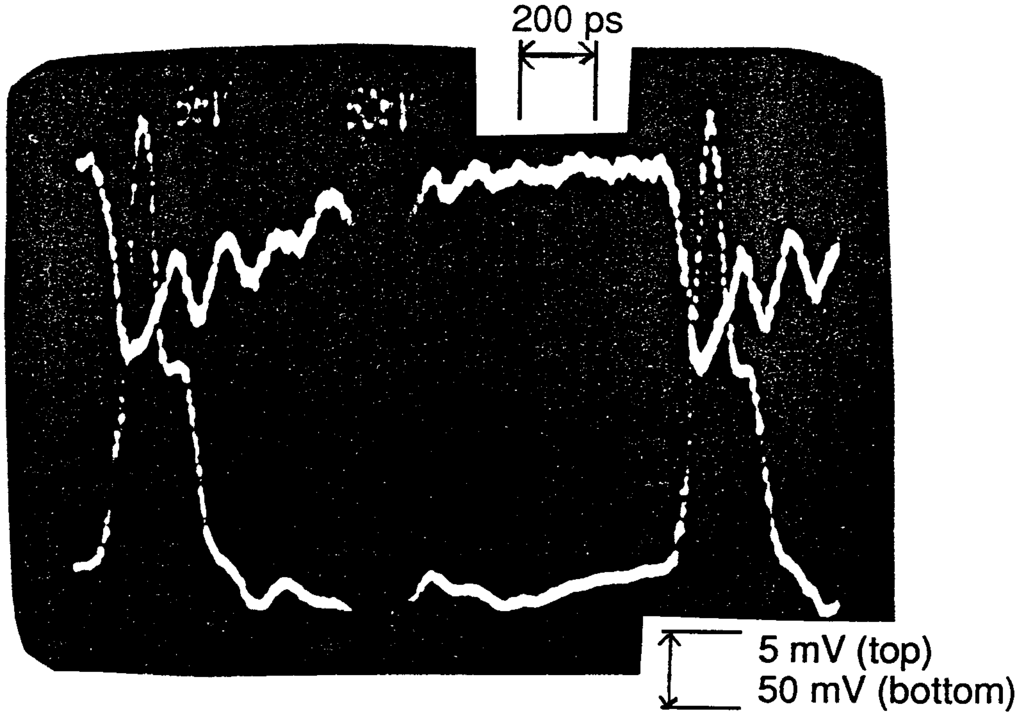

Figure 4.25: AC voltage on gain region (upper trace) and absorber (lower trace) while laser is passively mode-locked.

10 picoseconds. Theoretical models have been used to describe the basic operation of the device and to predict pulse energies and ranges where mode-locking should occur at different harmonics. Two-section quantum well lasers are well suited to generating stable pulses by passive mode-locking because of the decrease in differential gain with carrier density and the faster recovery of the absorbing region than the gain region. With a gain recovery time of one nanosecond, strong saturation passive mode-locking, where the leading and trailing edges see net loss on every round-trip, are expected to be attainable at repetition rates of a few hundred MHz to several GHz. If the mechanisms causing the broadening of the pulsewidths can be better understood and controlled, it should then be possible to use the two-section quantum well laser as a very simple source of stable subpicosecond pulses at these repetition rates.

The work in this thesis has demonstrated that quantum well lasers can be passively mode-locked at repetition rates ranging from 500 MHz to well over 100 GHz. At the low repetition rates, it was shown that stable pulses are generated, and that the pulsewidth is not strongly dependent upon the mode-locking frequency. The monolithic millimeter-wave mode-locked lasers operate in a regime where only small changes in gain and absorption occur under steady-state conditions. However, the very broad gain bandwidth, large ratio of differential absorption to differential gain, and fast absorber recovery allow a few modes to be excited and coupled together, giving rise to pulses with nearly 100% modulation depth. So far, it has not been possible to quantitatively study the stability of these high repetition rate pulse trains. The results on high frequency monolithic lasers and the lower frequency external cavity lasers are summarized in Table 4.4.

(a)

Monolithic Devices:	GaAs/AlGaAs	InGaAs/AlGaAs
repetition rate	108 GHz	42 GHz, 57 GHz
pulsewidth	2.4ps	5ps
$\Delta\nu\Delta\tau$	1.1	~2
pulse energy	50-100 fJ	0.6pJ
fastest observed modulation	130 GHz	100 GHz

(b)

External Cavity:	GaAs/AlGaAs
repetition rates	0.5-7 GHz
pulsewidth	5-8 ps
$\Delta\nu\Delta\tau$	~8
pulse energy	1-2pJ
σ_J(200 Hz, 273 MHz)	1.4 ps
σ_J(50 Hz, 273 MHz)	5.5 ps
σ_A(200 Hz, 273 MHz)	< 0.52%
synchronization signal	270 mV, 135 ps

Table 4.4: Summary of results from passively mode-locked (a) monolithic millimeter-wave lasers and (b) external cavity lasers.

References

[1] H.A. Haus, *IEEE J. Quantum Electr.*, **QE-11**, 736 (1975).

[2] H.A. Haus, *Jpn. J. Appl. Phys.*, **20**, 1007 (1981).

[3] G. Eisenstein, R.S. Tucker, U. Koren and S.K. Korotky, *IEEE J. Quantum Electr.* **QE-22**, 142 (1986).

[4] J.E. Bowers, P.A. Morton, A. Mar and S.W. Corzine, *IEEE J. Quantum Electr.*, **25**, 1426 (1989).

[5] M. Kuznetsov, D.Z. Tsang, J.N. Walpole, Z.L. Liau and E.P. Ippen,*Appl. Phys. Lett.*, **51**, 895 (1987).

[6] C. Harder, J.S. Smith, K.Y. Lau and A. Yariv, *Appl. Phys. Lett.*, **42**, 772 (1983).

[7] E.B. Treacy, *IEEE J. Quantum Electr.*, **QE-5**, 454 (1969).

[8] O.E. Martinez, *IEEE J. Quantum Electr.*, **QE-23**, 59 (1987).

[9] A. Takada, T. Sugie and M. Saruwatari, *Electron. Lett.*, **22**, 1347 (1986).

[10] E.P. Ippen, D.J. Eilenberger and R.W. Dixon, *Appl. Phys. Lett.*, **37**, 267 (1980).

[11] L.M. Frantz and J.S. Nodvik, *J. Appl. Phys.*, **34**, 2346 (1963).

[12] N.J. Frigo, *IEEE J. Quantum Electr.*, **QE-19**, 511 (1983).

[13] J.-C. Diels in **Dye Laser Principles with Applications**, ed. F. J. Duarte and Lloyd W. Hillman, Academic Press: Boston, pp. 58-68 (1990).

[14] C.P. Ausschnitt, *IEEE J. Quantum Electr.*, **QE-13**, 321 (1977).

[15] D. von der Linde, *Appl. Phys. B*, **39**, 201 (1986).

[16] D.J. Derickson, A. Mar and J.E. Bowers, *Electron. Lett.*, **26**, 2026 (1990).

Appendix A

Procedure for fabrication of multisection stripe lasers

A.1 Preparation of material

1. Cleave a piece of material, about 1 cm long by 5 mm wide.
2. If the back of the wafer contains indium, remove by lapping. Soak lapping block in acetone overnight to remove wafer and rinse in acetone, methanol, and deionized water.
3. Clean in boiling TCE for 5 minutes.
4. Soak in Acetone for 3 minutes.
5. Soak in Methanol for 3 minutes.

A.2 Photolithography and Etching of Stripes

1. Place wafer in hard bake (120°C) for 5-10 minutes; remove wafer and allow to cool.
2. Spin on Shipley 1350J photoresist, or equivalent, at 4500 RPM for 30 seconds.
3. Soft bake (80°C) for 20 minutes.
4. Expose the wafer with a photomask to define stripes (5-10 μm.) The length of the stripes should point along long axis of the oval defects that should be visible on the wafer surface.
5. Develop in Microposit developer for 15-45 seconds.
6. Hard bake for 20 minutes.
7. Mix up the etchant, 1:3:40 $H_2O_2 : H_3PO_4 : H_2O$, adding H_2O_2 last. This etchant can be made in advance and stored for several days.
8. Etch 1 minute per 1000 Å at room temperature, to a depth of 1 to 1.2 μm.
9. Strip the photoresist in a fuming 1:1 mixtrue of microposit 1112A photoresist remover and deionized water; rinse in water and blow dry.
10. Rinse the wafer in acetone, followed by methanol.

A.3 Silox growth and etch

1. Deposit about 1500 Å of SiO_2.
2. Spin on Shipley photoresist primer; let the primer sit for 30 seconds, then spin at 4500 RPM for 30 seconds.
3. Continue the photolithography as before using 1350J or equivalent and a mask with 1-2.5 μm openings along the length of the stripes.
4. Hard bake for 20 minutes.
5. Etch silox in buffered-HF solution for 30-45 seconds, and rinse in deionized water for at least 5 minutes.
6. Strip photoresist and rinse wafer as before.

A.4 Metallization

1. Spin on 1350J or equivalent at 3000 RPM for 30 seconds. Add more resist and spin again at 3000 RPM for 30 seconds.
2. Soft bake for 20 minutes.
3. Expose wafer to liftoff mask to define the multisection contacts.
4. Place in chlorobenzene for 5 minutes.
5. Blow dry and hard bake for 2 minutes.

6. Develop for about 2 minutes. Rinse in high purity deionized water for 3-5 minutes.
7. Plasma etch in oxygen for 20 seconds.
8. Evaporate the contact metals, 200 Å of Cr and 1500 Å of Au. The wafer should then be turned 180° around and another 1500 Å of Au evaporated to ensure that the contact is continuous over the edges of the etched stripe. To prevent hardening of the photoresist, the Cr should be deposited at a rate under 5 Å/sec, and the Au at a rate under 15 Å/sec. All thicknesses are the measured values from the Sloan Omni III thickness monitor using 5 MHz Ag crystals, and are about a factor of 3 smaller than the actual thicknesses.
9. Place wafer in acetone to lift off metal. If necessary, lightly brush the edges with a cotton swab.
10. Perform the photolithography and etching of the silox and GaAs cap layer for section isolation.
11. Lap the wafer to 3-4 mils.
12. Evaporate 200 Å AuGe and 800 Å Au on the back of the wafer.
13. Anneal the wafer for 20-30 seconds at 380°C.
14. Cleave the wafer into laser bars, using a scriber and/or scalpel.